Numerical Study on the Influence of Magnetic and Electric Fields on Filtration Performance of Wet Granular Beds

By

Sina Sabbaghian

A thesis

Presented to Sharif University of Technology, International Campus, Kish Island

in partial fulfilment of the

Requirements for the Degree of

Master of Science

in

Mechanical engineering

Supervisors:

Dr. Ali Moosavi

Dr. Hani Sadrhosseini

Kish Island, Iran, 2019

Sharif University of Technology

International Campus, Kish Island

This is to certify that the Thesis Prepared,

By: **Sina Sabbaghian**

Entitled: **Numerical Study on the Influence of Magnetic and Electric Fields on Filtration Performance of Wet Granular Beds**

and submitted in partial fulfilment of the requirements for the Degree of

<u>Master of Science</u>

Complies with the regulation of this university and meets the accepted standards with respect to originality and quality.

Signed by the final examining committee:

Supervisor: Dr. Ali Moosavi _____

Co-Supervisor: Dr. Hani Sadrhosseini _____

External Examiner: Prof. Masoud Darbandi _____

Internal Examiner: Dr. Mahdi Sani _____

Session Chair: _____

AUTHOR'S DECLARATION

I hereby declare that I am the sole author of this thesis. The work described in this thesis has not been previously submitted for a degree in this or any other university. All and any contributions by others are cited. This is a true copy of the thesis, including any required final revisions, as accepted by my examiners. I understand that my thesis may be made electronically available to the public.

Abstract

Numerical Study on the Influence of Magnetic and Electric Fields on Filtration Performance of Wet Granular Beds

Sina Sabbaghian, M.Sc

Sharif University of Technology, International Campus, kish Island, 2019

Supervisor: Dr. Ali Moosavi

Co- Supervisor: Dr. Hani Sadrhosseini

The aim of this study is to develop an understanding of the role of the magnetic and electric force on the filtration performance of wet granular beds. At first, the effect of wetting is considered by locating micro water film around the square channel for particle deposition in three different Reynolds numbers (Re=1, Re=5, Re=10). Typically, 1000 particles of different sizes ($100nm - 10\mu m$) were injected into the microchannel when air and water formed completely on the surface of the block. Drag force, Brownian force, Saffman`s lift force and gravity force affect the particles. After that, Dielectrophoretic and Magnetophoretic forces were included in the domain for investigating the role of these forces in collecting aerosol particles. A 2-D microchannel and a micro single square fiber, which is located in the microchannel and its blockage ratio is 0.25, are considered in this simulation. Comsol software is used for simulating. By adding a film of water around the block, the efficiency of capturing particles is increased, especially in low Reynolds numbers. For the effect of the electrostatic and electromagnetic field, the variation for particle deposition is 0 to 20 %.

Keywords: *Nanoparticle, wetting, filtration, wet granular filters, electromagnetic, electrostatics*

v

Acknowledgements

I would like to express my gratitude to my supervisor, Dr. Ali Moosavi for the continuous support, useful comments, remarks, engagement and immense knowledge through the learning process of this master thesis.

My sincere thanks also go to Dr. Hani Sadrhossein as one of my supervisors, for her patience, motivation, enthusiasm and of course her non-stop support. She consistently allowed this thesis to be my own work but steered me in the right direction whenever she thought I needed it.

I would also like to thank Dr. Mahdi Sani. The door to Dr. Sani`s office was always open whenever I ran into a trouble spot or had a question duration of the master`s program. Thanks for all the things that he taught me.

I would like to acknowledge Prof. Masoud Darbandi and Dr. Mahdi Sani as the defense committee, and I am gratefully indebted to them for their very valuable comments on this thesis.

Last but not least, I must express my very profound gratitude to my mother and to my sister and brother for providing me with unfailing support and continuous encouragement throughout my year of study. This accomplishment would not have been possible without them. Thank you.

Dedication

To my amazing mother who plays both roles in my life.

Table of Contents

x

List of Figures

xiv

xv

List of Tables

Chapter 1

Introduction

Clean air is a vital substance for the human. According to WHO (World Health Organization) data (2018), the majority of deaths caused by lung disease and cancer (about 1.8 million every year) are attributable to air pollution. Air pollution is divided into natural and man-made. First one includes radon, fog and mist, ozone, ash, soot, salt spray, and volcanic and combustion gases and man-made air pollution is produced from the burning of fossil fuels, such as coal, oil, natural gas, and gasoline to produce electricity and power our vehicles. Existing harmful particles in these two types of air pollution makes it necessary for the environment and human health to capture these particles from ambient.

One of the simplest and most wildly ways of removing particles from carrier flow is using filters such as fiber filters, fibrous filters, cyclones, electrostatic precipitators, and granular bed filters.

In this research, wet granular bed filters are considered to simulate, and the effect of electrostatic and electromagnetic is investigated on wet granular filers.

1.1 Granular Filters

Granular filtration is a fluid-solid separation process usually applied to remove little quantities of small particles from numerous kinds of fluids. Historically, this engineering practice is interesting. Both Sanskrit medical knowledge and Egyptian inscriptions give a clear sign that granular filtration was used for water treatment (as early as 200 bc), as detailed in Baker's book, The Quest for Pure Water (1949). At the same time, there is hardly a section

of the process and chemical industries that do not use granular filtration today. The important number of patents fixed in recent years to liquid- and gas-cleaning processes based on granular filtration proves its enduring utility.

The usefulness of granular filtration is clear from its possibility of application as well as from the manner in which it is achieved. Either liquid or gas fluid streams can be treated. Besides water and air, systems which may be behaved by granular filtration contain such varied substances as flue gas, melted metal, petrochemical feedstocks, polymers, alcoholic, or non-alcoholic beverages [1]. While in most cases granular filtration is accomplished in the fixed-bed mode, it may also be piloted in moving-bed or fluidized-bed style so that the procedure can be carried out constantly.

The basic standard of granular filtration remains the same, including the treatment of the system, the usage of medium, or the manner in which filtration is carried out. Under pressure or gravity, the suspension is forced to pass through a medium composed of granular substances (granular medium). When suspension flows through the medium, some of the particles in the suspension, because of the several forces acting on them, move toward and deposited on the surface of the granules of which the medium is composed. The level of deposition throughout the medium cannot be made uniform in general; however, the whole of the medium is proposed to be used for particle collection.

1.1.1   Granular Filtration

Fluid–particle separation technology means a collection of processes for clearing (as contaminants or impurities), separating (suspended particles from suspending fluid or one type of particles from a mixture of particles), and concentrating and recovering (as products)

particles from fluid–particle suspensions [2]. As a technology, its age is probably second only to that of crushing and grinding of solids [3]. While the processes categorized as fluid–particle separation are too various to be cited exclusively, it is generally accepted that fluid–particle separation includes granular and fibrous filtration, cake filtration, cartridge and, cycloning, thickening membrane filtration, dewatering and expression, flocculation, scrubbing, and electrostatic precipitation. The technology is simple to a large number of manufacturing industries (mineral, chemical, and food and beverages) as well as to pollution reduction and environment control (e.g., clean rooms). Truly, it is hard to find any important engineering enterprise in which fluid–particle separation is not involved.

The connection between the numerous fluid–particle separation procedures can be seen from the grouping scheme offered by Tiller (1974) for liquid-solid separation. This scheme, shown in Figure 1.1, is based on Tiller's idea that solid-liquid separation can be viewed as a system consisting of one or more stages: (1) pretreatment, to facilitate the operation of subsequent stages; (2) solids concentration, to increase the solid content of suspensions; (3) solids separation, to separate solids and the suspending liquid; and (4) post-treatment, to improve the quality of the recovered products (either solid or liquid).

The diagram illustrated in Figure 1.1 is suitable in defining the function and field of application of granular filtration; which is, the process is used primarily for illuminating watery suspensions using the granular media as depositing bodies for particles present in the suspension. In opposition, cake filtration is recovering solid products from relatively concentrated slurries. The difference between cake filtration (a subject often included in basic engineering texts) and granular filtration is the manner in which they operate. In the former case, the medium (or the bulk of it) through which the treated suspension flows is composed of the solids to be recovered.

3

```
                    ┌─ Chemical
                    │  Flocculation
                    │  Coagulation
    Pretreatment ───┤
                    │
                    └─ Physical
                       Crystal growth
                       Freezing and other physical changes
                       Filter aid addition

                    ┌─ Thickening
                    │  Hydrocycloning
    Solids          │
    concentration ──┤
                    │
                    └─ Clarification
```

```
                                                            ┌─ Batch
                                            Press, vacuum, ─┤
                    ┌─ Recovery of solid    gravity filters │
                    │  particles                            └─ Continuous
                    │
                    │  Cake formation ──┤
                    │                                       ┌─ Filtering
    Solids          │                                       │  Solid bowl
    separation ─────┤                       Centrifuges ───┤
                    │                                       │
                    │                                       └─ Sedimenting
                    │                                          Perforated bowl
                    │  Clarification
                    └─ No cake formed
                       Deep granular beds
                       Cartridges
```

```
                    ┌─ Filtrate ── Polishing
                    │              Membranes
                    │              Ultrafiltration
    Posttreatment ──┤
                    │
                    └─ Cake ── Washing ──────── Deliquoring
                               Displacement     Drainage
                               Reslurry         Mechanical
                                                Hydraulic
```

Figure 1.1 Stages of solid-liquid filtration [4]

1.1.2   Granular Filtration versus Fibrous Filtration

Fibrous filtration denotes to the removal particles' procedure from gas streams affected by
fleeting streams through fibrous media. According to the system in which the filter media are
founded, particle holding deposited in surface and throughout the media. In the former case,
the fibers (natural or chemical fibers, cellulose, metal or glass fibers) are pressed together in

4

felt or spun or woven into cloth (fabric) that their filter media pores are relatively small (as compared with the size of the particles to be removed)[1].

Several amounts of particles deposited in the form of filter cakes at the surface of the medium and removed discontinuously at extreme pressure. This fibrous filtration is similar to cake filtration with removing particles from solid-liquid slurries. Baghouse filters used in power utilities are a typical instance of this operation[1].

If the fibrous media packs fibers loosely, for example, those used in ventilation and air-conditioning applications, withholding particles will be typically removed within the interior of the media. This kind of fibrous filtration is comparable to granular filtration. As the physical laws governing the flow through either type of media are the same, the methodologies used to describe either type of filtration become almost interchangeable. This resemblance, obviously, does not suggest that they are the same as each other. Furthermore, the geometries of the entities creating the filter media are obviously different (e.g., granules or spheres in granular media vs. fibers or cylinders in fibrous media). There are also important differences between packing densities (or porosity), collector sizes, and mechanical strength [5]. As filtration performance, fibrous filters have the benefits of higher single collector efficiency and lower pressure drop, because of their small collector size (i.e., fiber diameter) and high porosity. Also, granular filters can be easily regenerated in contrast to the difficulty of removing deposited particles for individual fibers. Additionally, granular filtration is more suitable in treating high-temperature and/or corrosion gaseous streams, because of the relative abundance of granular substances which are temperature-and corrosion-resistant [6].

1.1.3 Granular Filtration for Gas Cleaning

The requirement of industrial processes is caused by developing granular filtration for gas cleaning. Less work has been done to standardize the design and process of systems. As against, a large number of granular filters of different designs and configurations were developed [7].

1.1.4 Savannah River Plant (SRP) Sand Filters

One usually mentioned example representing the efficiency of granular aerosol filtration is the use of sand filters to remove radioactive particulates from gas streams. Both the fuel-processing plants at Hanford, Washington, and at Savannah River, Georgia, utilize sand filters for this purpose [2]. These filters are usually very large. For example, the two original filters at Savannah River have a cross-section of over $2000m^2$ ($30.45 \times 73.15m$) [8], while the dimension of the filter installed in 1975 then has a cross-section of over $3300m^2$ ($30.5 \times 110m$), treating gases at a rate of 3000 to $3500\ m^3/min$ (Orth, et al., 1976). Several layers of coarse granules are used for the filter media (prefilter sections), layers are composed of three layers of fine sand, set along the direction of gas flow. The designed gas velocity is under 3 cm/s to ensure that no radioactive particles enter. Low gas velocity is the reason that these filers are constructed too huge. The initial pressure associated with the gas flow through the filter (i.e., when the filter is free of any particle deposition) is $19cm\ H_2O$. Total collection efficiency is well over 99%. These filters are extraordinarily reliable. The integrity of material plays a key role in the useful life of these filters. For example, one of the original filters was changed at Savannah River because of the acid attack and erosion of the filter's concrete support structure[1]. Prior to its replacement and over a period of 40 years of operation, the filter's collection efficiency remained not only steady but actually improved with the only

moderate pressure-drop increase. Besides the corrosion and erosion problems, the major operational trouble met was the condensation of moisture from the filtered gas, which led to the compaction and channeling of the filter medium[9].

1.1.5 Ducon Filter

The Ducon filter, developed by Zenz and his associates (Zenz, 1971; Zenz and Krockta, 1972; Kalen and Zenz, 1974), is a fixed-bed filter with fluidized expansion for media cleaning. Figure 1.2 shows a schematic diagram describing the operational principle given in Zenz's patent. The filter is made of an array of sections formed by two punched, concentric cylindrical walls practically filled with filter grains. Gas goes in the section through the outer wall and flows down into the granular media. The cleaned gas passes through the inner wall and is backlogged in a manifold in the inside of the filter. When the pressure drop across the specific compartment becomes excessive, the medium may be cleaned by fluidizing the filter grains. This "blowback" is made by passing the clean gas in the reverse direction and is possible because each compartment is not completely packed with filter grains. The Ducon filter has been applied in recovering fine from a fluid-cracking catalyst regenerator[10]. A modified version of the Ducon filter was also tested to clean flue gas from a fluidized combustor (Hoke and Gregory, 1977).
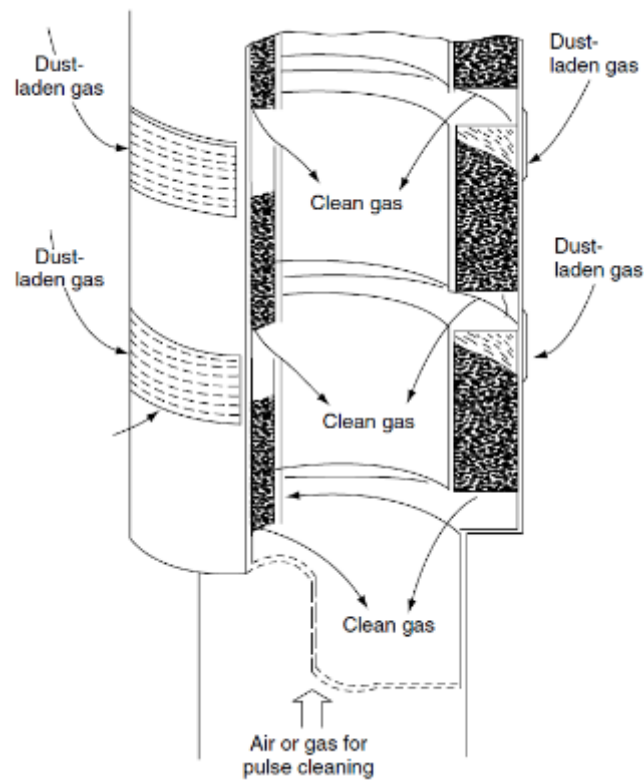
Figure 1.2 Duncon Co, expandable-bed filter element [1].

1.1.6 Wet Scrubber Filters

Emission control equipment commonly used to remove particles includes wet scrubbers, electrostatic precipitators, cyclones, and fabric filters. A wet scrubber is an effective tool in removing particles as it brings particle-laden gas into contact with liquid droplets. The scrubbing mechanisms are represented by diffusion, interception, inertial impaction, and gravitational settling. Among these mechanisms, inertial impaction remains an important mechanism for the capture of particles larger than 5.0 mm, while diffusion is essential for the capture of smaller particles (Ebert and Buttner, 1986; Gemci and Ebert, 1992).

Figure 1.3 is a sketch of a gravitational wet scrubber. The unit causes very little pressure loss and can handle large volumes of gases. As the particle-laden gas flows upward, particles

8

collide with liquid droplets sprayed across the flow passage, and then liquid droplets containing the particles settle to the bottom of the scrubber. It is known that gravitational wet scrubbers are generally not suitable for removing particles smaller than 1.0 mm. Scrubbers combined with electrical precipitation (Laitinen et al., 1997) and modified scrubbers (Boll, 1973; Yung et al., 1978; Fan et al., 1988; Spink, 1988) had been suggested as a means to increase small particle removal efficiency. However, operational conditions of the gravitational wet scrubber, including droplet residence time, droplet size, and liquid-to-gas flow ratio, may play a role in removing particles much smaller than 1.0 mm in diameter. Although the gravitational wet scrubber is commonly used to remove particles from gas streams, the exact mechanisms involved are still not fully understood.
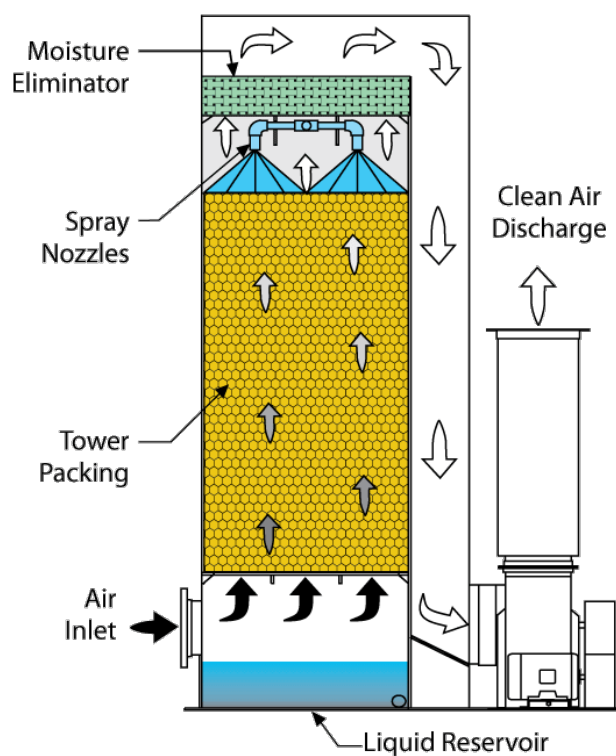
Figure 1.3 Schematic of a wet gravitational scrubber.

1.2   Aerosol Filtration Mechanisms

The aerosol is produced by different events on the earth or atmosphere. Aerosol filtration, unexpectedly, refers to the removal of solid and liquid particles suspended in the air. Considering a spherical shape, the size of the aerosol particle has been measured as the diameter of the particle. Figure 1.4 represents the particle size of common air contaminants.
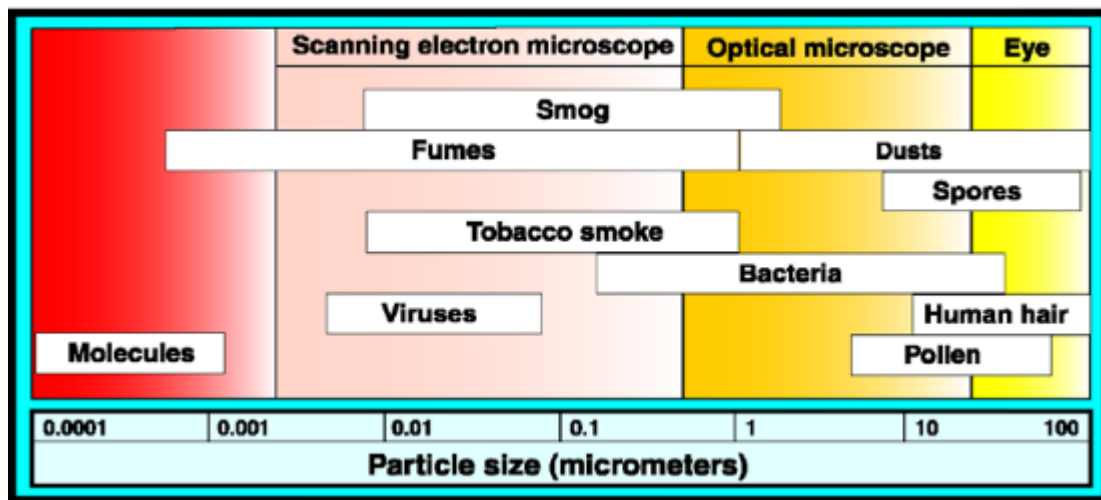
Figure 1.4 Common air contaminants and their relative sizes [11], [12]

According to Table 1-1, aerosol filtration is more complicated than hydrosol filtration. There are four basic mechanisms for the aerosol particle to deposit a neutral fiber in aerosol filtration, including interception, inertial impaction, Brownian diffusion, and gravitational settling (negligible in the case of Nanoparticles).

Table 1-1 Capture Mechanisms of aerosol filtration and hydrosol filtration

	Flow Phase	Particle Phase	Capture Mechanisms
Aerosol	Gas	Solid/Liquid	Interception
			Inertia impaction
			Diffusion
			Gravitational settling
Hydrosol	Liquid	Solid	Interception

The collection efficiency of a fibrous filter media can be described as the fraction of entering particles that are protected by the filter, either based on particle count or mass. Figure 1.5 has shown the collection efficiency curve of a fibrous filter with the thickness t=mm, SVF $\alpha = 5\%$, fiber diameter $df = 2\ \mu m$ and flow face velocity $V = 0.1\ m/s$ [11]. By regarding this fact that interception and inertial impaction are the dominant mechanisms for big particles - while diffusion is dominant for small particles-, the combined effects of interception, inertial impaction and diffusion result in a typical V–shape in the collection efficiency curve. The typical V-shape efficiency curve changes according to the filter type and flow velocity. By decreasing fiber diameter, the efficiency curve will shift to the left and the size of the V–shape will reduce and vice versa. For Nanoparticle filtration, which diffusion is the dominant mechanism, the residual time for the particles and fibers to interact is extended through reducing flow velocity [13] and collection efficiency proliferates. Inertial impaction augments when flow velocity augments.
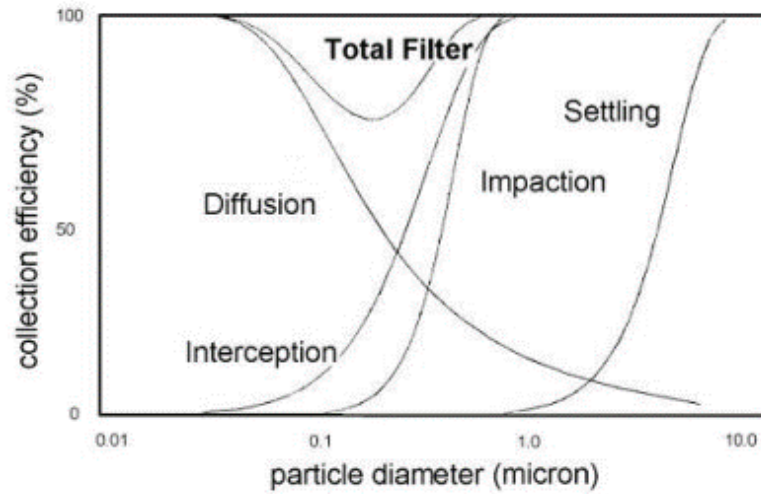
Figure 1.5 A typical fraction collection efficiency curve for filter media [14]

1.3 Evaluation of Filtration Performance

Collection efficiency E and pressure drop ΔP (or permeability k) are two important factors in describing and rating fibrous filters. Pursuant to their end-use, filters have various requirements for their collection efficiency. Some filters are designed to have high collection efficiency (e.g., HEPA) unlike other filters. Minimum pressure drop (maximum permeability) for desired collection efficiency is an advantage for filters. Collection efficiency should be defined as the fraction of entering particles that are retained by the filter based on either particle count or particle mass; as is shown below, the first one is lower than the other:

$$E = \frac{N_{in} - N_{out}}{N_{in}} \tag{1-1}$$

$$E_m = \frac{C_{in} - C_{out}}{C_{in}} \tag{1-2}$$

where N and C refer to the number and mass concentration of particles at inlet and outlet of the filters, respectively.

Penetration (P) is defined as the fraction of entering particles that exist or penetrate the filter based on either particle count or particle mass, which characterized the ability of the filter to take particles:

$$P = \frac{N_{out}}{N_{in}}$$

(1-3)

Also, collection efficiency and pressure drop are two terms generally used in filtration literature.

$$P_m = \frac{C_{out}}{C_{in}}$$

(1-4)

Another two parameters to assess filter performance are:

Quality factor (QF) and Minimum Efficiency Reporting Value (MERV).

QF in industrial terms is the indicator of filters performance considering both collection efficiency and pressure drop; QF is defined as:

$$QF = -\frac{\ln[(1-E)*100]}{\Delta P}$$

(1-5)

Most of the neutral fibrous filters become more efficient as they load with dirt. MERV is a number from 1 to 20 to assess the lowest point of efficiency, which in most cases the moment the filter is just installed [12]. The higher the value of MERV shows, the more efficient air filters are. MERV value is commonly used in the industry to show: low efficiency filters with MERV 1-4 are applied to challenge particle with dp >10 μm; filters with MERV 5-8 are

applied to remove particle with dp ranging from 3 to 10 µm; filters with MERV 9-12 are applied to challenge particle with dp ranging from 1 to 3 µm; High efficiency filters with MERV 12-16 are applied to remove particle with dp ranging from 0.3 to 1 µm; and High efficiency filters with MERV 16-20 are applied to remove the extremely small particle with .

In order to evaluate the performance of the filters, two tests have been designed in the United States; the first one is ASHRAE(American Society of Heating, Refrigerating and Air Conditioning Engineering) 52.1-1992 and the other is ASHRAE 52.2 –1999 [12]. The test ASHRAE 52.1-1992 measures filters ability to capture a mass fraction of coarse dust and filters ability to eliminate large particles. ASHRAE 52.1-1992 could be applied for low- and medium- efficiency filters. ASHRAE 52.2-1999 focuses on "Method of Testing General Ventilation Air Cleaning Devices for Removal by Particle Size". This one is used more in laboratory and measures the efficiency of the filters versus a wide range of particle size. The sample filter, generally having face dimensions of 24" by 24", is placed in a dust test in this newer stand test. Based on filter type, the airflow in the duct is set at a constant value ranging from 500 –3000 cfm. Aerosols in 12 sizes ranging from 0.3 to 10 µm injected upstream of the sample filter, upstream particle number and downstream particle number are found by particle counters. The collection efficiency for every 12 channels could be evaluated by this test.

1.4   Existing Theories of Filtration

Noticing flow pattern is the only way to estimate the filtration performance based on the structure of the filter. Since the basic flow pattern is known, the pressure drop across the media could be obtained and the injected particles' behavior inside the web could be derived, which leads to a better understanding of filtration process [15].

In filtration, the inertia or the viscosity of air dominates depends on the scale of the system and on the velocity of the air. The relative importance can be ascertained by the Reynolds number (RE):

$$Re = \frac{inertial\ force}{viscous\ force} = \frac{\rho V L}{\mu} \qquad (1\text{-}6)$$

Where ρ is the air density and is approximately $1.20\ kg/m3$ and μ is the coefficient of viscosity, which equals 1.81×10^{-5} at NTP.

L is the characteristic length and is equivalent to fiber diameter in this case.

Reynolds number is used to recognize three flow regime, including 1) very low Re indicates viscous creeping motion (inertial effects are neglected), 2) moderate Re implies a smoothly varying laminar flow, and 3) high Re indicates turbulent flow. For the flow velocity and the fiber diameter considered in this work, Re is low, and the flow is laminar flow. For microfiber media filtration with low velocity, Re<1, and the extreme case of laminar flow, inviscid flow is valid in which inertial influence is neglected and Reynolds number is assumed to be zero. Inviscid flow is a flow pattern which does not change with the velocity, and is a special matter (Brown, 1993).

When in aerosol filtration, molecular effects in airflow could be ignored (continuous fluid), the obstacles in flow path are larger than the mean free path of air molecules (λ). If the flow is perpendicular to the webs of 3D layered structures, as most of the nonwoven filters are, the obstacle length is really fiber diameter (d_f). At NTP (Normal Temperature and Pressure – air at $20°C$ and $1\ atm$), the flow is continuous when the fiber is above the sub-micrometer size [15].

Computing an air flow could be done after describing a mathematical model for the fibrous filter. Then, filter collection efficiency should be obtained after particle injection. During the past decades, there have been many pioneering types of research, dealing with either single fiber or a structured array of fibers, which has aided developing the filtration science and technology to its current level. ([16]–[37])

Most of these studies have been limited to systems consisting of rows of fibers (often in two-dimensional geometries) perpendicular to the flow direction. The results show that there have been a few endeavors regarding simulating the multi-fibrous filter media with various fiber's cross-sectional shape and arrangement. Also, these media had not an important effect on filtration performance.

1.5   Pressure Drop and Slipping Effect

The relative velocity of the gas at the surface of the fibers is zero, which is not met for small fibers at NTP. Davies (1973) showed that the slipping effect could be considered for small fibers whose size is comparable with the mean free path of air molecules.

Four different regimes have been recognized in the gas flow based on the value of Knudsen Number $Kn = \frac{2\lambda}{d_f}$ including: 1) free molecule regime ($Kn > 10$); 2) Transient regime ($10 > Kn > 0.25$); 3) Slip flow regime ($0.25 > Kn > 0.001$; and 4) Continuum regime ($Kn < 0.001$).

There are many pieces of research about collection efficiency and pressure drop of these regimes [38], [39]. Most of these studies were carried out with paper filters used with high flow rates and may not obey Darcy's law. Davies [40] showed that problems with high

Knudsen number consist of the calculation of the particle motion through the lower atmosphere or higher temperature condition.

Hinds (1999) has shown that for a continuous flow, a filter's pressure drop is a function of air viscosity, filter thickness, face velocity, fiber diameter, and a parameter $f(\alpha)$, being only a function of the filter Solid Volume Fraction (SVF).

$$\Delta p = f(\alpha)\frac{\eta t U}{d_f^2} \qquad (1\text{-}7)$$

Different theories presented various equations for $f(\alpha)$. Hinds (1999) [11] represented the Kuwabara's cell model, $f(\alpha)$:

$$f(\alpha) = \frac{16\alpha}{Ku} \qquad (1\text{-}8)$$

For the channel arrays model, $f(\alpha)$ based on Rao and Faghri (1988) numerically solution is considered as:

$$f(\alpha) = 10.54\alpha + 157.36\alpha^2 + 578\alpha^3 \qquad (1\text{-}9)$$

Sangani and Acrivos (1982), presented another model by solving a series of bi-harmonic equations for Stokes flow:

$$f(\alpha) = \frac{16\alpha}{K_{channel}} = \frac{16\alpha}{-\frac{1}{2}ln\alpha - 0.738 + \alpha - 0.887\alpha^2 + 2.038\alpha^3} \qquad (1\text{-}10)$$

Henry and Ariman (1983) conducted $f(\alpha)$ based on the numerical study for staggered arrays model, as follows:

$$f(\alpha) = 9.784\alpha + 152.64\alpha^2 + 555.6\alpha^3 \qquad (1\text{-}11)$$

Sangani and Acrivos (1982) introduced another expression for the stag arrays model:

9

$$f(\alpha) = \frac{16}{K_{stag}} = \frac{16}{-\frac{1}{2}ln\alpha - 0.735 + \alpha - \frac{1}{4}\alpha^2} \qquad (1\text{-}12)$$

In this field, there are many theoretical models for justifying an appropriate correlation but still, some of the most successful permeability models are based on pure empiricism [11], [15], [40]. Davies's experimental correlation is given to calculate the pressure drop of a variety of filter media with SVF ranging from 0.6% to 30% [40]. Dimensionless pressure drop based on Davies' correlation is:

$$f(\alpha) = 64\alpha^{\frac{3}{2}}(1 + 56\alpha^3) \qquad (1\text{-}13)$$

Pich (1971) presented the summary of theoretical findings for pressure drop over all values of Knudsen number [39]. According to Pich's theory, the pressure drop across the filters, ΔP, is related to the pressure drop across the filter when $Kn = 0$, ΔP_0. For $Kn < 0.001$, $\Delta P/\Delta P_0 = 1$

For $0.25 > Kn > 0.001$

$$\frac{\Delta P}{\Delta P_0} = \frac{1 + \frac{0.998 Kn_0}{-0.75 - 0.5ln\alpha}}{1 + \frac{0.998 Kn}{-0.75 - 0.5ln\alpha}} \qquad (1\text{-}14)$$

where Kn_0 is the Knudsen number of the fibers at maximum pressure which is usually one atmosphere.

For $Kn > 10$,

$$\frac{\Delta P}{\Delta P_0} = \frac{0.57}{Kn}(-0.75 - 0.5ln\alpha + 0998 Kn_0) \qquad (1\text{-}15)$$

There is not any theory to introduce the transition regime for $10 > Kn > 0.25$, and the schematic dependence is presented in Figure 1.6, in which X-coordinate is the operating pressure and Y-coordinate is the pressure drop, ΔP.

In the slip flow region, the influenced of slip effect on single fiber efficiency is accounted by correlating the diffusion and interceptions term by slip correction factors [41].
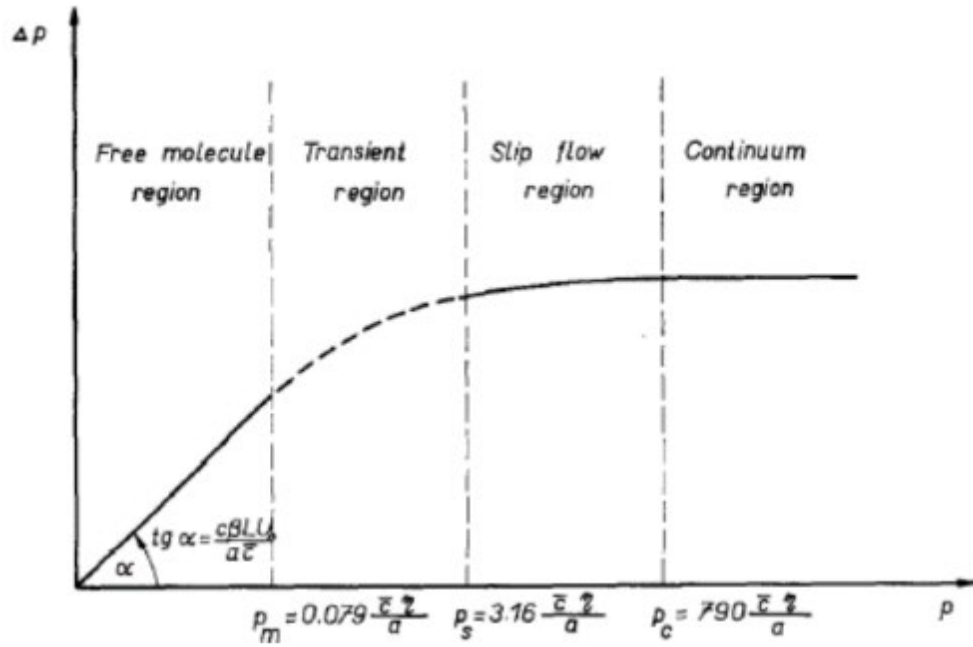
Figure 1.6 Schematically dependence of the pressure drop across the filters on the operating pressure of fibrous filter with low solid volume fraction[39].

Where

$$C_d = 1 + 0.388 Kn \left(\frac{(1-\alpha)Pe}{Ku}\right)^{\frac{1}{3}} \ and \ C_R = 1 + \frac{1.996 Kn}{R} \qquad\qquad (1\text{-}16)$$

Air resistance and permeability are employed to describe the pressure drop across a fiber. These two terms could be used as follows: 1) the term air resistance is often used for the pressure drop across a filter at some arbitrary flow rate. So, the resistance, *W*, is

$$W = \frac{\Delta P}{Q} \qquad\qquad (1\text{-}17)$$

11

Where $Q = U/A$ is the flow rate and A is the area of the cross-section of the sample.

2) The second term is the permeability. Based on Darcy`s law (only valid for slow, viscous flow), permeability, k, is inversely proportional to the pressure drop:

$$k = \frac{Ut\mu}{\Delta P}$$
(1-18)

1.6 Regimes of Two-Dimensional Flow Around a Bluff-Body

When flow passes over a circular cylinder as an instance of a bluff-body, a region of disturbed flow is formed around the cylinder. Zdravkovich (1997) categorized the disturbed flow field around a circular cylinder into four regions (Figure 1.7)[42]:

(I) The narrow retarded flow region in which the local time-averaged velocity is less than the free-stream velocity.

(II) Two boundary layers which are attached to the surface of the cylinder. These boundary layers around the cylinder beget under the effect of an eligible pressure gradient followed by a small region of noxious pressure gradient just before separation.

(III) Two sidewise regions of displaced and accelerated flow. The expansion of displaced regions is strongly correlated to the blockage influence.

(IV) One wide downstream region of separated flow named the wake. The form of the wake is affected by the state of the flow, which may be laminar or turbulent.
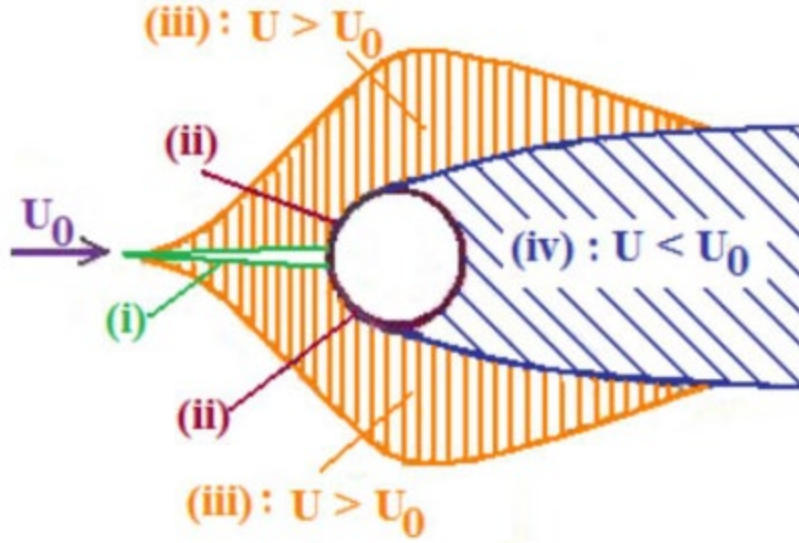
Figure 1.7 Regions of disturbed flow around a circular cylinder [44].

The phenomenon of vortex shedding from circular cylinder outcrops for a broad range of Reynolds numbers; nonetheless, at appointed Reynolds numbers, vortex formation may abide and other changes in the flow patterns betide. The flow has been classified into different Reynolds number regimes by various authors, such as Coutanceau and Defaye (1991) [43], Williamson (1996) [44], and Zdravkovich (1997) [42], pursuant to the boundary layer characteristics on the cylinder, aerodynamic forces, vortex formation, and flow structure. These are the Creeping flow ($Re < 5$), Attached eddies ($5 < Re < 40$), Laminar vortex shedding ($40 < Re < 350$), Subcritical regime ($350 < Re < 2 \times 105$), Critical regime ($2 \times 10^5 < Re < 7 \times 10^5$), Supercritical regime ($7 \times 10^5 < Re < 3.5 \times 10^6$), and Trans-critical regime ($Re > 3.5 \times 10^6$). In the addendum sections according to the Reynolds number of our filtration simulation study, laminar vortex shedding and subcritical regime are briefly reviewed.

1.6.1 Laminar Vortex Shedding, 40<Re<350

According to Reynolds number, the attached eddies become unstable and oscillation develops in the shear layers. The oscillation magnitude proliferates with Reynolds number to the point of the sudden inception of alternate vortex shedding. Then, the shear layers roll up alternately into vortices. These vortices are shed into the wake funning two rows of oppositely signed vortices known as a Karman vortex street (Figure 1.8). The Reynolds number at which this occurs is sensitive to experimental conditions like surface roughness and perturbations in the incoming flow. As the Reynolds number increases before Re =150, the shear layers commence the transition to turbulence until they roll up. Some authors have subdivided the regime at this point. This results in a discontinuity in the Strouhal frequencies at Re=180-190, which may depend on whether or not the Reynolds number is increasing or decreasing. A second discontinuity befalls at Re=230-260, contingent on experimental conditions, because of three-dimensional flow structures in the wake[44].

Figure 1.8 Laminar vortex shedding regime at $40 < Re < 350$ [43].

1.6.2 Subcritical Regime, 350<Re< 2×10^5

Coutanceau and Defaye (1991) [43] distinguished ten flow regimes in the range which was from $2,000 < Re < 1.5 - 2 \times 10^5$ as Regime 7. The ranges determined by a laminar boundary layer before separation and a quasi-constant separation angle of approximately 80°C measured from the front stagnation point (Figure 1.9). This is erred section of the subcritical regime, which can expand from $350 < Re < 2 \times 10^5$. In the subcritical regime, the transition waves in the two shear layers that border the wake become sufficiently large and roll up into small-scale vortices. The small-scale vortices are carried downstream by a fully turbulent Karman vortex street with a nearly permanent Strouhal number of $St{\sim}0.20$. As the Reynolds number increments, the small-scale vortices achieve to a descending vortex formation length. A shorter vortex formation length is affiliated with a larger vortex shedding frequency and slightly increased drag. The drag coefficient (C_D) is commonly 1.2, where $C_D = \frac{F_D}{0.5A\rho U^2}$ and F_D is the mean drag force and A is the cylinder frontal area.

For a smooth cylinder, skin friction drag contributes 1-2% to the total drag while pressure drag is responsible for the remaining 98% (Achenbach, 1968) [45].

Williamson (1996) determined the area from Re=1,000 to 2×10^5 as the shear-layer transition regime in which the vortex shedding behavior remains relatively constant. While this flow is nominally two-dimensional, in practice there exist three-dimensional structures in the separated shear layers as well as three-dimensional structures on the scale of the Karman vortex street[44].

15

Figure 1.9 Subcritical flow regimes at $350 < Re < 2 \times 10^5$ [42].

1.6.3   Summary of Flow Regime

In backbite of the above perturbations, the transition of the boundary layer is amenable mostly on the Reynolds number and body geometry. According to the accumulated experimental data about a circular cylinder, the flow regimes can be fully laminar or any of the three transitions or in fully turbulent states. Flow regimes based on Re and the characteristics of drag coefficient, along with the length of near-wake and length of eddy emergence have been ranked at the below table.

1.7   Vortex Shedding

Sumer and Fredsoe (1997) have presented a vortex shedding theory [46]. In a condition with $Re > 40$ flow, the boundary layer over the cylinder surface will separate owing to the adverse pressure gradient. This pressure gradient turns up due to the divergent environment of the flow at the rear side of the cylinder. As a result, a shear layer will be formed. The boundary layer along the cylinder contains a remarkable amount of vorticity. The vorticity fits to a shear layer downstream of the separation point and inures the shear layer to roll up into a vortex with a sign similar to that of the incoming vorticity, which is shown in Figure 1.10 a:
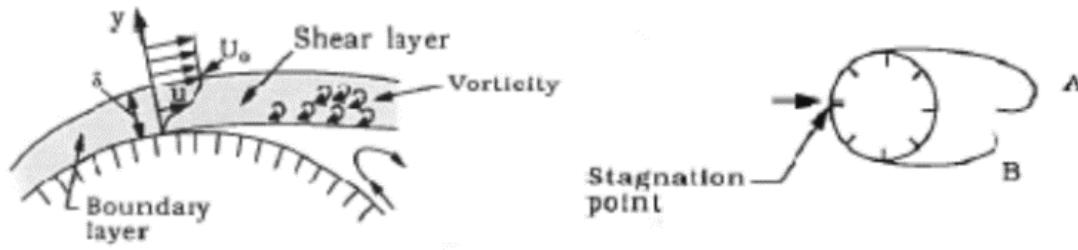
Figure 1.10 The boundary layer, the shear layer downstream of the cylinder and the beginning of the vortex shedding are illustrated, from [46].

(a) The detailed picture of flow near Separation

(b) Beginning of vortex shedding

1.8 The Mechanism of Vortex Shedding

The mechanism of vortex shedding can be portrayed in the following way. This is described by the help of Figure 1.10 and Figure 1.11. When the larger vortex becomes strong enough, it will draw the opposite vortex across the wake. This is projected in Figure 1.11 a. The vorticity in Vortex A is in the clockwise direction, while the vorticity in Vortex B is in the opposite direction. The vorticity with opposite sign (from Vortex B) will cut off the further supply of vorticity to Vortex A from its boundary layer; in this condition, Vortex A is shed. So Vortex A is a free vortex and will be connected downstream of the cylinder.

(a) Vortex B is drawn across   (b) Vortex C is drawn across
the wake before Vortex   the wake before Vortex
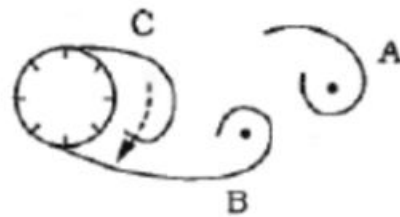
Figure 1.11 Illustration of vortex shedding from [46]

Now, a new vortex, named Vortex C, will be formed at the side of the cylinder where Vortex

A was settled. Vortex B will now have the same role as Vortex A had. It will develop in size

and strength and draw Vortex C across the wake until it is shed, and Vortex B is free, as

shown in Figure 1.11b. This alternating vortex shedding will continue to betide

between the two sides of the cylinder. The vortex shedding arises only when the shear

layers interact with each other.

1.9   Vortex-Shedding Frequency

In order to discover the Strouhal number St, the vortex-shedding period was found from the

plot for the lift coefficient. It can also be found from the oscillating pressure or velocities in a

probe in the wake near the cylinder. The vortex shedding frequency, f_u, is given by

$$f_u = \frac{1}{T_u} \qquad\qquad (1\text{-}19)$$

Normalization of the flow velocity U_c and the cylinder diameter D would be occur by vortex

shedding frequency, named Strouhal number and is computed by the formula

$$St = \frac{f_u D}{U_c} \qquad\qquad (1\text{-}20)$$

The Strouhal number varies with the Reynolds number $St = St\ (Re)$.

Figure 1.12 indicates how the Strouhal number varies with Reynolds number.
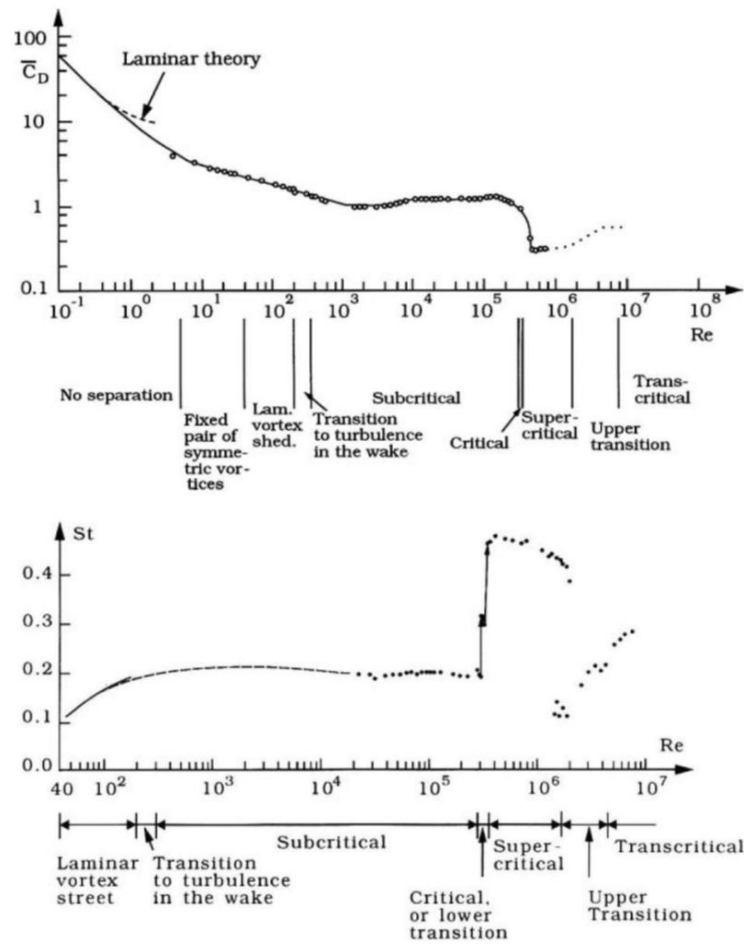
Figure 1.12 Strohal number for a smooth circular cylinder. Different curve types (solid, dashed, dots) are from different experiments. The figure is found in [46].

19

Vortex shedding, for the first time begins at $Re = 40$, then it increases gradually when Re is increased until it remains approximately constant at $Re = 300$, which is the lower end of the subcritical flow regime. This magnitude of the Strouhal number remains throughout the subcritical range. It can be seen from Figure 1.12 that the Strouhal number experiences a sudden jump in value at $Re = 3 - 3.5 \times 10^5$, which is named the critical range of Re. Here, the Strouhal number has a value of about 0.45. This high value of St has remained for a large part of the supercritical Re range, but it decreases slightly with increasing Re. The reason for explaining the sudden jump in Strouhal number is that boundary layer on both sides of the cylinder is turbulent at the separation point. The result is that the separation point moves downstream. This means that the alternating vortices will interact with each other at a faster rate, meaning the vortex shedding frequency increases which leads to an increase of Strouhal number.

1.10 Dependence of Pressure and Force on Flow Characteristics

The effects of viscosity of the fluid are relevant only within a thin layer near the surface of a structure. The flow outside the layer region is pondered as inviscid. Howbeit, in many cases, this small viscosity governing region plays an important role in the formation of boundary layers. The presence of a boundary layer is associated with gently decreasing flow velocity near a surface, where the velocity vanishes. Flows in the boundary layer may detach from the surface and significantly alter the flow field around it. Figure 1.13 shows the velocity profiles and pressure gradients near a curved surface. The free stream velocity U is approaching to the structure, the x and y coordinates are tangent and normal to the surface of the structure, respectively. The flow propagates its velocity $U(x)$ out of a boundary layer along the $x-direction$ because of converging streamlines at the upstream region, which results in the

decrease of pressure with x. Beyond the point of the maximum velocity of $U(x)$, the streamlines diverge. This eventually causes the velocity to decrease and the pressure to increase. In the region of increasing velocity flow, the curvature of a velocity profile $u(x, y)$ is given by

$$\frac{\partial^2 u}{\partial y^2} < 0 \text{ at wall} \tag{1-21}$$

Where u is the velocity profile normal to the surface in the boundary layer. On the other hand, in the region of decreasing-velocity flow, the curvature of the velocity profile in the boundary layer is

$$\frac{\partial^2 u}{\partial y^2} > 0 \text{ at wall} \tag{1-22}$$

Since the velocity profiles have opposite curvatures downstream, a point of inflection where $\frac{\partial^2 u}{\partial y^2} = 0$ exists in the region of velocity-decreasing flow. The thickness of the boundary layer enhances downstream, which is caused by the effect of decreasing pressure gradient due to the shape of the bluff body. Under a high adverse pressure gradient, the flow velocity reverses direction. A region of backward flow happens from the detachment of the boundary layer. This is known as "separation." This is an important phenomenon in bluff-body aerodynamics.
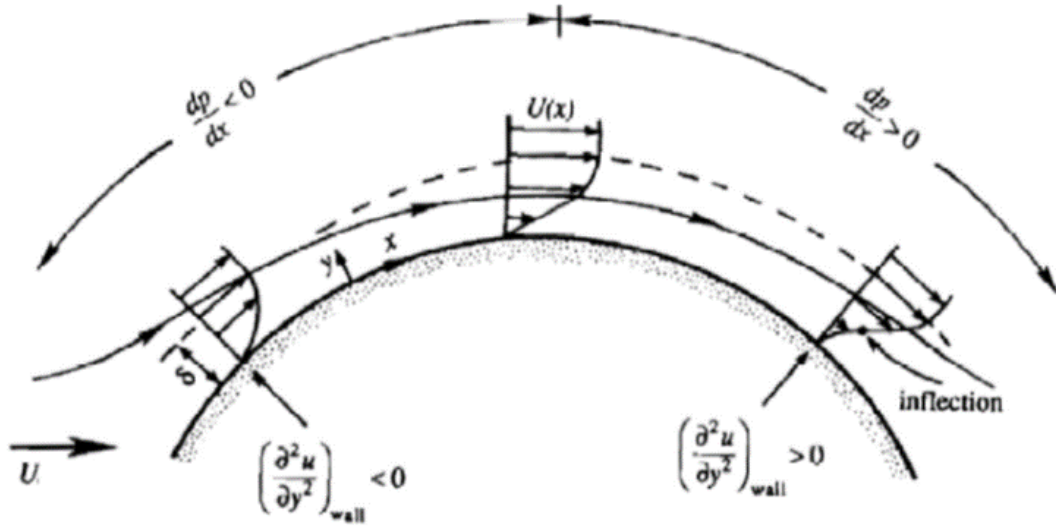
Figure 1.13 Velocity profiles across boundary layers on a smoothly curved surface (Kundu and Cohen 2004) [47]

Figure 1.14 demonstrates an inflection and a separation of the flow. The inflection and separation point are indicated by I and S, respectively. The separation point is indicated as below:

$$\frac{\partial^2 \partial u}{\partial y} = 0 \tag{1-23}$$

Since the separation of a boundary layer befalls when the flow is sufficiently decelerated by inertial forces because of the adverse pressure gradients along the surface, the relationship between inertial and viscous effects is an important descriptor of flow characteristics.

22
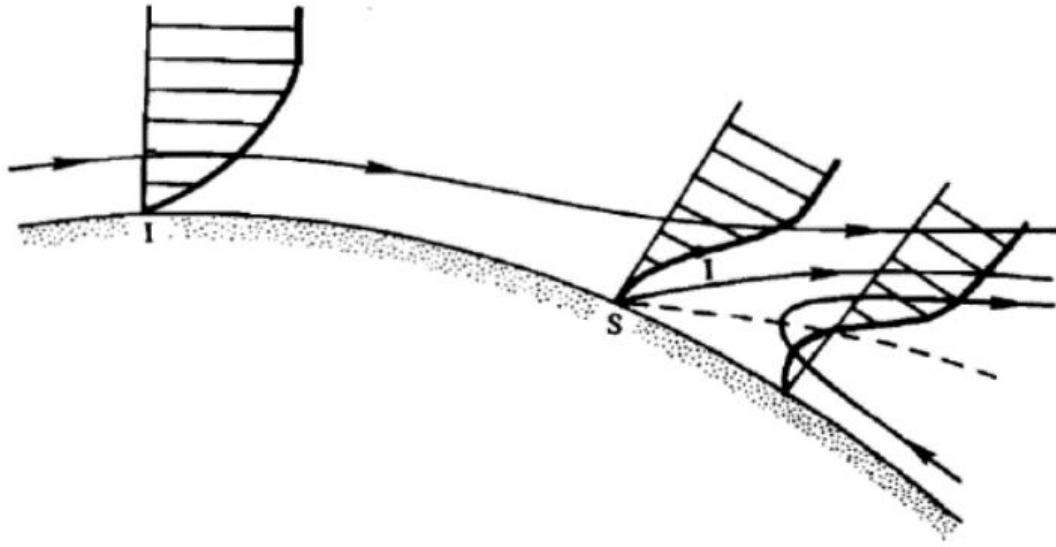
Figure 1.14 Streamlines and velocity profiles near a separation point [47].

For example, flow around a circular cylinder follows the cylinder contours at $Re = 5$, but the flow gets separated from the cylinder surface and develops a fully turbulent vortex street at $300 < Re < 3 \times 10^5$. Figure 1.15 represents the variation of mean drag coefficient and the fluctuation of the lift coefficient of a smooth circular cylinder according to Reynolds number. It demonstrates that the forces of the circular cylinder are strongly dependent on the Reynolds number. The drag coefficient of a smooth cylinder suddenly drops in the range of $2 \times 10^5 \leq Re \leq 5 \times 10^5$. This is recognized as "drag crisis" in the critical regime. It eventuates from the transition of the laminar to turbulent flow in a boundary layer ahead of a separation point on the surface of the cylinder. This entails the separation point to move leeward. The delay in separation leads to narrowing of the wake, a decreased (less negative) base pressure in the wake; therefore, the drag coefficient reduces. Figure 1.15a indicates that the time-averaged drag coefficient proliferates in the super-critical and the trans-critical regime as the Reynolds number increases. Although, the drag coefficient remains much lower in the super- or Trans-

critical regime than in the sub-critical regime. The oscillation of lift coefficient also changes dramatically with the Reynolds number as illustrated in Figure 1.15b.

(a) Drag coefficient [105]   (b) Lift coefficient
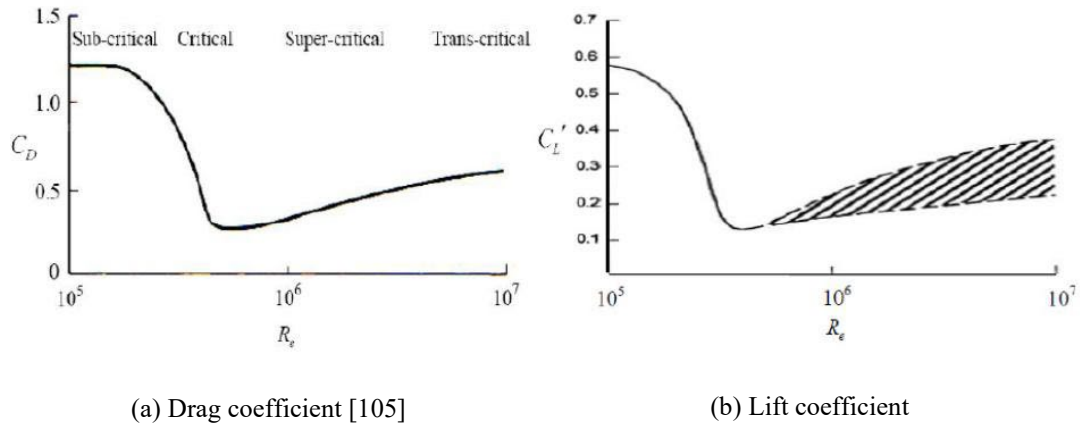
Figure 1.15 Variation of (a) mean drag coefficient and (b) fluctuating lift coefficient with Reynolds number for a smooth circular cylinder

Figure 1.16 represents that pressure distribution over a circular cylinder is sensitive to Reynolds number. The separation point of the flow in the super-critical regime (Re=7×10^5) is located at a large angle from the stagnation point in comparison with that in the sub-critical regime (Re=2×10^5). The shifted separation angles, owing to the Reynolds number effect, noticeably affect the flow-induced pressure and forces on the circular cylinder.
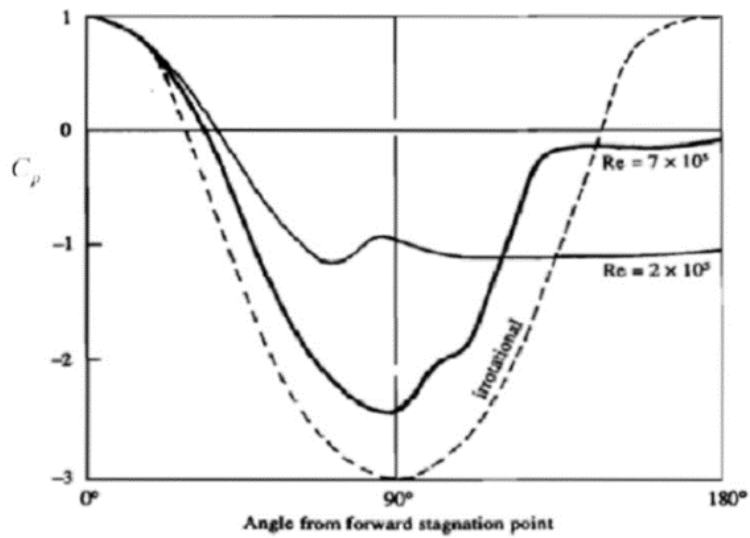
Figure 1.16 Influence of Reynolds number on pressure distribution over a circular cylinder [47].

1.11 Lift and Drag Concepts

When an object moves through a fluid, an interaction between the object and the fluid outcrops; this effect can be given for the forces at the fluid-body interface. These forces can be explained in terms of the stresses-wall shear stresses, because of the viscous effects and normal stresses due to the pressure, p. Typical shear stress and pressure distributions are displayed in Figure 1.17a and Figure 1.17b. Both τ_w and p vary in magnitude and direction along the surface.
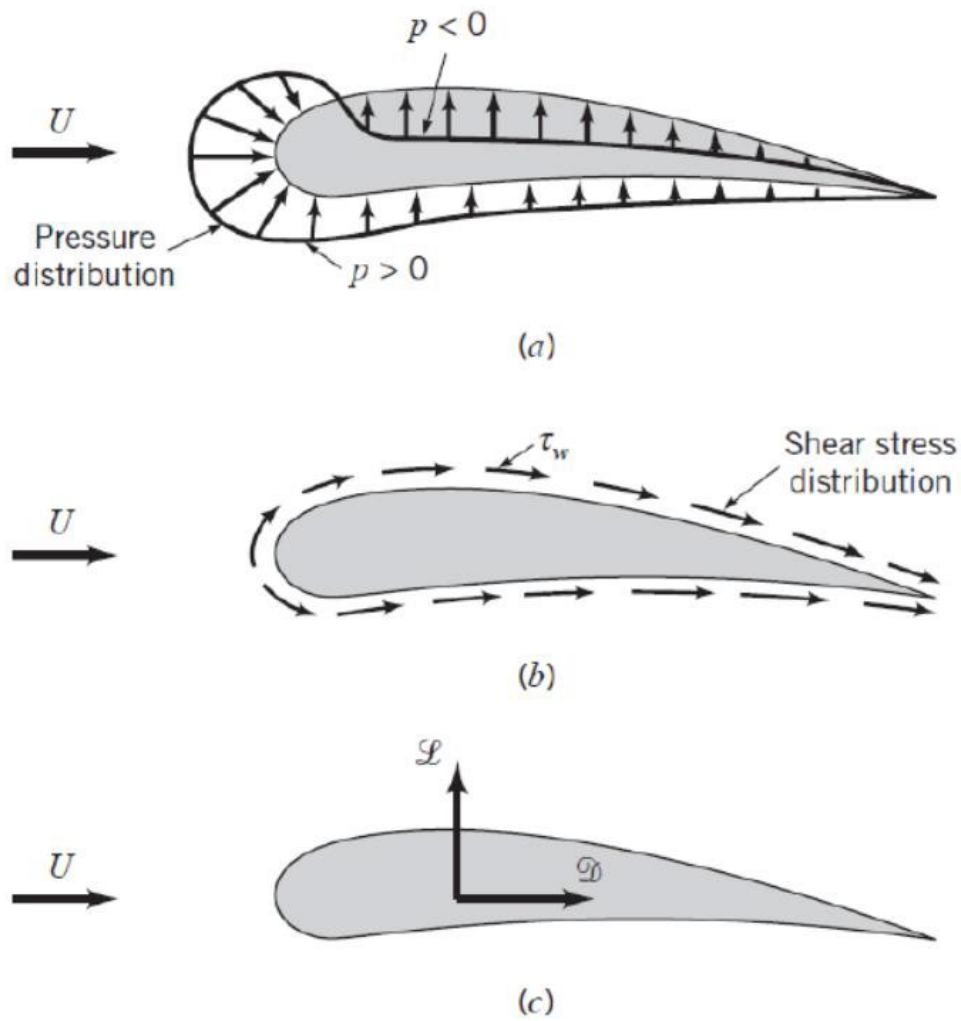
Figure 1.17 Forces from the surrounding fluid on a two-dimensional object:

(a) Pressure force, (b) viscous force, (c) resultant force (lift and drag) [48]

It is often practical to know the precise distribution of shear stress and pressure over the surface of the body, albeit such information is arduous to obtain.
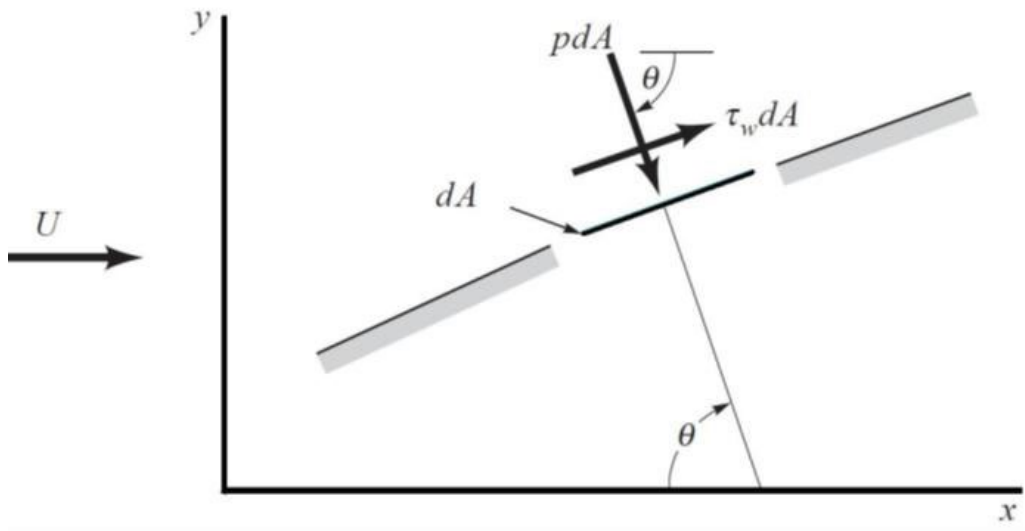
Figure 1.18 Pressure and shear forces on a small element of the surface of a body [48].

Many times, howsoever, only the integrated or resultant effects of these distributions are required. The illative force in the direction of the upstream velocity is termed the drag, and the resultant force normal to the upstream velocity has denominated the lift as indicated in Figure 1.17c. For some three-dimensional bodies there may also be a side force that is perpendicular to the plane containing D and L. Likewise, there may be a side force that is perpendicular to the plane containing and the resultant of the shear stress and pressure distributions can be obtained by integrating the effect of these two quantities on the body surface as indicated in Figure 1.18.

The x and y components of the fluid force on the small element dA are

$$dF_x = (pdA) \cos \theta + (\tau_w dA) \sin \theta \qquad (1\text{-}24)$$

And

$$dF_y = -(pdA) \sin\theta + (\tau_w dA)\cos\theta \qquad (1\text{-}25)$$

Afterward, the net x and y components of the force on the object are

$$D = \int dF_x = \int p\cos\theta dA + \int \tau_w \sin\theta dA \qquad (\,1\text{-}26\,)$$

And

$$L = \int dF_y = -\int p\sin\theta dA + \int \tau_w \cos\theta dA \qquad (\,1\text{-}27\,)$$

Needless to say, to carry out the integrations and determine the lift and drag, we must know the body shape and the distribution of τ_w and p along the surface. These repartitions are often extremely formidable to procure, either experimentally or theoretically. The pressure distribution can be achieved experimentally by the use of a series of static pressure taps along the body surface. On the other side, it is usually quite inexplicable to measure the wall shear stress distribution.

Howsoever, Equations 1.29 and 1.30 are valid for any object; the hardness in their use lies in obtaining the appropriate shear stress and pressure distributions on the body surface. Considerable endeavor has gone into determining these quantities, but due to the various complexities involved, such information is available only for specified simple situations. Without subtle information, concerning the shear stress and pressure distributions on a body, Equations 1.29 and 1.30 cannot be used. The broadly used alternative is to define dimensionless lift, drag coefficients, and assess their approximate values by the means of a simplified analysis, some numerical techniques, or an appropriate experiment. The lift coefficient and drag coefficient are defined as

$$C_L = \frac{L}{0.5\rho AU^2} \qquad (\,1\text{-}28\,)$$

and

$$C_D = \frac{D}{0.5\rho AU^2} \qquad (\,1\text{-}29)$$

where *A* is the characteristic of the frontal area of the object. Frontal area is the projected area seen by a person looking from a parallel direction to the upstream velocity, *U*. It would be the area of the shadow of the object projected onto a screen normal to the upstream velocity as formed by a light shining along with the upstream flow. In other situations, *A* is taken to be the plane form area of the projected area seen from a normal direction to the upstream velocity. Indubitably, the characteristic area used in the definition of the lift and drag coefficients must be clearly stated [48].

1.11.1 Drag

Any object moving through a fluid will experience a drag, a net force in the direction of flow owing to the pressure and shear forces on the surface of the object. This net force, a combination of flow direction components of the normal and tangential forces on the body, can be determined by the help of Equations 1.29 and 1.30, maintained the distributions of pressure, and wall shear stress (τ_w). These distributions are determined analytically in a few cases. Most of the information coherent to drag on objects is an outcome of numerous experiments with wind tunnels, water tunnels, towing tanks, and other ingenious devices that are used to measure the drag on scale models.

Dimensionless form and the consequences can be appropriately radioed in prototype calculations. In some cases, the outcome for a given-shaped object is a drag coefficient, where is a function of other dimensionless parameters such as Reynolds

number, Re, Mach number, Froude number, Re, and the relative roughness of the surface, That is:

$$C_D = \emptyset(Shape, Re, Ma, Fr, \frac{\varepsilon}{l})$$ (1-30)

1.12 Multi-phase Flow

Any fluid flow consisting of more than one phase or component is named multiphase flow. For briefness and because they are enclosed in other texts, those circumstances are eliminated in which the components are well mixed above the molecular level. Therefore, the flows considered have some level of phase or component leave-taking at a scale fine overhead the molecular level. This still greeneries (verb?) an enormous range of different multiphase flows. One could categorize them discussing to the state of the different phases or components and therefore refer to gas/solids flows, or liquid/solids flows or gas/particle flows or bubbly flows and so on.[49]

Others focus attention on a specific application such as slurry flows, cavitating flows, aerosols, debris flows, and fluidized beds and so on; again there are many such texts. Almost every processing technology must deal with the multiphase flow, from cavitating pumps and turbines to electrophotographic processes to papermaking to the pellet form of almost all raw plastics.

The skill to guess the fluid flow behavior of these processes is necessary to the efficiency and effectiveness of the processes. For example, the effective flow of toner is a major factor in the quality and the speed of electrophotographic printers.[49] Multiphase flows are also a universal feature of our environment whether one considers rain, snow, fog, avalanches, mudslides, sediment transport, debris flows, and numerous other natural phenomena to say

30

nothing of what occurs outside the world. Very serious natural and medical flows are multiphase, from blood flow to semen to the bends to lithotripsy to laser surgery cavitation and so on[50]. No single list can adequately illustrate the diversity and ubiquity; consequently, any attempt at a comprehensive treatment of multiphase flows is flawed unless it focuses on common phenomenological themes and avoids the temptation to digress into lists of observations.

Disperse flows and separated flows are two basic topologies of multiphase flow which can helpfully be recognized at the outset. Disperse flows mean containing onfinite particles, drops or bubbles (the disperse phase) distributed in a linked volume of the continuous phase. On the other hand, separated flows consist of two or more continuous streams of different fluids separated by interfaces.

1.12.1 Multiphase Flow Models

A determined theme throughout the study of multiphase flows is the need to model and guess the detailed behavior of those flows and the phenomena that they manifest. There are three ways in which such models are explored:

1) Experimentally, through laboratory-sized models equipped with suitable equipment, 2) Theoretically, using mathematical equations and models for the flow, and 3) Computationally, using the power and size of modern computers to report the difficulty of the flow. Obviously, there are some applications in which full-scale laboratory models are possible. But, in many examples, the laboratory model must have a very different scale than the sample and then a reliable theoretical or computational model is critical for confident

extrapolation to the scale of the prototype. There are also cases in which a laboratory model is impossible for a wide variety of reasons.[49]

Consequently, the analytical competence and physical understanding are deeply based on the theoretical and/or computational models as the complexity of most multiphase flows presents a major hurdle. It may be possible at some reserved time in the future to code the Navier-Stokes equations for each of the phases or components and to compute every detail of multiphase flow, the motion of all the fluid around and inside every particle or drop, and the position of every interface. But the computer power and speed required to do this is far beyond the present capability for most of the flows that are commonly experienced. When one or both of the phases become turbulent (as often happens) the magnitude of the challenge becomes truly astronomical. Therefore, simplifications are essential in realistic models of most multiphase flows.[51]

In scatter flows two types of models are dominant, *trajectory models* and *two-fluid models*. In trajectory models, the motion of the disperse phase is measured by following either the motion of the actual particles or the motion of larger, representative *particles*. The details of the flow around each of the particles are included in expected drag, lift and moment forces acting on and changing the trajectory of those particles. The thermal history of the particles can also be tracked if it is appropriate to do so. Trajectory models have been very useful in studies of the rheology of granular flows primarily because the effects of the interstitial fluid are small.

 In other methods, two-fluid models, the disband phase is treated as a second continuous phase intermixed and interacting with the continuous phase. Effective conservation equations (of mass, momentum, and energy) are established for the two fluid flows; these included

interaction terms modeling the exchange of mass, momentum, and energy between the two flows. These equations are solved in two methods, theoretic and computation. Thus, the two-fluid models neglect the discrete nature of the disperse phase and estimate its effects upon the continuous phase. Inherent in this approach are averaging processes necessary to characterize the properties of the disperse phase; these involve significant difficulties. The boundary conditions appropriate in two-fluid models also pose difficult modeling issues. [49]

In opposition, separated flows present many fewer matters. In theory one must solve the single-phase fluid flow equations in the two streams, coupling them through suitable kinematic and dynamic conditions at the interface. Free streamline theory is a sample of successful execution of such a strategy through the interface conditions used in that setting which are chiefly simple [52]–[54]

1.12.2 Conservative Level Set Method for Two Phase Flow

Problems containing moving boundaries and interfaces occur in a wide range of applications, such as multi-phase flow, crystal growth, fluid–structure interactions, etc. Different ways to simulate these problems have been established. Front tracking methods and level set methods for incompressible flows volume of fluid methods are used frequently.

In the simulation of incompressible a two-phase flow, the method which has been used widely is the volume of fluid (VOF). In these methods, the interface is given discreetly by a color function, well-defined to be the fraction of volume in each cell of one of the fluids. From the color function, a reconstruction of the interface is completed and the interface is then promulgated implicitly by updating the color function. VOF methods are conservative and can engage with topological changes in the interface. Though, they are frequently inaccurate,

achieving a high order of accuracy is hard because of the discontinuity of the color function. No advection scheme for the volume of the fluid method has an order higher than two. In addition, calculating properties of the interface like normal and curvature accurately is hard. Still, the good conservation properties are attractive and quite sophisticated methods have been developed. [55].

Another method for free boundary problems is the determination of the trajectory of the boundary, which has been explicitly and lightly distributed by markers on the interface, and the propagation of the markers. The interface can be represented sharply. In this way, this form of methods is frequently referred to as front tracking methods. Markers can move closely together or far apart, making redistribution of markers is needed. Distinct attention has to be taken to topological changes. Also, if the markers move self-sufficiently of each other, oscillations in the interface may happen.

Added trouble is the interaction of the interface with a fixed Eulerian grid. All these features make front tracking methods tough to implement for a general case [56]. A method to simulate multi-fluid flows using front tracking is described in [56]. Recently, level set methods have become common and have been used in a large range of applications such as compressible and incompressible two-phase flow, image processing and flame propagation. General reports of level set methods can be found in [57][58] and applications to two-phase flow are represented in [59], [60]. Generally, the interface is signified by the zero contour of a signed distance function, and the level set function. The movement of the interface is investigated by a differential equation for the level set function. The advection is in general done by (weighted) essentially non-oscillatory (WENO, ENO) methods [56]. To preserve the level set function a signed distance function, or a reinitialization process is needed [56]. Similarly, this method is governed by a differential equation. Level set methods automatically

agree with topological changes and it is easy to get high order of accuracy, just by selecting an ENO or WENO scheme with the wanted order of accuracy.

1.12.3 Incompressible Two-Phase Flow

Advection method for the phase field function is coupled with a two-phase incompressible flow solver. Diffuse interface model is being used, where surface tension is changed to a volume force spread over a few layers of cells. The discontinuity in density and viscosity across the interface is also smoothed out [56].

Surface tension per interfacial area at a point $\vec{x}_I$ on the interface is given by

$$\vec{F}_{sa}(\vec{x}_I) = \sigma\kappa(\vec{x}_I)\hat{n}(\vec{x}_I) \qquad (1\text{-}31)$$

Where $\kappa = -\nabla.\left(\frac{\nabla\Phi}{|\nabla\Phi|}\right)$ and $\hat{n} = \frac{\nabla\Phi}{|\nabla\Phi|}$ as in [13]. Choosing a volume force at any point $\vec{x}$ as

$$\vec{F}_{sv}(\vec{x}) = \sigma(-\nabla.\frac{\nabla\Phi}{|\nabla\Phi|})\nabla\Phi \qquad (1\text{-}32)$$

will result in the total force as $\vec{F}_{sa}(\vec{x}_I)$, however, grew over the finite interface width. Now, it becomes significant that the thickness of the transition layer is retained constantly. $\vec{F}_{sv}$ is equal to $\vec{F}_{sa}(\vec{x}_I)$ only in the limit when the thickness of the interface goes to zero[13]. If the interface becomes widespread, $\vec{F}_{sv}$ will not be a good guesstimate of $\vec{F}_{sa}(\vec{x}_I)$. Consequently, the interface thickness should not become wide. Too sharp transition, on the other side, will produce complications in numerically computing $\vec{F}_{sv}$, since up to second order derivatives of Φ are needed.

Assume the interface is advected with a given velocity field $\vec{u}$. This corresponds to the following simple ordinary differential equation for every point $\vec{x}$ on the interface as follows:

$$\frac{d\vec{x}}{dt} = \vec{u}(\vec{x})$$

(1-33)

As in standard level set methods, we can instead solve advect Φ which is conservative and does not change the profile of Φ at the interface.

$$\Phi_t + \vec{u}.\nabla\Phi = 0$$

(1-34)

The dimensionless incompressible Navier–Stokes equations with surface tension and gravity are:

$$\nabla.\vec{u} = 0$$

(1-35)

$$\vec{u}_t + (\vec{u}.\nabla)\vec{u}_t = -\frac{\nabla p}{\rho} + \frac{1}{\rho Re}\nabla.\left(\mu(\nabla\vec{u} + (\nabla\vec{u})^T)\right) + \frac{1}{Fr^2}\vec{e}_g + \frac{1}{\rho We}\tilde{F}_{sv}$$

(1-36)

$$\Phi_t + \vec{u}.\nabla\Phi = 0$$

(1-37)

Where $Re = \frac{\rho_{ref}u_{ref}l_{ref}}{\mu_{ref}}$ is the Reynolds number, $Fr = \frac{u_{ref}}{\sqrt{l_{ref}g}}$ is the Froude number, $We = \frac{\rho_{ref}u_{ref}^2 u_{ref}}{\sigma}$ is the Weber and $\tilde{F}_{sv} = \frac{\vec{F}_{sv}}{\sigma\vec{e}_g}$ is the unit vector in the direction of gravitation and ρ and μ are the non-dimensionalized density and viscosity, individually. The density and viscosity fluctuate smoothly over the interface by letting:

$$\rho = \rho_1 + (\rho_2 - \rho_1).\Phi$$

(1-38)

$$\mu = \mu_1 + (\mu_2 - \mu_1).\Phi$$

(1-39)

ρ_1, ρ_2 and μ_1, μ_2 are the non-dimensional densities and viscosities of the two fluids.

A staggered grid is used for the discretization, i.e., Φ and p are given at grid points $\vec{x}_{i,j}$, whereas u is given on $\vec{x}_{i+1/2,j}$ and v on $\vec{x}_{i+1/2,j}$ [55].

1.13 Electrostatics and Electromagnetics

1.13.1 Electrostatics

The results of Faraday`s experiments with the concentric spheres could be summed up as an experimental law by stating that electric flux passing through an imaginary spherical surface lying between the two conducting spheres is equal to the charge enclosed within that imaginary surface. This enclosed charge is distributed on the surface of the inner sphere, or it might be concentrated as a point charge at the center of the imaginary sphere. However, since one coulomb of electric flux is produced by one coulomb of charge, the inner conductor might just as well have been a cube or a brass door key and the total induced charge on the outer sphere would still be the same. Certainly, the flux density would change from its previous symmetrical distribution to some unknown configuration, but $+Q$ coulombs on any inner conductor would produce an induced charge of $-Q$ coulombs on the surrounding sphere. Going one step further, now two outer hemispheres could be replaced by an empty (but completely closed) soup can. Q coulombs on the brass door key would produce $\Psi = Q$ lines of electric flux and would induce $-Q$ coulombs on the thin can. [61]

These generalizations for Faraday`s experiment lead to the following statement, which is known as Gauss`s law:

The electric flux passing through any closed surface is equal to the total charge enclosed by that surface.

The contribution of Gauss was not actually in stating the law as mentioned above, but in providing a mathematical form for this statement, which is obtained.

Distribution of charge is imagined and shown as a cloud of point charges in Figure 1.19 surrounded by a closed surface of any shape which we wish to visualize. If the total charge is Q, then Q coulombs of electric flux will pass through the enclosing surface. At every point on

the surface, the electric-flux-density vector $\boldsymbol{D}$ will have some values of $\boldsymbol{D_S}$, where the subscript S merely reminds us that $\boldsymbol{D}$ must be evaluated at the surface, and $\boldsymbol{D_s}$ will in general, varies in magnitude and direction from one point on the surface to another point.[62]
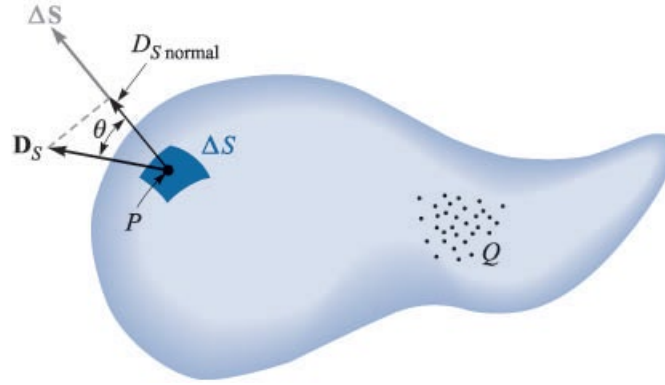
Figure 1.19 The electric flux density $\boldsymbol{D_s}$ at P due to charge Q. The total flux passing through $\Delta\boldsymbol{S}$ is $\boldsymbol{D_s} . \Delta S$ [62]

The nature of an incremental element of the surface must be considered. And the incremental element of area ΔS is very nearly a portion of a plane surface, and the complete description of this surface element requires not only a statement of its magnitude ΔS but also of its orientation in space. On the other hand, the incremental surface element is a vector quantity. The only unique direction which may be associated with ΔS is the direction of the normal to that plane which is tangent to the surface at the point in question. There are, two such normals, and ambiguity is removed by specifying the outward normal whenever the surface is closed and "outward" has a specific meaning.

At any point P is considered as an incremental element of surface ΔS while $\boldsymbol{D_S}$ makes an angle θ with ΔS, as shown in Figure 1.19. The flux crossing ΔS is the product of the normal component of $\boldsymbol{D_S}$ and ΔS as follows:

$$\Delta\Psi = flux\ crossing\ \Delta S = \boldsymbol{D_{S,norm}}\Delta = \boldsymbol{D_S}Scos\theta\Delta S = \boldsymbol{D_S}.\Delta S \qquad (1\text{-}40)$$

The total flux passing through the closed surface is obtained by adding the differential constitutions crossing each surface element ΔS,

$$\Psi = \int d\Psi = \oint_{\substack{closed \\ surface}} \boldsymbol{D_S} . dS \qquad (1\text{-}41)$$

And the mathematical formulation of Gauss`s law is:

$$\Psi = \oint_S \boldsymbol{D_S} . dS = charge\ enclosed = Q \qquad (1\text{-}42)$$

The charge enclosed might be several point charges, in which case

$$Q = \sum Qn \qquad (1\text{-}43)$$

Or a line charge,

$$Q = \int \rho_L dL \qquad (1\text{-}44)$$

Or volume charge

$$Q = \int \rho_v dv \qquad (1\text{-}45)$$

Gauss`s law may be written in terms of the charge distribution as:

$$\oint_S D_s . dS = \int_{vol} \rho_v dv \qquad (1\text{-}46)$$

Which means that the total electric flux through any closed surface is equal to the charge enclosed.

1.13.1.1 Maxwell`s First Equation (Electrostatics)

Definition of divergence is:

$$div\ D = \lim_{\Delta v \to 0} \frac{\oint_S D.dS}{\Delta v} = \frac{\partial D_x}{\partial x} + \frac{\partial D_y}{\partial y} + \frac{\partial D_z}{\partial z} \qquad (1\text{-}47)$$

For given Gauss`s law,

$$\oint_S A \cdot dS = Q \qquad (1\text{-}48)$$

and for per unit volume:

$$\frac{\oint_S A.dS}{\Delta v} = \frac{Q}{\Delta v} \qquad (1\text{-}49)$$

As the volume shrinks to zero,

$$\lim_{\Delta v \to 0} \frac{\oint_S A.dS}{\Delta v} = \lim_{\Delta v \to 0} \frac{Q}{\Delta v} \qquad (1\text{-}50)$$

The left side is equal to div D and the right side is equal to volume charge density,

$$div\ \boldsymbol{D} = \rho_v \qquad (1\text{-}51)$$

This is the first of Maxwell`s four equations as they are applied to electrostatics and steady magnetic fields, and it states that electric flux per unit volume leaving a vanishingly small volume unit is exactly equal to the volume charge density there. This equation is aptly called the point form of Gauss`s law. Gauss`s law relates the flux leaving any closed surface to the charge enclosed, and Maxwell`s first equation makes an identical statement on a per-unit-volume basis for a vanishingly small volume, or at a point. [62]

1.13.2 Electromagnetics

In constructing the electrostatics model, an electric field vector, **E**, and an electric flux density (electric displacement) vector, **D,** are modeled. The fundamental governing differential equations are

$$\nabla \times \boldsymbol{E} = \boldsymbol{0} \qquad (1\text{-}52)$$

$$\nabla . \boldsymbol{D} = \rho \qquad (1\text{-}53)$$

For linear and isotropic media $\boldsymbol{E}\ and\ \boldsymbol{D}$ are related by a constitutive relation

$$\boldsymbol{D} = \epsilon \boldsymbol{E} \tag{1-54}$$

For the magneto-static model, we define a magnetic flux density vector, $\boldsymbol{B}$, and a magnetic field intensity vector, $\boldsymbol{H}$. The fundamental differential equations are

$$\nabla . \boldsymbol{B} = 0 \tag{1-55}$$

$$\nabla \times \boldsymbol{B} = \boldsymbol{J} \tag{1-56}$$

The constitutive relation for $\boldsymbol{B}$ and $\boldsymbol{H}$ in linear and isotropic media is

$$\boldsymbol{H} = \frac{1}{\mu} \boldsymbol{B} \tag{1-57}$$

It is observed that, in the stationary case, electric field vectors $\mathbf{E}$ and $\boldsymbol{D}$ and magnetic fields vectors $\boldsymbol{B}$ and $\boldsymbol{H}$ form separate and independent pairs. In other words, $\mathbf{E}$ and $\boldsymbol{D}$ in the electrostatic model are not related to $\boldsymbol{B}$ and $\boldsymbol{H}$ in the magneto-static model. In a conducting medium, static electric and magnetic fields may both exist and form an electro-magneto-static field. A static electric field in a conducting medium causes a steady current to flow that, in turn, gives rise to a static magnetic field. However, the electric field can be completely determined by static electric charges or potential distributions.

1.13.2.1 Maxwell Equations

The fundamental postulate for electromagnetic induction assures us that a time-varying magnetic field gives rise to an electric field. This assurance has been amply verified by numerous experiments. The $\nabla \times \mathbf{E} = 0$ equation should be replaced by $\nabla \times \boldsymbol{E} = -\frac{\partial \boldsymbol{B}}{\partial t}$. It shows that the electric field intensity in a region of time-varying magnetic flux density is therefore non-conservative and cannot be expressed as the gradient of a scalar potential. Following is the revised set of two curls and two divergence equations which are shown in the previous section:

$$\nabla \times \boldsymbol{E} = -\frac{\partial \boldsymbol{B}}{\partial t},$$ (1-58)

$$\nabla \times \boldsymbol{H} = \boldsymbol{J}$$ (1-59)

$$\nabla . \boldsymbol{D} = \rho$$ (1-60)

$$\nabla . \boldsymbol{B} = 0$$ (1-61)

In addition, we know that the principle of conservation of charge must be satisfied at all times. The mathematical expression of charge conservation is the equation of continuity:

$$\nabla . \boldsymbol{J} = -\frac{\partial \rho}{\partial t}$$ (1-62)

Finally, we have

$$\nabla \times \boldsymbol{H} = \boldsymbol{J} + \frac{\partial \boldsymbol{D}}{\partial t}$$ (1-63)

Above equation indicates that a time-varying electric field will give rise to the magnetic field, even in the absence of current flow.

It is easy to verify that $\frac{\partial \boldsymbol{D}}{\partial t}$ has the dimension of a current (SI unit: A/m^2). The term $\frac{\partial \boldsymbol{D}}{\partial t}$ is called displacement current density, and its introduction in the $\nabla \times \boldsymbol{H}$ equation was one of the major contributions of James Clerk Maxwell (1831-1879).

Maxwell equations are as follows:

$$\nabla \times \boldsymbol{E} = -\frac{\partial \boldsymbol{B}}{\partial t}$$
(1-64)

$$\nabla \times \boldsymbol{H} = \boldsymbol{J} + \frac{\partial \boldsymbol{D}}{\partial t}$$ (1-65)

$$\nabla . \boldsymbol{D} = \rho$$ (1-66)

$$\nabla . \boldsymbol{B} = 0$$ (1-67)

Note that ρ in Eq. (1-66) is the density of free charges, and J is the density of free currents, which may comprise both convection current ($\rho \boldsymbol{u}$) and conduction current ($\sigma \boldsymbol{E}$).

These four equations, together with the equation of continuity ($\nabla.\boldsymbol{J} = -\frac{\partial \rho}{\partial t}$) and Lorentz`s force equation ($\boldsymbol{F} = q(\boldsymbol{E} + \boldsymbol{u} \times \boldsymbol{B})$), form the foundation of electromagnetic theory.

Although Maxwell`s equations are consistent, they are not all independent. As a matter of fact, the two divergence equations, can be derived from the two curl equations by making use of the equation of continuity [63].

1.14 Wetting and Surface Force

The analysis of wetting of a solid or a liquid surface touches many fields, from the physical chemistry of surfaces and interfaces to thermodynamics, materials science, and physics of fluids. The wetting phenomenon plays a key role in many modern technologies such as brazing and soldering, three-dimensional printing, tissue engineering, surface coating and cleaning, microelectronics, optical and optoelectronic technology, and many others.

The conditions of the equilibrium in heterogeneous systems, which can be derived with accounting for the peculiarities of transition zones in two- and three-phase systems, are connected with the manifestation of surface forces of the first and the second kind. The distinguishing between the two kinds of surface forces was considered in Chapter 2.1 of the monograph by Derjaguin, Churaev, and Muller [64]. Briefly, the surface forces of the first kind, acting on the molecules at the vicinity of a single interface between two bulk phases, are responsible for the appearance and for the equilibrium value of the interfacial tension. Forces due to the effects of the overlap of two interfacial regions, confining a thin layer, in the course of surfaces approaching, refer to the surface forces of the second kind. Thus, the surface forces of the second kind are acting between the two interfaces, separated by a fluid interlayer, no part of which retains the intensive properties of the bulk phase. Derjaguin

showed that the analysis of the surface forces of the second kind can be performed by consideration of the dependence of the disjoining pressure $\Pi(h)$ on the film thickness h [64]:

$$\Pi(h) = P_N(h) - P_b \qquad\qquad (1\text{-}68)$$

In Eq. (1), $P_N(h)$ is the normal component of the pressure tensor in the thin interlayer of thickness h and P_b is the pressure in a bulk isotropic liquid which is in the equilibrium with the interlayer considered. On the other hand, the overlap of the transition regions results in the appearance of excess Gibbs free energy of the interlayer induced by above overlapping. Thus, the disjoining pressure or the surface forces per unit of film area may be defined as[64]:

$$\Pi(h) = -\left(\frac{\partial G}{\partial h}\right)_{T,P,\mu_i} \qquad\qquad (1\text{-}69)$$

Where G is the Gibbs free energy per unit of the interlayer area, T and P are the temperature and the pressure in the system, respectively, containing thin film, and μ_i is the chemical potential of i-th component of the system.

Surface forces of both kinds are responsible for the particular features of the three-phase equilibrium, for the nature of wetting established in one or another system, and, finally, for the coexistence of bulk and confined liquids. Certainly, surface forces of both kinds originate from the intermolecular forces. Therefore the feeling may appear that the description of different aspects of manifestation of these forces on the basis of various kinds of surfaces forces, as well as the introduction of various concepts, like surface (interfacial) tension, line tension, and disjoining pressure, is mainly a question of terminology. In particular, there exists a point of view that both the line tension and the disjoining pressure describe one and the same peculiarities of the three-phase contact [65]. However, all the above-mentioned concepts are related to different aspects of manifestation of the intermolecular forces, and each of them is responsible for different phenomena. For example, neither the line tension nor

the disjoining pressure affects the shape of the pendant drop; this shape is completely determined by the surface tension and the gravitational forces. On the contrary, the equilibrium thickness of the wetting film on a flat substrate is determined by the disjoining pressure; neither the surface tension nor the line tension affects this thickness. Another example is the drop on fiber in equilibrium with the wetting film, which is covering the fiber. The Young equation and the main problems in its application.

Among numerous approaches relating the equilibrium wettability of solid by liquid with the properties of interfaces through their thermodynamic parameters one of the most popular is based on the application of the Young equation:

$$cos\theta_0 = \frac{\sigma_{sv} - \sigma_{sl}}{\sigma_{lv}}$$
(1-70)

Where θ_0 is the contact angle, σ_{sv} and σ_{sl} are the surface energies at the solid/vapor and solid/liquid interfaces, respectively, and σ_{lv} is the surface tension of the liquid. The application of this equation typically implies the assumption that solid is smooth, homogeneous, non-deformable, and insoluble in the probe non-reactive liquid. The Young's contact angle defined by Equation 1-68 is affected by physicochemical and geometrical peculiarities of contacting phases through the surface energies. It has been noted [64] that Young's equation gives a macroscopic contact angle defined as the angle of intersection of the capillary surface of the liquid (liquid meniscus or drop) and solid substrate, which are not perturbed by the field of surface forces of the second kind. However, these surface forces (acting between the solid/liquid and the liquid/fluid interfaces within the transition zone) modify the shape of liquid and solid surfaces on the nanoscopic scale [64], [66]–[68]

As a result, the macroscopic contact angle differs from the local nanoscopic angles in the vicinity of three-phase contact line. Thus, Young's angle does not concern itself with the slope

of the liquid surface in the close vicinity of the substrate and has to be considered as the macroscopic parameter of three-phase coexistence.

The Young equation is applicable for the description of three-phase equilibrium in systems with various geometries, like liquid meniscus near the wall and inside the capillaries, sessile drops, captive bubbles, etc. However, below for definiteness, we will mainly refer to the geometry of sessile drop (unless specified otherwise) as the system most frequently used for contact angle measurement.

Besides, the contact angle measurement is based on the analysis of the three-phase contact and the angle is dependent on the three-phase contact formation [69]–[71]. Thus the shape of the sessile drop is established by the advancement of three-phase line just after drop deposition and the contact angle measured shortly after drop deposition corresponds to the advancing rather than equilibrium angle. In contrast, the measurement of the contact angle by the withdrawal of Wilhelmy plate gives the receding angle as formed in the process of the triple line retreat.

Another difficulty in the analysis of experimental findings on the basis of Equation (1-69) is related to the mechanical deformation of real solid surface. Such deformation is caused by the excess pressure inside the drop and the transition zone between the drop and the wetting/ adsorption film. In its turn, this deformation modifies the energy balance. [66], [67], [72]

The consistent interpretation of contact angles θ for nano- and submicron drops needs the completion of the Young equation by terms associated with the line tension contribution:

$$cos\theta = cos\theta_0 - \frac{1}{\sigma_{LV}}[\frac{\tau}{r} + \frac{\partial\tau}{\partial r}]cos\gamma \qquad\qquad (1\text{-}71)$$

where θ_0 is the contact angle for the system under consideration created by the drop of infinite contact radius, τ is the line tension, describing the additional free energy required to create the unit length of three-phase contact line, r is the contact line radius, and γ is the angle

46

between the principal normal to contact line and the tangent plane to the substrate surface. The concept of line tension was proposed by Gibbs [73] to account for three-phase mutual interactions in the immediate vicinity of the contact line. Since the role of line tension is not of central importance for the problems discussed in this research, we will not dwell on the consideration of this phenomenon here. The detailed collection of references on papers devoted to various theoretical approaches as well as a summary of experimental studies of the line tension phenomena can be found in the review paper of Amirfazli and Neumann [74].

However, it is worth noting here that despite of the variety of theoretical approaches used to deduce the sign and the magnitude of the line tension, it is well appreciated now that the nature of the latter is related to the overlapping of the fields of surface forces associated with each of the phases mingling at the three-phase contact [66]–[68], [75]–[79].

As it can be deducted from Eq. (1-69), the influence of line tension correction is determined both by the contact line parameters, such as the radius, the magnitude and the sign of the line tension and by the mutual orientation of contact line and substrate surface. Thus, for the cases when $\partial\tau/\partial r$ can be neglected and the wetted surface is flat, Eq. (1-69) reduces to the well-known generalized Young equation [64], [67], [74], [78], [80]. According to Eq. (1-69) the line tension does not influence the wettability of external and internal cylindrical surfaces such as pores and fibers, whereas its role in the wettability of spherical particles is determined by the three-phase line position and vanishes for the equatorial section. The physical mechanism, underlying such behavior is related to the total (for cylindrical surfaces) or partial compensation of forces associated with the line tension, by the elastic reaction of the substrate.

The application of the conventional Young equation for the interpretation of experimental data on contact angle measurements using macroscopic drops (when all terms related to the line tension can be omitted) requires the information about solid/vapor and solid/ liquid

surface energies. Our knowledge about the above parameters typically is quite poor, because the estimation of surface energies of the solid/fluid interface is based on the indirect experimental methods coupled with a model representation of the system. As a result, the values obtained in the frame of different approaches may significantly differ from each other. Generally, σ_{sv} differs from the surface energy at solid/vacuum interface because the solid surface is covered with a thin wetting or adsorption film of liquid that is in equilibrium with the drop and the vapor.

1.15 Thesis Overview

There are many studies concentrated on fibrous filters, membrane filters, and fabric filters; but a few of them have focused on granular air filtration. Limited information has shown that granular air filtration has high removal efficiency for a wide range of particle size [81]–[85]. Granular filters may also be the only and promising option for air filtration at high temperature and high pressure [86]–[91].

The mechanisms of granular air filtration are similar to those of fibrous air filtration, except that the particles are deposited on surfaces of the granules. Among all the particle transport mechanisms, it has been widely accepted that diffusion is the dominant mechanism for the removal of nanoparticles (1 nm–100 nm in diameter), the electrostatic and electromagnetic effect is often ignored in conventional air filtration models that were developed based on single fiber theory [5], [92]. Aerosol particles and granules often carry electrostatic charges which may influence particle transport and the consequent removal efficiency. The electrostatic forces between particles and granules may include image forces, dielectrophoretic due to collector charge, magnohporetic due to a coil, columbic force, space charge effect, columbic force due to the external field, dielectrophoretic and magnophporetic

due to the external electric field. However, the columbic forces due to particle charge and an external electrostatic and electromagnetic field are the most dominant forces [16].

Because of few research on the effect of electrostatic and electromagnetic forces on the filtering of soot-filtered filters, in this study, the effect of electromagnetic and electrostatic forces on the efficiency of soaked grain filters is scrutinized by using Comsol software.

1.16 Literature Review

The mechanisms of granular air filtration are similar to those of fibrous air filtration, except that the particles are deposited on surfaces of the granules. Among all the particle transport mechanisms, it has been widely accepted that diffusion is the dominant mechanism for the removal of nanoparticles (1–100 nm in diameter), and the electrostatic effect is often ignored in conventional air filtration models that were developed based on single fiber theory.

The effect of electrostatic forces on the granular filtration of nanoaerosol NaCl particles in the range of 10 nm to 100nm was investigated experimentally in Golashahi and et al. [81]. The test granular filters were made of 2mm homogeneous glass beads at three media thicknesses (25, 76 and 127mm), and they were tested at three airflow rates (27, 45, and 65 lpm). The filtration efficiencies were measured for neutralized and charged NaCl nanoparticles. The corresponding difference was considered as the filtration efficiency attributed to the electrostatic attraction between the charged NaCl particles and the glass granules. Results showed that the electrostatics played a great role in nanoaerosol filtration, which is different from conventional filtration theories. Its contribution to filtration efficiency increased with the size of the nanoparticles to a level of 30% or so. Results also showed a positive correlation between the separation efficiency due to electrostatic forces and the residence time of the

49

airflow. The correlation is relatively strong (between 0.6 and 0.9) for particles in the range of 20–100 nm. However, it is weak, although positive, for sub-20 nm particles [93].

Wet scrubbers are one of the type of granular filters which are widely used to clean exhaust gas in the fields of metallurgy, mining and electric power plants [94]. These carrier particles are removed from a gas stream by conventional wet scrubbers through three main scrubbing mechanisms, i.e., Brownian diffusion, interception and inertial impaction [95], [96].

Lei Guan, et al. [97] built a randomly packed granular filtration model to investigate the mechanism of particle deposition on the granular surface, including the deposition positions, the backflow of articles and the relation with Stokes number. The deposition positions of particles of different sizes on the granular surface were exhibited, and the results showed that the diameters of particles deposited on the leeward side of the granule are smaller than 5μm. The deposition area is larger and more uniform for smaller particle deposited on the windward side of the granule and it leads to a higher-pressure drop. Besides, the concentrations of particles smaller than 5μm linearly decrease with the height of the model between 50mm~78mm, and for the cases of larger than 15μm, they dramatically drop between 50mm~63mm and the decline rate gradually reduces to zero with respect to 78mm. Other cases of particle diameters between 5μm ~15μm are between the above two situations. The Stokes number based on the inlet gas velocity versus the grade collection efficiency and the Stokes number based on the normal impaction velocity of particles versus the diameter of the particles are concluded to evaluate the filtration performance and the sticking probability of particles and they are expressed with two equations. [97] Conventional gravitational wet scrubbers, which generally perform removal of fine particles with low efficiency, cannot meet new standards for pollution emissions. One way of improving the collection efficiency of fine particles is to impose additional electrostatic forces upon particles by means of particle-

charging, or droplet-charging, or even opposite-charging of particles and droplets. A Monte Carlo method for population balance modeling is presented to describe the particle removal processes of gravitational wet scrubbers with electrostatic enhancement, in such a way that the grade collection efficiency and particle size distribution are calculated quantitatively. Numerical results show that the grade collection efficiency of submicron particles is only about 5% in conventional wet scrubbers. However, it reaches approximately 25% in particle-charging wet scrubbers, roughly 70% in droplet-charging wet scrubbers, and even above 99% in opposite-charging wet scrubbers. Furthermore, population balance modeling is used to optimize the operational parameters of the droplet-charging wet scrubbers by means of the quantitative comparison of the grade collection efficiency. It is found that the operational parameters that are beneficial to the high-efficiency removal of fine particles are faster gas velocity, slower droplet velocity, larger liquid-to-gas flow ratio, larger charge-to-mass ratio of droplets, smaller geometric mean diameter and smaller geometric standard deviation of droplets.[98]

Although a number of studies have been conducted by considering the external electric field to enhance electrostatic forces between microsized particles and granular beads, there is very limited information about the effect of electrostatic and electromagnetic forces on wet granular filtration of particles. In this work, a numerical study was carried out to investigate the effect of electrostatic and electromagnetic forces on aerosol filtration.

51

Chapter 2

Governing Equations and Numerical Scheme

2.1 Two- Phase Flow

The Two-Phase Flow, Level Set, and Phase Field interfaces can be used to model the flow of two different, immiscible fluids, where the exact position of the interface between the two fluids is of interest. The fluid-fluid interface is tracked using an auxiliary function on a fixed mesh. These methods account for differences in the two fluids' densities and viscosities and include the effects of surface tension and gravity.

2.1.1 The Two-Phase Flow, Level Set, and Phase Field Interfaces

The following sections list all the physics interfaces and the physics features associated with them under the Multiphase Flow branch. The descriptions follow a structured order as defined by the order in the branch. Because many of the physics interfaces are integrated with each other, some described nodes will also be cross-referenced to other physics interfaces.

2.1.1.1 Level Set and Phase Field Equations

By default, the Level Set and Phase Field interfaces use the incompressible formulation of the Navier-Stokes equations:

$$\nabla . u = 0 \qquad\qquad (\text{2-1})$$

$$\rho \frac{\partial u}{\partial t} + \rho (u . \nabla) u = \nabla . [-pI + \mu(\nabla u + \nabla u^T)] + F_g + F_{st} + F_{ext} + F \qquad (\text{2-2})$$

Note that Equation 2-1 and Equation 2-2 are solved in the contained interface, Laminar Flow or Turbulent Flow interface.

2.1.1.2 Using the Level Set Method

If the level set method is used to track the interface, it adds the following equation:

$$\frac{\partial \Phi}{\partial t} + u.\nabla\Phi = \gamma\nabla.\left(\varepsilon\nabla\Phi - \Phi(1-\Phi)\right)\frac{\nabla\Phi}{|\nabla\Phi|} \qquad (2\text{-}3)$$

where γ is the reinitialization parameter, and ε is the interface thickness controlling parameter (is equal to $h_{max}/2$ where h_{max} is the maximum element size in the component). The density is a function of the:

$$\rho = \rho_1 + (\rho_2 - \rho_1)\Phi \qquad (2\text{-}4)$$

And the dynamic viscosity is given by

$$\mu = \mu_1 + (\mu_2 - \mu_1)\Phi \qquad (2\text{-}5)$$

where ρ_1 and ρ_2 are the constant densities of Fluid 1 and Fluid 2, respectively, and μ_1 and μ_2 are the dynamic viscosities of Fluid 1 and Fluid 2, respectively. Here, Fluid 1 corresponds to the domain where $\phi < 0.5$, and Fluid 2 corresponds to the domain where $\phi > 0.5$.

2.1.1.3 The Surface Tension Force for the Level Set Method

For the level set method, the surface tension force acting on the interface between the two fluids is $F_{st} = \sigma\kappa\delta n$ where σ is the surface tensions coefficient (SI unit: N/m), κ is the curvature, and n is the unit normal to the interface. δ (SI unit: 1/m) is a Dirac delta function located at the interface and κ depends on the second derivatives of the level set function ϕ. This can lead to poor accuracy of the surface tension force. Therefore, the following alternative formulation is used:

$$F_{st} = \nabla \cdot \left(\sigma \left(I - (nn^T) \right) \delta \right) \tag{2-6}$$

In the weak formulation of the momentum equation, it is possible to move the divergence operator, using integration by parts, to the test functions for the velocity components.

The δ-function is approximated by a smooth function according to

$$\delta = 6|\nabla \Phi||\Phi - (1 - \Phi)| \tag{2-7}$$

2.1.1.4 Conservative and Non-Conservative Formulations

When the velocity field is divergence free, one can use either the conservative or the nonconservative formulation of the level set or phase field equation. The conservative form perfectly conserves the mass of each fluid, but the computational time is generally longer.

2.1.1.5 Phase Initialization

If the study type Transient with Phase Initialization is used in the model, the level set or phase field variable is automatically initialized. For this study, two study steps are created, Phase Initialization and Time Dependent. The Phase Initialization step solves the distance to the initial interface >, D_{w^i}. The Time-Dependent step then uses the initial condition for the level set function according to the following expression:

$$\Phi_0 = \frac{1}{1 + e^{D_{wi}/\varepsilon}} \tag{2-8}$$

in domains initially filled with Fluid 1 and

$$\Phi_0 = \frac{1}{1 + e^{-D_{wi}/\varepsilon}} \tag{2-9}$$

in domains initially filled with Fluid 2.

Correspondingly, for the phase field method the following expressions are used:

54

$$\Phi_0 = -\tanh\left(\frac{D_{wi}}{\sqrt{2}\varepsilon}\right)$$ (2-10)

in Fluid 1 and

$$\Phi_0 = \tanh\left(\frac{D_{wi}}{\sqrt{2}\varepsilon}\right)$$ (2-11)

in Fluid 2. The initial condition for the help variable is $\psi_0 = 0$. These expressions are based

on the analytical solution of the steady state solution of Equation $\Phi_0 = \frac{1}{1+e^{-D_{wi}/\varepsilon}}$ (2-9)

, Equation $\Phi_0 = -\tanh\left(\frac{D_{wi}}{\sqrt{2}\varepsilon}\right)$ (2-10), and Equation $\Phi_0 = \tanh\left(\frac{D_{wi}}{\sqrt{2}\varepsilon}\right)$ (2-11) for a

straight, non-moving interface.

2.2 Particle Tracking Methodology

Briefly, Lagrangian particle tracking technique calculates the trajectory of every single particle and registers the initial and final locations of particles. Most traditional multiphase flow studies evaluate the particles as a continuum. Hence, the computing cost could be enormous if particles are considered separately. Howbeit, for a typical fiber on a multi-fibrous filter, it is common that the fiber size is comparable to the particle size. In this case, it is not reasonable to study the particles as a continuum, rather than to treat the particles separately. In this section, the main particle capture mechanism as the first step is reviewed, and then the mathematical description of the particle tracking methodology will be provided. This particle tracking methodology is used for the analysis in chapter 4 as the main analyzing tool in this thesis.

2.2.1 Particle Capture Mechanism

Experimental measurements with fibrous filters have validated the fundamental theories about aerosol particle filtration. There are several mechanisms by which a filter can capture a

particle from a moving aerosol stream. Albeit, in this work, we use the capture mechanisms which are particle capture by mechanical means and dielectrophoretic and magnophoretic. Filtration by mechanical means includes direct interception, inertial impaction, and Brownian diffusion. For large particles, gravitational settling is another main mechanical mechanism of particle capture. In this section, an abridged introduction of main capture mechanisms is covered and each main capture mechanism is physically elucidated.

2.2.1.1 Direct Interception

Direct interception turns up when a particle is subject to neither inertial nor diffusive motion, and the particle is not responding to any external force. In this situation, a particle would follow a streamline which comes in contact with the filter surface. Figure 2.1 shows the demonstration of direct interception for a particle captured by a cylindrical fiber.
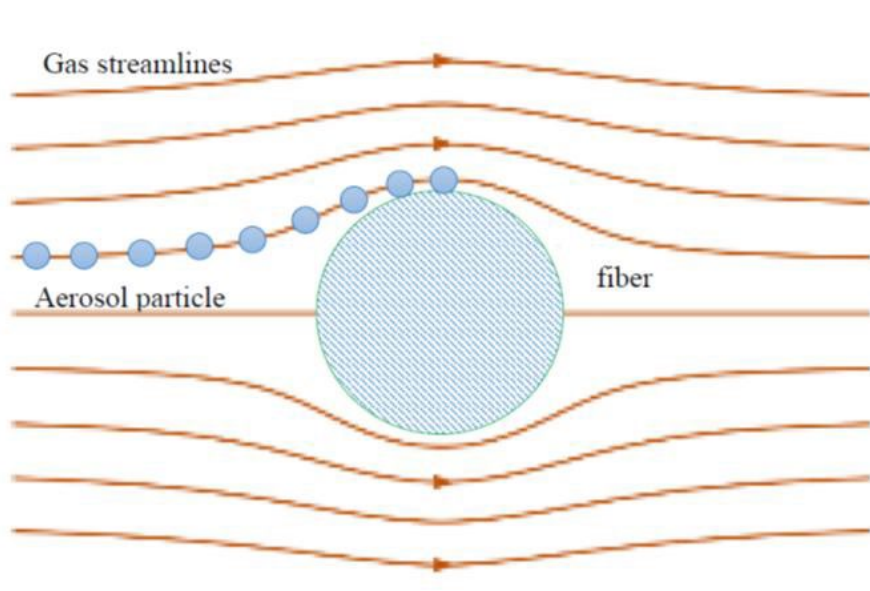

Figure 2.1 Illustration of direct interaction [11].

Direct interception is the capture mechanism simply because of the finite size of the particle itself. The particle is supposed to follow the streamline perfectly. Direct interception is the only mechanical capture mechanism that is not a consequence of the particle deviating from its original streamline, and the capture of the particle due to interception can be described entirely with the flow field. An interception parameter [11], which is defined in equation 3-12, is normally considered to be the dependent variable to quantitatively describe the filtration owing to interception.

$$N_R = \frac{d_p}{d_c}$$
(2-12)

Where d_p is the diameter of the particle, and d_c is the characteristic length of the filter. For fibrous filter, this characteristic length is the diameter of a single fiber. It is self-evident that bigger interception parameter associates with higher filtration efficiency.

2.2.2 Inertia Impaction

Through inertia, an aerosol particle may not be able to follow the streamline under the condition when the flow's direction is varying, such as diverging and converging. When the viscous effect from the fluid is not strong enough to keep the particle's motion along the streamline, a particle deviates from the streamline and can perhaps impact with the filter. This mechanism is called the inertial impaction. How a particle reacts to a change in flow direction appertains upon the inertia of the particle and the drag force from the fluid. A massless particle with no inertia will follow the streamline, while a heavy particle tends to move with its original velocity. Figure 2.2 illustrates the situation when a particle is collected by a cylindrical fiber due to inertial impaction. As illustrated in Figure 2.2, instead of following the streamline, the particle moves with the dotted line and contacts with the fiber due to a piecemeal deviation from the streamline.
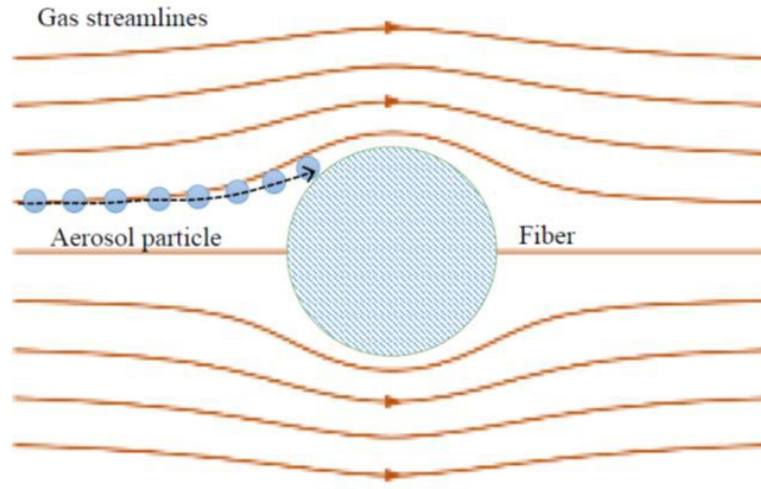
Figure 2.2 Illustration of inertial impaction [11].

Relaxation time is a prevalent parameter that is used to characterize particles inertia, and stopping distance is the distance that a particle travels before sharing the same velocity of the fluid. Relaxation time and stopping distance are defined as [11]:

$$\tau_R = m_p B \tag{2-13}$$

$$d_{stop} = \tau_R U_0 \tag{2-14}$$

Where τ_R is the relaxation time, m_p is the mass of the particle, d_{stop} is the stopping distance, U_0 is filtration velocity, which is normally the mean velocity of the injecting flow, and B is the mechanical mobility of the particle which is defined in equation 3-4 for an aerosol particle.

$$B = \frac{C_c}{3\pi\mu d_p} \tag{2-15}$$

where C_c is Cunningham correction factor, and μ is kinematic viscosity of the fluid. Relaxation time is correlated to the particle's inertia; a short relaxation time implies low particle inertia and a long relaxation time implies high particle inertia. In studies of particle

58

filtration owing to inertial effects with fibrous filters, it is universally understood that the Stokes number is the dimensionless parameter that characterizes inertial impaction. The Stokes number is defined as the ratio of particle stopping distance to the characteristic length of the filter, as depicted in equation 3-15[11].

$$St = \frac{\tau P U_0}{d_c} = \frac{\rho_p d_p^2 C_c U_0}{18 \mu d_c} \qquad \qquad (2\text{-}16)$$

where St is the Stokes number and ρ_p is the density of the particle. The Stokes number portrays particle deposition due to inertial effects. A smaller Stokes number intimates smaller inertial effects while a larger Stokes number intimates stronger inertial effects. When the Stokes number is close to zero, a particle follows the streamlines. As the Stokes number increments, a particle commences to diverge from streamlines. Whether or not, stronger inertial effects lead to higher filtration efficiency depends on the geometry of the filter.

2.2.2.1 Brownian Diffusion

When a fine particle is suspended in a fluid, the impact from the surrounding gas or liquid molecules incurs the instantaneous momentum of the particle to vary randomly and accordingly causes the particle to move in a fortuitous path. This accidental motion of fine particles in a medium is called Brownian motion. Figure 2.3 indicates the Brownian motion process of a single particle. In this figure, the dotted lines are a possible path of the moving particle (blue sphere). Yellow scattered spheres are free molecules of the medium.
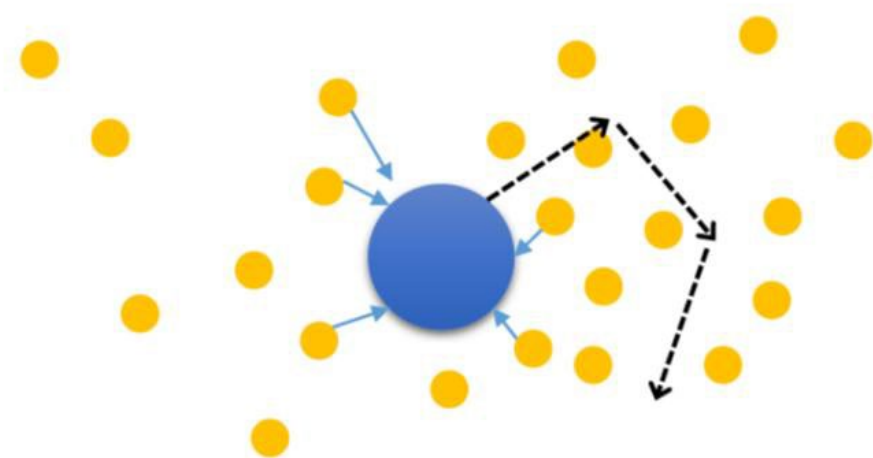
Figure 2.3 Illustration of a particle's motion due to Brownian motion [11].

Brownian motion is known to be significantly lucrative for submicron particle filtration. When a particle flows with a fluid, Brownian diffusion will be the reason for the particle to randomly deviate from the streamline, and impact with a solid surface. Figure 2.4 represents a possible case when a particle contacts the surface of a cylindrical fibrous filter because of Brownian diffusion.
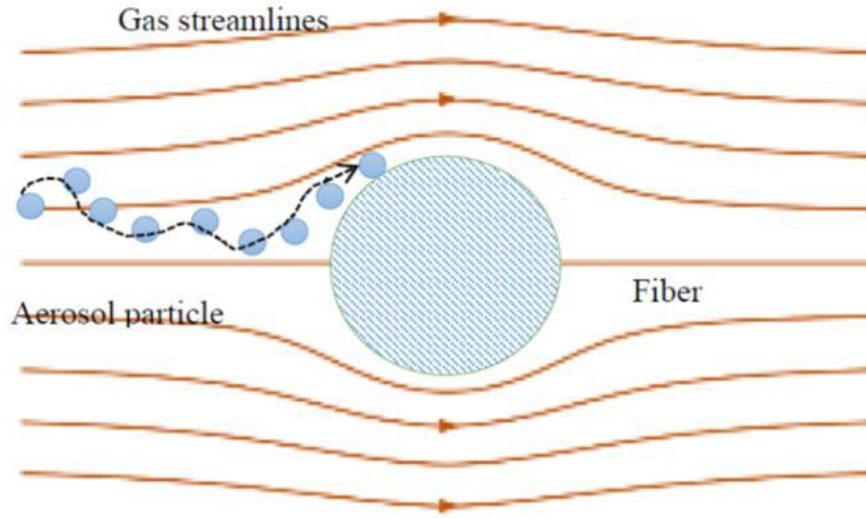
Figure 2.4 Illustration of particle capture due to Brownian diffusion [11].

Particle capture owing to Brownian motion diffusion depends on both the diffusion properties of the particle and the flow condition. In the theories about filtration with fibrous filters, it is commonly considered that Brownian diffusion is governed by the particle's Peclet number, which is defined as:

$$Pe = \frac{d_C U_0}{D} \qquad (2\text{-}17)$$

Where Pe is the Peclet number, and D is the coefficient of diffusion of particles

$$D = \frac{\kappa_B T C_c}{3\pi\mu d_p} \qquad (2\text{-}18)$$

where $k_B = 1.38 \times 10^{-23} \, J/K$ is the Boltzmann constant, and T is the absolute temperature. From equation 2-18, it is perceptible that capture due to Brownian motion is dependent on the geometry of the filter (fiber diameter d_f), flow condition (free filtration velocity U_0) and the diffusion properties of the particle itself (coefficient of diffusion D). For a small particle, the effect of momentum transfer between the particle and free molecules is relatively stronger in

comparison with bigger particles. This means smaller particles are more diffusive compared to bigger particles. Thus, for submicron aerosol particles, Brownian motion is the main capture mechanism. When the Peclet number is close to zero, it means the particle is very diffusive (with a large D), or the filter is very small (with a small d_f), or the flow is very weak (with a small U0). In the above situations, it is clear that particle capture will be easier, resulting in higher filtration efficiency. With the augmentation of the Peclet number, the filtration gets smaller due to Brownian motion.

2.2.2.2 Other Mechanisms

While the main mechanisms are dominant for submicron particles filtration, there are a few other mechanisms that might be momentous under some circumstances. These other mechanisms contain gravitational settling, the Saffman lift force, the thermophoretic force, the pressure gradient, and the particle-to-particle interaction.

Gravitational settling portrays the particle motion due to the gravity. If the particle density is distinct from that of the fluid, then the particles will settle in the direction of the gravitational force.

Besides, when a small particle is suspended in a gas that has a temperature gradient, the particle experiences a force in the direction opposite to the direction of the temperature gradient. This phenomenon is called thermophoresis. This force is dependent on both the gas and particle properties, as well as the temperature distribution. Since, the direction of thermophoretic force is always in the direction of decreasing temperature, if the average fluid temperature is higher than the surrounding channel surface, the thermophoretic force helps to drive the particle towards the surface. The Saffman lift force is usually deliberated to be

significant when a particle is fairly close to the surface. In this thesis, it is assumed that neither the flow nor the filter is heated, and both the flow and the filter are under room temperature, thus thermophoretic forces are neglected.

2.2.3 Lagrangian Particle Tracking Technique

As discussed in 3.1.1, there are many various physical mechanisms that influence the filtration process under different conditions. Howbeit, it is not necessary to include all the mechanisms to study sub-micron particle filtration with multi-fibrous filters because under most conditions, only three mechanisms are prevailing while the others can be small enough to be neglected. Hereupon, to construct a mathematical model of particle motion and calculate the trajectories of particles, it is necessary to make a few assumptions that simplify the model and computation process. In this thesis, Brownian motion, Saffman's lift force, Drag force, Gravity force, Dielectrophoretic force and magnetophoretic force are included as the main particle capture mechanisms.

Particles are assumed to be spherical and particle rotation is neglected. As well, it is assumed that interactions between particles are neglected as one particle's effect on another is much smaller than the interaction between the particle and the filter itself. Furthermore, in an actual filtration process, it is possible for a particle to deposit on another particle, however, particle coagulation is not considered in this thesis. Another reason to assume that particle is injected separately is that the calculation of flow field is needed in advance in order to calculate a particle's trajectory. By assuming that there is no deposited particle inside the channel, the study avoided the complexity of an altering flow field through the filtration process. In addition, a one-way coupling of the filtration process assumes that the particle's motion does not affect the flow field.

63

2.2.3.1 Equation of Particle Motion (EOM)

The governing equation for a spherical particle in an aerosol stream is Newton's second law, which describes the correlation between a single object's acceleration and the external forces applied on the object. With the consideration of two main deposition mechanisms and one other force, hydrodynamic drag force from a surrounding fluid; an external Brownian force to model Brownian motion of particles; and Saffman's lift force which should be considered for submicron particles, were included into Newton's second law of particle motion. The trajectory of the particle is governed by the following equation:

$$\frac{d}{dt}(m_p v) = F_D + F_g + F_{ext} \qquad\qquad (2\text{-}19)$$

Where m_p is the mass of the particle, v represents the velocity of the particle, F_D and F_g express the hydrodynamic drag force and gravity force, respectively. F_{ext} represents the summation of Saffman's lift F_L force, Brownian motion force (F_B) and dielectrophoretic force (F_{dp}) and magnetophoretic force (F_{mp}). Gravitational force is proved much smaller than the Brownian force and is thus neglected.

$$m_p \frac{dv}{dt} = F_D + F_g + F_{ext} \qquad\qquad (2\text{-}20)$$

The assumption is that any mass lost by the particles continues to move with the particle velocity and does not cause the particle to decelerate.

2.2.3.2 Drag Force

The drag force on a particle is owing to the relative motion to the fluid. In equation (2-20) F_D is defined by:

$$F_D = \left(\frac{1}{\tau_p S}\right) m_p (u - v) \qquad\qquad\qquad\qquad (2\text{-}21)$$

Where m_p is the particle mass, τ_p is the particle velocity response time, $\boldsymbol{v}$ is the velocity of the particle and $\boldsymbol{u}$ is the response to the fluid.

A large number of expressions for the particle response time are available. Selecting an appropriate drag law requires knowledge of the relative Reynolds number Re (dimensionless) of particles in the flow. The relative Reynolds number is given by the expression:

$$Re_r = \frac{\rho \|u - v\| d_p}{\mu} \qquad\qquad\qquad\qquad (2\text{-}22)$$

For a spherical particle experiencing flow with small Reynolds number, the calculation of drag force follows Stokes law, through which the drag force on a spherical particle due to the fluid's viscosity will be calculated [78]:

$$\tau_p = \frac{\rho_p d_p^2}{18\mu} \qquad\qquad\qquad\qquad (2\text{-}23)$$

where ρ_p and d_p are the diameters of particle, respectively and μ is the dynamic viscosity of ambient gas.

For small particles, the Knudsen number becomes large; drag is reduced at the range compared to the Stokes' law prediction, therefore a correction factor is needed.

When rarefaction effects are included, a correction factor is applied to the drag force to account for the effects of a nonzero particle Knudsen number:

$$C_D = \frac{C_{D,c}}{S} \qquad\qquad\qquad\qquad (2\text{-}24)$$

Where C_D (dimensionless) is the drag coefficient, $C_{D,C}$ (dimensionless) is the drag coefficient under conditions of continuum flow (the limit as the particle Knudsen number Kn approaches zero), and S (dimensionless) is the correction factor that accounts for noncontinuum flow.

For the following definitions of the drag force correction factor, the particle Knudsen number is defined as:

$$Kn = \frac{\lambda}{d_p} \tag{2-25}$$

where d_p is the particle diameter and λ is the mean free path of gas molecules:

$$\lambda = \sqrt{\frac{\pi}{2\rho p}}\mu \tag{2-26}$$

where p is the gas pressure, ρ is the gas density, and μ is the gas viscosity.

The Cunningham-Millikan-Davies model uses three dimensionless, user-defined coefficients to define the correction factor:

$$S = 1 + Kn\left(C_1 + C_2\exp\left(-\frac{C_3}{Kn}\right)\right) \tag{2-27}$$

where $C_1, C_2, and\ C_3$ are user-define coefficients. In this thesis, these numbers are used based on Cunningham-Millikan-Davies as $C_1 = 2.514, C_2 = 0.8, C_3 = 0.55$

2.2.3.3 Brownian Force

In order to include the Brownian motion as a main particle capture mechanism, we need to model Brownian motion as an external force. The Brownian Force node is accounted for the diffusion of suspended particles in a fluid according to Einstein's theory. When using this feature, a random force is applied to each particle at each time step. This often forces the

solver to take very small time steps because the relative and absolute tolerances solver settings are quite strict (10^{-5} and 10^{-6}, respectively).

The Brownian motion of a particle is modeled as a Gaussian white noise process [81]. Given the fact that Brownian motion is affected by collisions with free molecules, the Brownian force is dependent on the properties of both the fluid and the particle. The Brownian force is given as [83]:

$$F_B = \varsigma \sqrt{\frac{12\pi a \mu k_B T}{\Delta t}}$$

(2-28)

where k_B is the Boltzmann constant which is equal to $1.38 \times 10^{-23} J/K$, T is the absolute temperature, and Δt is the magnitude of the time step. The parameter ς is a Gaussian random number with zero mean and unit variance. The random direction of the Brownian force was accounted for by evaluating both the x and y components of F_B at each time step using independent values of ζ in the two directions. A different value of ζ is created for each particle, at each time step for each component of the Brownian force. The Brownian force leads to spreading of particles from regions of high particle density to low density.

2.2.3.4 Staffman Lift Force

A small particle in shear flow field experiences a lift force perpendicular to the flow direction as a result of the velocity gradient and inertial effects in the viscous flow around the particle. This force was reported by Saffman and hence called Saffman lift force [79]. For a viscous channel flow, the flow in the axial direction generates a Saffman lift force in the radial direction, which lifts the particles towards the center of the channel and gives a relative importance to prevailing forces.

Particles in a non-uniform velocity field are subjected to lift and drag forces. The drag force acts in the direction opposite the relative velocity of the particle with respect to the fluid. The lift force acts along the direction of the gradient of the fluid velocity. These forces change significantly as the particle approaches a wall.

The Lift Force feature is used to exert a lift force on the particles. Two formulations of the lift force are available. Both expressions for the lift force are valid when the angular velocity of the particle can be neglected and a no-slip boundary condition applies at the particle surface.

The following sections describe the available lift force models. The Saffman lift force is utilized when particles are in a non-uniform velocity field far from walls. The Wall induced lift force applies to particles close to the walls of a flow channel.

The Saffman lift force F_L (SI unit: N), described in [99], is given by

$$F_L = 81.2 r_p^2 L_v \sqrt{\mu \rho \frac{|u-v|}{L_b}} \tag{2-29}$$

$$L_v = (u - v) \times [\nabla \times (u - v)] \tag{2-30}$$

Where r_p is the particle radius, μ is the fluid viscosity and $\boldsymbol{v}$ and $\boldsymbol{u}$ are the velocities of the particle and fluid, respectively.

The Saffman lift force is only nonzero for particles that have not yet been entrained in the surrounding fluid. Once a particle has reached equilibrium with the surrounding fluid velocity, the Saffman lift force is zero. To model the inertial lift force on particles in a flow channel, which is typically nonzero even after the particles become entrained in the flow, we need to consider using the Wall induced lift force described in the following section.

2.2.3.5 Gravity Force

One must use the Gravity Force node to define the gravity vector and density. The gravity force causes particles with a suitably high mass and density to move in the same direction as the orientation of the gravity vector. For submicron particles, the drag and other external forces can dominate and gravity can have little effect on the particle trajectories.

Coordinates are based on space dimension for the Gravity vector g (SI unit: m/s2). The default magnitude for the gravity vector is constantly equal to g = 9.80665 m/s2 corresponding to the standard acceleration due to the gravity on Earth.

The Gravity Force is given by:

$$F_g = m_p g \frac{\rho_p - \rho}{\rho_p} \qquad (2\text{-}31)$$

where ρ is the density of the surrounding fluid (SI unit: kg/m^3) and g is the gravity vector (SI unit: m/s^2).

2.2.3.6 Dielectrophoretic Force

The Dielectrophoretic Force feature adds the following contribution to F_{ext} for the case of a static electric field:

$$F_{dp} = 2\pi r_p^3 \varepsilon_0 \, real(\varepsilon^*) real\left(\frac{\varepsilon_p^* - \varepsilon^*}{\varepsilon_p^* + 2\varepsilon^*}\right) \nabla |E_{rms}|^2 \qquad (2\text{-}32)$$

Where $\boldsymbol{E}_{rms}$ denotes the root mean square electric field. For fields that are computed in the frequency domain, the complex permittivity can be expressed as

$$\varepsilon^* = \varepsilon - \frac{i\sigma}{\omega} \qquad (2\text{-}33)$$

Where ε is the permittivity, σ (SI unit: S/m) is the electrical conductivity, and ω (SI unit: rad/s) is the angular frequency of the electric field.

2.2.3.7 Magnetophoretic Force

The Magnetophoretic Force causes motion of permeable particles toward regions where the magnetic field is stronger. The magnetophoretic force is applicable for particles which are neutral and have a different relative permeability than the background fluid. The magnetophoretic force is defined as:

$$F_m = 2\pi r_p^3 \mu_0 \mu_r K \nabla |\boldsymbol{H}|^2 \qquad\qquad (\text{2-34})$$

where $\boldsymbol{H}$ is the magnetic field, μ_r is the fluid relative permeability, $\mu_{r,p}$ is the particle relative permeability, and K is defined as:

$$K = \frac{\mu_{r,p} - \mu_r}{\mu_{r,p} + 2\mu_r} \qquad\qquad (\text{2-35})$$

The force is only valid for non-conducting particles, so additional force contributions due to eddy currents induced in particles are not taken into account.

2.3   Numerical Scheme

2.3.1   Grid's Quality

The quality of meshing is indispensable for ensuring an accurate analysis of the simulation. A fine mesh will only produce more precise data than a coarse mesh if the mesh elements are of the same or better quality. The quality of the mesh is defined by three important factors: the maximum cell squish, the maximum cell skewness, and the maximum aspect ratio. In our study, the quality of grid has evaluated by Skwenes Quality ranges from 0 to 1, where values

close to 0 correspond to low quality. The average minimum element quality is about 0.9which means good quality of our mesh. 24716 mapped cell is used for making the mesh.

2.3.2   Numerical Method

In the finite element method, the continuous flow domain is divided into the finite number of elements introducing the grid. The process of creating an efficient grid representing the physics correctly is drastically based upon the creation and testing of several different grids. Hence, making a grid is a time-consuming part of the CFD-analysis. The quality of the CFD-analysis, to a great extent, is dependent on the grid quality in the sense that a too coarse grid may give erroneous outcomes. A large number of elements throughout the domain is preferable, but is computationally expensive; accordingly, a compromise between accuracy and number of elements should be taken into account. A comprehension of fundamental fluid dynamics of the problem is necessary, so high-density grids can be used in regions of flow where complex behavior is expected.

2.3.2.1   Finite Element Method

The description of the laws of physics for space- and time-dependent problems is usually expressed in terms of partial differential equations (PDEs). For the vast majority of geometries and problems, these PDEs cannot be solved with analytical methods. Instead, an approximation of the equations can be constructed, typically based upon different types of discretization. These discretization methods approximate the PDEs with numerical model equations, which can be solved using numerical methods. The solutions to the numerical model equations are, in turn, an approximation of the real solution to the PDEs.

One of the benefits of using the finite element method is that it offers great freedom in the selection of discretization, both in the elements that may be used to discretize space and the basis functions. Another benefit of the finite element method is that the theory is well developed. The reason for this is the close relationship between the numerical formulation and the weak formulation of the PDE problem. For instance, the theory provides useful error estimates, or bounds for the error, when the numerical model equations are solved on a computer.

The governing equations of the unsteady flow of an incompressible viscous Newtonian fluid over fiber are the classical continuity and Navier- Stokes equations. They are written in the following form:

$$\nabla. u = 0 \tag{2-36}$$

$$\rho_0 \left(\frac{\partial u}{\partial t} + u. \nabla u \right) - \nabla. \sigma + \rho_0 f = 0 \tag{2-37}$$

In equations 3.1 and 3.2, u denotes the velocity vector, σ is the total stress tensor which is equal to $\sigma = \tau - PI$, τ is the viscous stress tensor and is equal to $\tau = 2\mu D$ in which D is equal to $D = \frac{1}{2}[(\nabla u) + (\nabla u)^T]$, P is the pressure, f is the body force vector (per unit mass), ρ_0 is the density, and μ is the shear viscosity of the fluid. Equation 3-20 has the rate of change term and the convective term in the left-hand side and the diffusion term on the right-hand side. The equation is used as the starting point for the computational procedure in the finite element method.

The level set equation is of linear hyperbolic type. It is well-known that standard conforming finite element discretization methods are in general not very suitable for such partial differential equations since these methods can be unstable. There is extensive literature on finite element techniques for hyperbolic problems. One popular strategy is to combine

standard finite element spaces with a stabilization technique. A fundamental stabilization method, which is very often used in practice, is the streamline-diffusion finite element method (SDFEM).

2.4　Flow Field Validation

2.4.1　A Single Square Fiber without Particle Tracking

To see that the airflow field simulation is correct for different fiber's cross-sectional shapes, a single square fiber is considered in a duct for $Re = 200$. For this Reynolds number, we have laminar vortex shedding flow regime. The ratio of the blockage area is 0.25. The wakes have formed behind the square, and the contour of velocity magnitude is illustrated in figure 2.5:
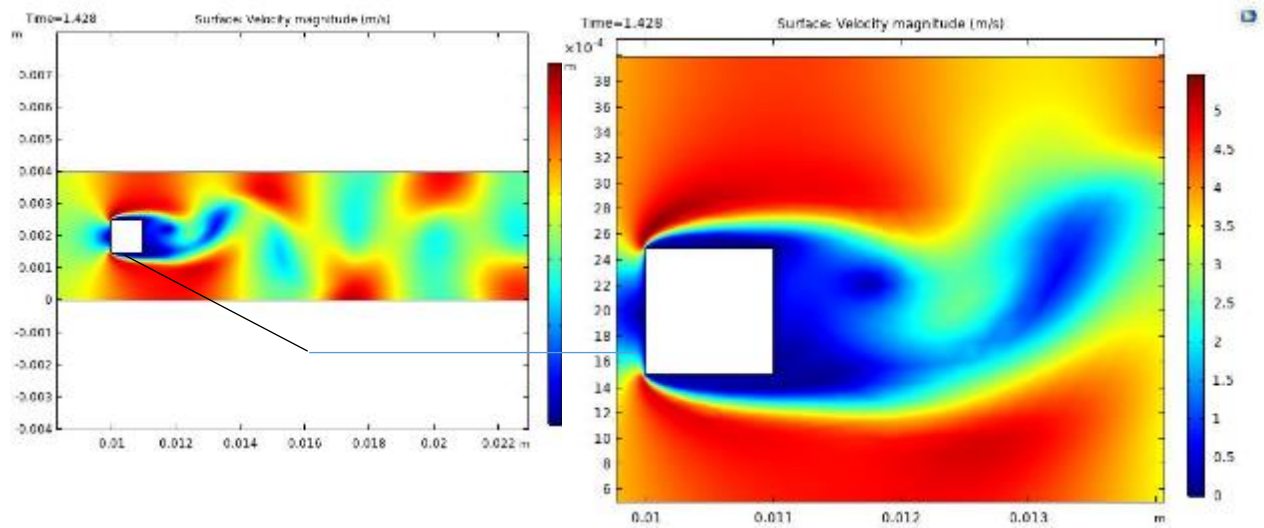
Figure 2.5 Contours of velocity magnitude $Re = 200$
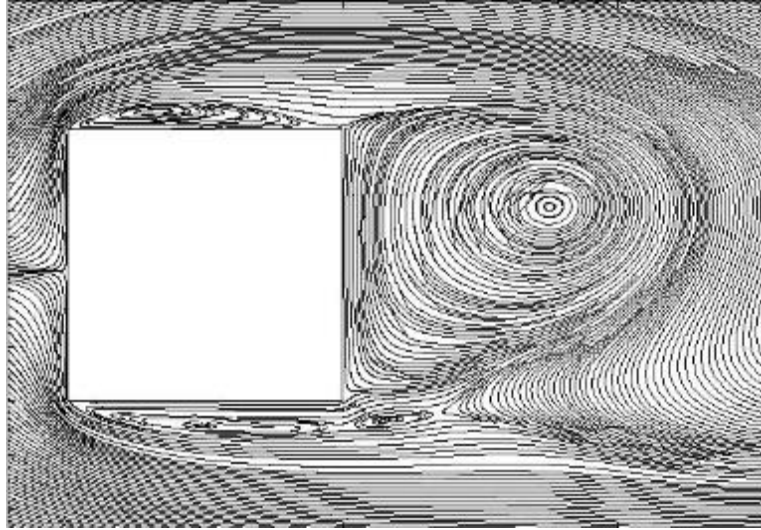
Figure 2.6 Flow streamline for $Re = 200$ at $t = 1.428$

For validating vortex shading, Strouhal number of this study is compared with D. J Bardon (2010), Strouhal number $(St = \frac{fl}{u})$ which is computed in this study and is about 2.21.

Table 2-1 Strouhal numbers for different Reynolds numbers and blockage ratios (D. J Bardon 2010)

Re	$\frac{B}{H}$	Strouhal number (S)
200	0.25	0.2197
250	0.25	0.2197
500	0.25	0.2075
750	0.25	0.2075
1000	0.25	0.1953
1500	0.25	0.1953
2000	0.25	0.1953
250	0.33	0.2686

74

In terms of considering mesh independence, we have changed the number of grid's nodes of the boundary layer at square's wall to obtain a finer mesh which showed the difference below 6% in Strouhal number, in comparison with previous results. For considering the independency of the time step, we have simulated the flow field with half time step, and the error was the same. Again, the time step which is selected for $Re = 200$ is according to the work of R. Franke et al. (1990). The mesh of our present work has depicted below:
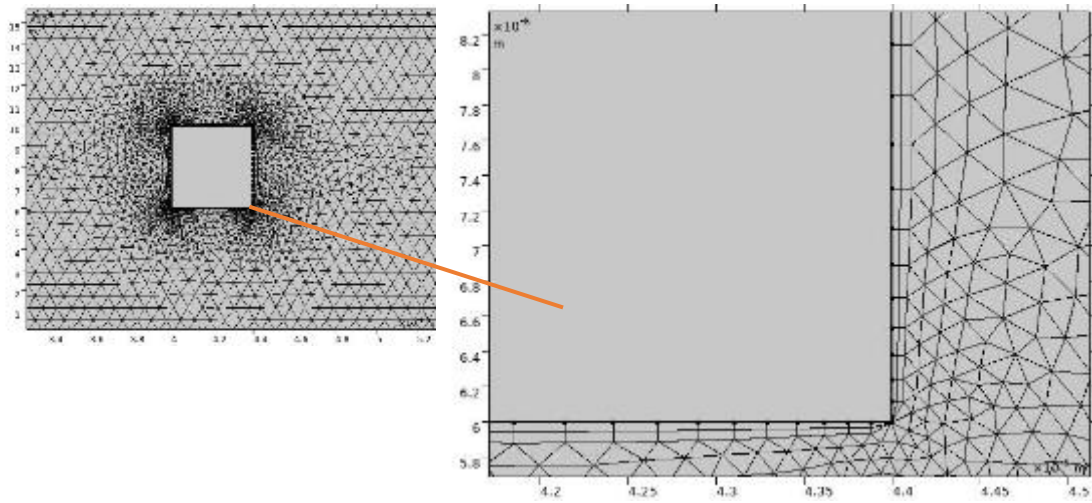
Figure 2.7 Single square fiber's grid

2.5   Simulation Setups with Particle Tracking

The simulation follows the particle tracking methodology described in chapter 3 with a simple geometry of a single rectangular duct. In chapter 3, the drag force on the particles depends upon the local flow field. The Brownian motion is modeled as an external fluctuating force and Saffman's lift force is considered for submicron particles as well.

2.5.1   Flow Field Calculation

A transient laminar incompressible model has been adopted for the flow regime inside our virtual filter. For the $Re = 200$ vortex shedding will happen behind the fibers. Owing to the micron scaled duct size, the flow needs to be reconsidered as microflow. The Knudsen number is the dimensionless number that is used to portray micro flow over fibers. The Knudsen number is defined as:

$$Kn = \frac{\lambda}{d_c} \tag{2-38}$$

Where λ is the mean free path of the fluid, and d_c is the characteristic length, which is usually taken as the fiber's diameter. Under standard conditions, the mean free path of air is about $66\ nm$ [15]. With different Knudsen numbers, the flow can be distinguished into a few different regimes, where the mathematical description is different. Table 2-2 illustrates the range of Knudsen number and the corresponding flow properties [15].

Table 2-2 Knudsen number regimes

$Kn \leq 10^{-2}$	Flow is continuous; Continuum assumption; Navier-Stokes Equation with No-slip boundary conditions
$10^{-2} \leq Kn \leq 10^{-1}$	Navier-Stokes Equation with slip boundary correction
$10^{-1} \leq Kn \leq 10$	Transition flow; High slip on the boundary
$Kn \geq 10$	Free molecular flow

Given a fiber diameter of $1\ \mu m$ and using the channel diameter as characteristic length, one can calculate the Knudsen number as about 0.001, within which the fluid can be treated as a

continuum, and the momentum transport in the fluid can be described by Navier-Stokes equations. Then the No-slip boundary conditions are considered.

Reynolds number of the duct flow over fibers is defined as:

$$Re = \frac{\rho U d_f}{\mu} \hspace{6cm} (2\text{-}39)$$

in which d_f is the fiber diameter.

2.5.2   Solution Algorithm

Lagrangian definition of a problem is possible by solving Newton's law of motion. Newton's law of motion requires determination of particle mass and forces acting on a particle. The magnetic force and electric forces are calculated by the finite element model. For each particle, an ordinary differential equation is solved for each component. Thus, for two-dimensional geometry, two ordinary equations are solved for each particle. Forces acting on each particle are calculated using the magnetic and electric fields in particle's position, at every time step. Then, the particle's position is obtained and the process is repeated until the end of the simulation. The magnetic field, electric field, laminar flow and, the two-phase flow are solved in the first step separately and time-dependently. Particles' motion is time-dependent. Thus, the unsteady particle motion is solved in the next step. The values obtained from the first step are used as the input values for the second step.

The simulation procedure is shown schematically in Figure 2.8. First of all, the magnetic and electric field and the fluid flow are solved separately. Then forces acting on the particle are calculated and from Newton's second law the particle acceleration and velocity are obtained. Then by integrating particle velocity, its position is determined. This calculation is repeated in each time step until the end of the simulation time. All of the above steps are repeated for

each   particle.
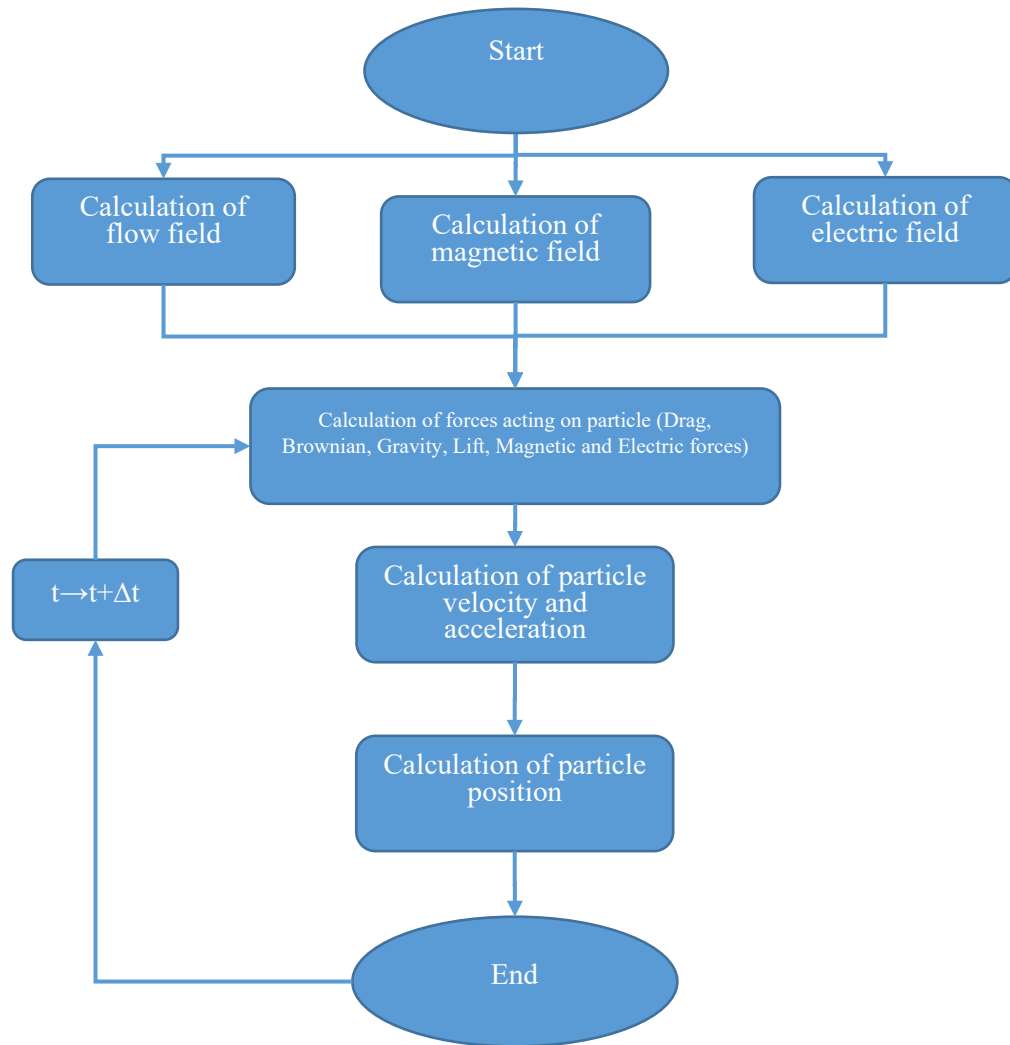

Figure 2.8 A schematic diagram of the solution algorithm.

All computations are performed with a finite element method. The solver has been specifically designed and developed to treat fluid–structure interaction problems. Briefly, the solver possesses the following characteristics.

A mixed finite element method is used to solve the velocity–pressure form of the Navier–Stokes equations for an incompressible fluid. Note that pressure is the Lagrangian multiplier

corresponding to the incompressibility constraint. An implicit Backward Differentiation Formula (BDF) time integrator of second-order accuracy is used for the flow velocity components and phase field component and particle. The parallel sparse direct solver PARDISO [100], [101] is used to solve the linear system. An Implicit method is fully coupling all degrees of freedom.

2.5.3   Boundary Conditions

Boundary conditions considered for the simulations are as follows:

Air is assumed to flow into the simulation domain through a velocity-inlet type boundary. The symmetry boundary condition is used for the top and bottom sides of the computational 2-D geometry. Considering symmetry, boundary conditions should be accepted as no significant lateral airflow is expected inside a filter media. For the airflow on the fiber surfaces, we assumed a no-slip boundary condition. This is because for the air thermal condition and the fiber diameter considered in this thesis, the continuum flow prevails, i.e., $Kn_f = \frac{\lambda}{d_f} \ll 1$, where Kn_f is the fiber Knudsen number, and λ is the mean free path of the air molecules($about\ 66\ nm$).

When water is located around the square cylinder, the wall of cylinder is assumed as a wetted wall and the contact angle between wall and water is assumed $\frac{\pi}{6}$. [102]

2.5.4   Particle Tracking Validation

The current study uses FEM for the simulation of the flow field in a 2D channel with obstruction of a single square fiber. The upstream and downstream distances of the square cylinder are, respectively, 10B and 20B (where B is the width of the cylinder). The blockage

ratio is fixed at 0.25. For the present simulations, an inlet parabolic velocity profile for flow entering to the channel was considered. A zero gradient condition in x-direction was used as the outlet boundary condition, along with the symmetry boundary condition for the upper and lower walls of the channel. The boundary condition used for pressure was zero-normal derivative for the pressure at all boundaries. At the obstacle surfaces, no-slip boundary condition was taken into account. A two-dimensional, incompressible flow of a fluid is considered in the computational domain. The primary parameters affecting the fluid flow in a channel with a square cylinder obstruction are the Reynolds number and the blockage ratio. Reynolds number was based on mean inlet velocity, U_m , and cylinder width, B, was chosen as 200, while a constant value of 25% for blockage ratio was used. Stokes number, non-dimensional particle relaxation time ($stk = \tau U_m/B$) is the key parameter characterizing the particle motion. Unsteady two-dimensional vortex shedding observed in the flow configuration for the dimensions of the computational domain is indicated in Figure 2.9.
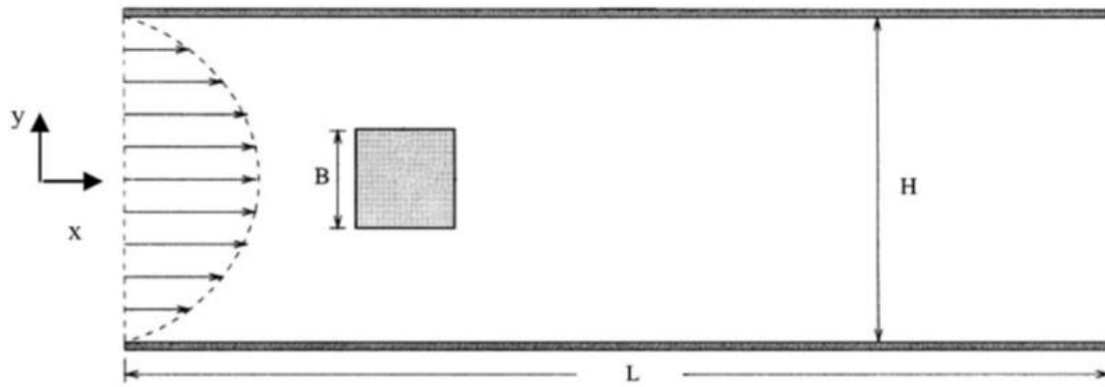
Figure 2.9 Schematic of the computational domain [99].

To validate the present computations with Jafari et al. (2010) and Banihashemi et al. (2016)[99], [103], the deposition efficiencies on the front side of the block were computed. 501 particles for a given Stokes number were injected uniformly in the projected area of the

block at a distance of 10B upstream of the block, and their deposition efficiencies were evaluated.

The particle deposition efficiency is defined as:

$$\eta = \frac{number\ of\ deposited\ particles\ on\ the\ surface}{number\ of\ particles\ entering\ the\ projected\ area\ of\ the\ surface} \qquad (\ 2\text{-}40\ )$$

Figure 2.10 depicts the variation of particle deposition efficiency with the particle Stokes number for the front side of the block, Jafari et al. (2010).
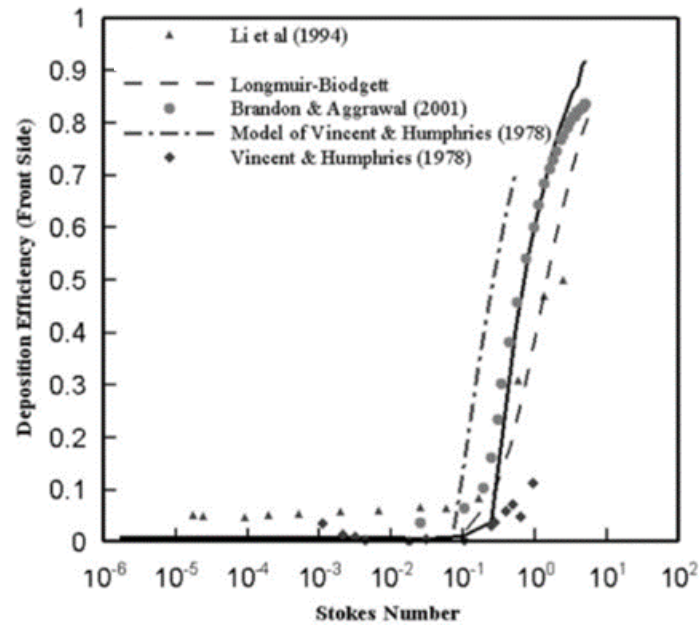

Figure 2.10 Variation of particle deposition with Stk [99].

Figure 2.11 shows our deposition efficiency results, the average errors in comparison with Jafari et al. (2010) is below 5%. $Stk = 0.35$. However, the error is about 9% with Jafari et al. (2010) and 6% with Banihashemi et al. (2016). The calculated deposition efficiency in $Stk = 0.35$ number is located between Jafari et al. (2010) and Banihashemi et al. (2016) which is acceptable for the numerical simulation.
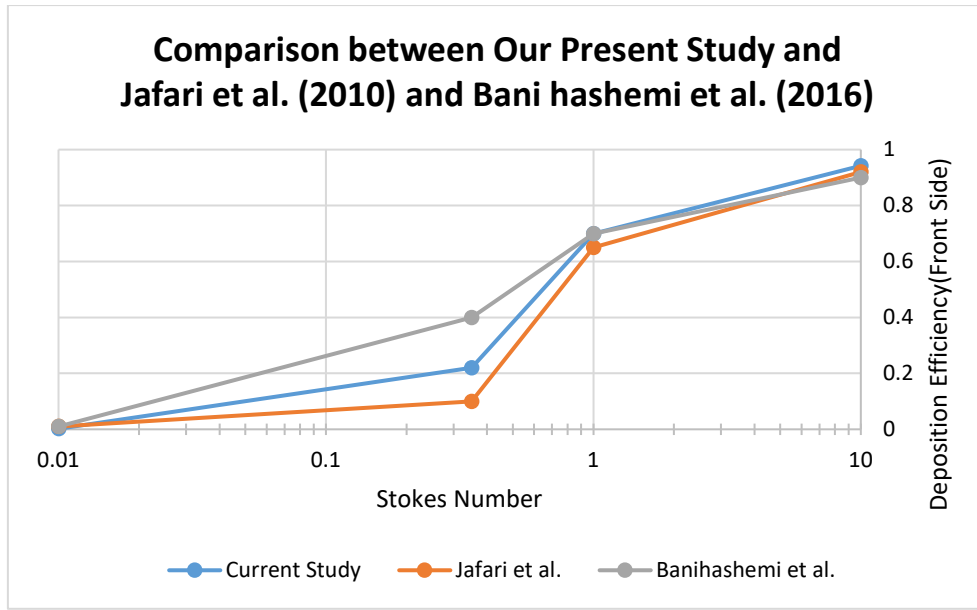
Figure 2.11 Variation of particle deposition efficiency with respect to Stk.

Through the help of boundary adaption in Comsol, our grid independency result shows the error of 0.4%. To study time step independency, we simulated the study with a half-time step ($\frac{\Delta t}{2} = 0.006$) that showed a good agreement in particle capture efficiency according to our previous result. The time step has selected with respect to Re and St, according to the work of R. Franke et al. [104].

2.6   Geometry of the Study

A 2-D domain is investigated in this study. A rectangle channel is selected in which a square block is located at the center in the y-direction. The blockage ratio is 0.25. The upstream and downstream distances of the square cylinder are, respectively, 10B and 5B (where B is the width of the cylinder). For the present simulations, an inlet with a fully developed velocity profile was selected for flow entering to the channel. A zero gradient condition in x-direction was used as the outlet boundary condition, along with the symmetry boundary condition for

the upper and lower walls of the channel. The boundary condition used for pressure was zero-normal derivative for the pressure at all boundaries. At the block surfaces, the no-slip boundary condition was taken into account. A two-dimensional incompressible flow of a fluid is considered in the computational domain. The primary parameters affecting the fluid flow in a channel with a square cylinder obstruction are the Reynolds number and the blockage ratio. Reynolds number based on mean inlet velocity, U_m, and cylinder width, B are selected.

2.7 Mesh Quality

For solving Navier-Stocks equations a mapped mesh is considered. Figure 2.12 shows a typical close-up view of a mesh near the block, with refinement in the wake, near the edges and even the interface between air and water. 24,716 nodes are combined to make the domain mesh. The average skewness quality of the mesh is about 0.98 which shows fine mesh is considered. Figure 2.12 shows the skewness quality of elements and figure 2.13 illustrates the mesh in the domain.

Figure 2.12 Skewness elements quality
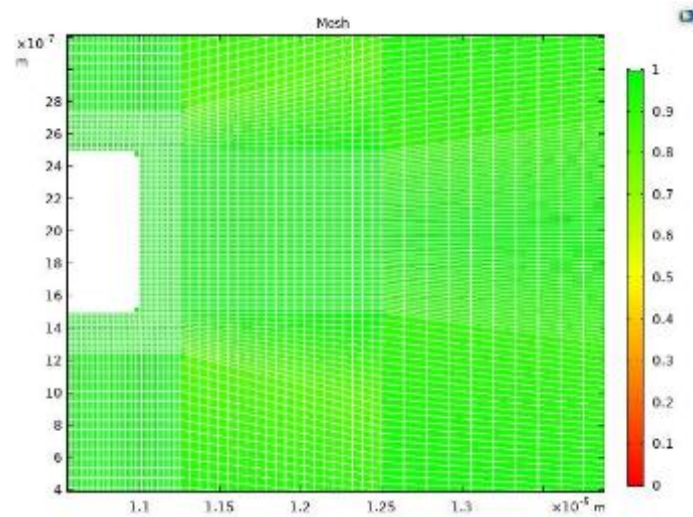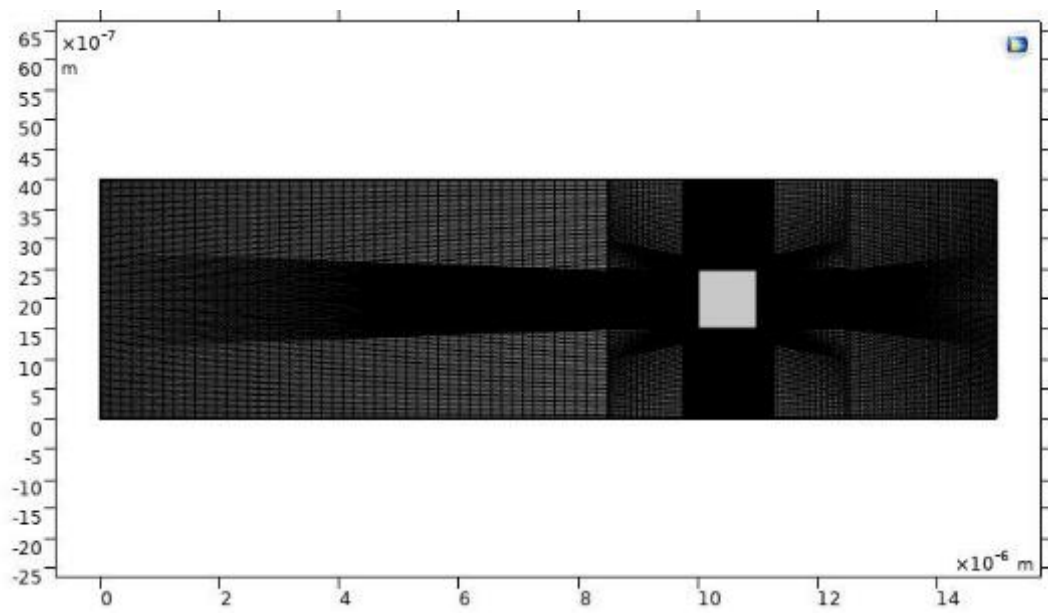
Figure 2.13 The mesh in the domain.

Chapter 3

Results

3.1 On the Importance of Reynolds Number on Particle Deposition Efficiency Without Electrophoretic and Magnetophoretic Force

3.1.1 Dry Cylinder

At the first step, a single dry square fiber is considered over which the flow crosses. The 2-D domain is identical with section 2.6. In terms of considering the effect of four different Reynolds numbers on particle capture efficiency, ($Re = 1$, $Re = 5$, $Re = 10$) are chosen. The flow regime is laminar in this Reynolds range and with $Re = 1$, wakes will not form behind the block but with $Re = 5$, $Re = 10$ the vortex will form behind the square because of vortex shedding phenomena. The grid's node numbers are the same as section 2.7. Due to the good agreement results for $Re = 200$, boundary adapted the square`s wall with Comsol for other Reynolds numbers. As we cited in the previous section the time step that we have selected is suitable as we test it by half time step experiment.

As mentioned before, we have chosen time steps according to the work of R. Franke et al.[104]. The results for four different particle sizes have been tabulated below:

Table 3-1 Variation of particle deposition efficiency with Reynolds number for dry cylinder

Particle diameter Reynolds No.	10 nm	100 nm	500 nm	1000 nm
$Re = 1$	0.000	0.001	0.065	0.132
$Re = 5$	0.000	0.026	0.202	0.225
$Re = 10$	0.000	0.107	0.229	0.241

As it is illustrated in Table 3-1, the results show that with respect to particle diameter when particle diameter increases the deposition efficiency increase too.

Contours of velocity magnitude as well as submicron particle traces are illustrated in Figure 3.1 to Figure 3.8 below:
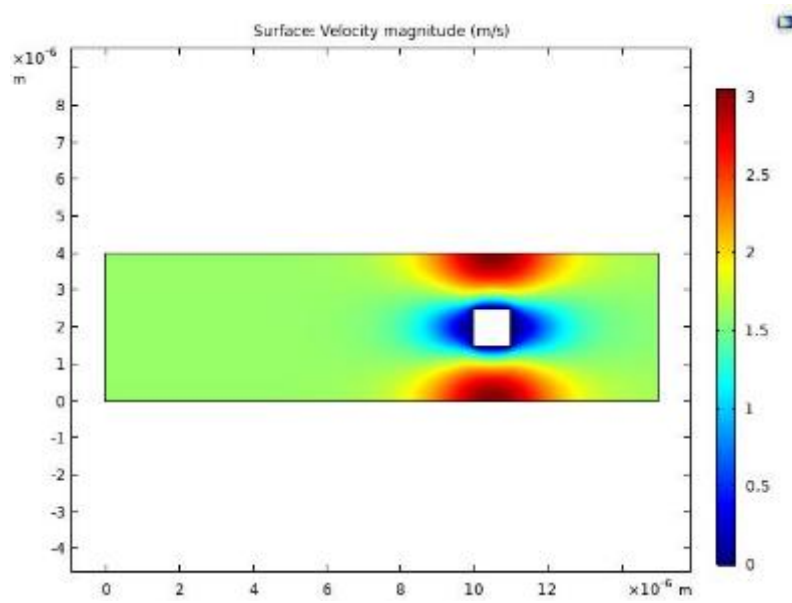
Figure 3.1 Contour of velocity magnitude for $Re = 0.1$
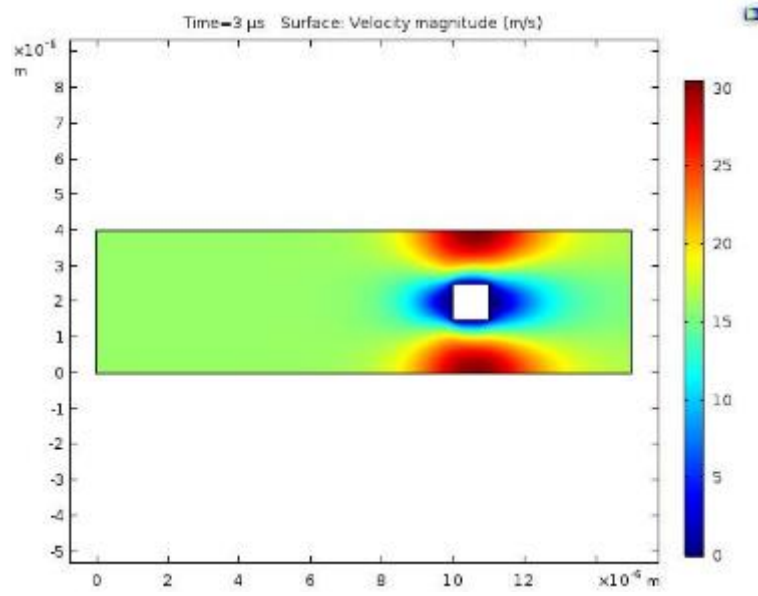
Figure 3.2 Contour of velocity magnitude for $Re = 1$
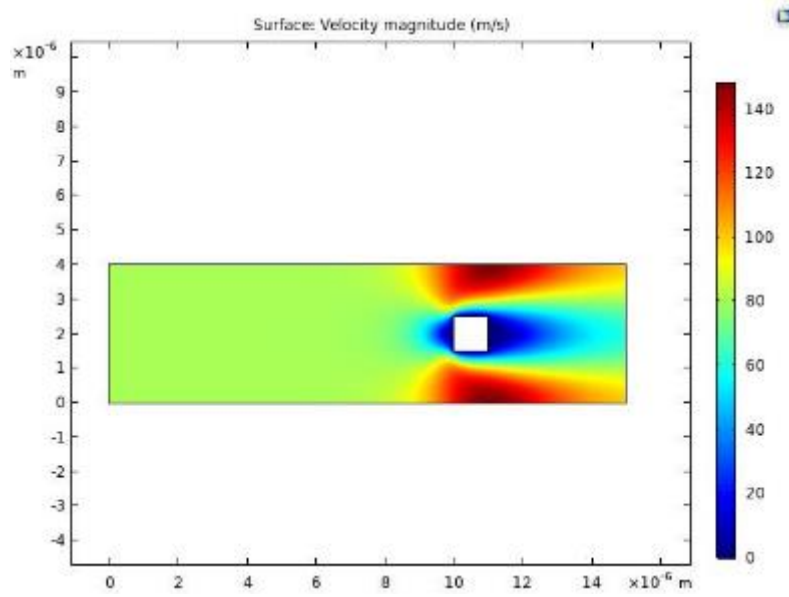
Figure 3.3 Contour of velocity magnitude for $Re = 5$
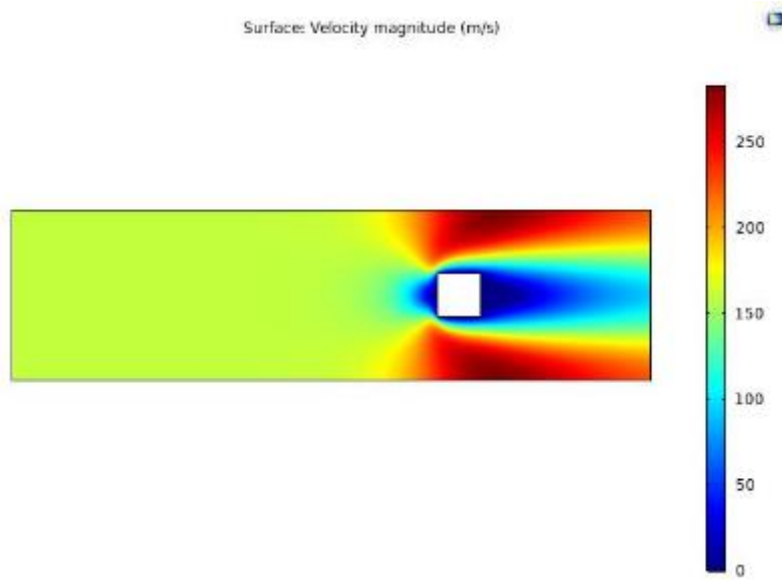
Figure 3.4 Contour of velocity magnitude for $Re = 10$
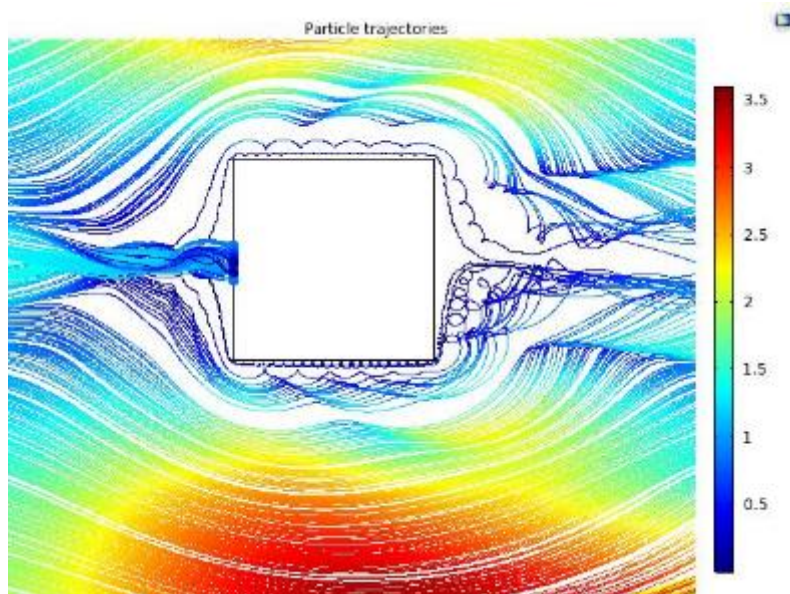
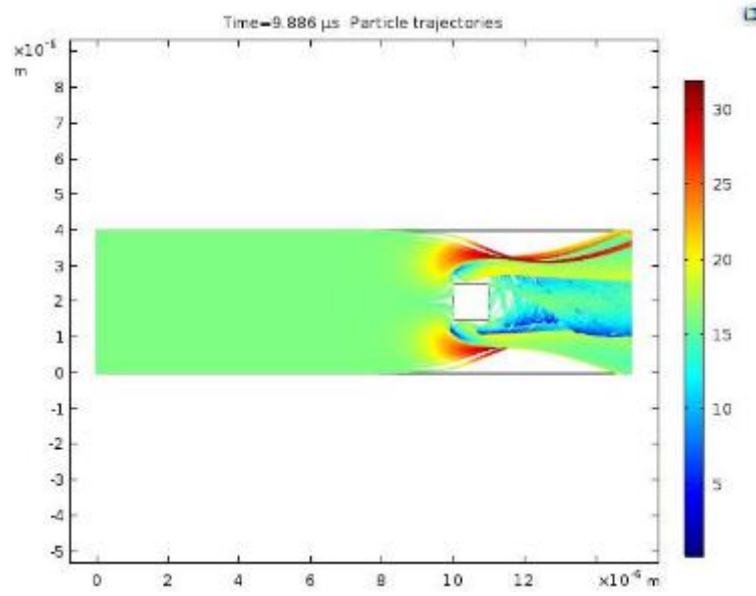Figure 3.5 Particle trajectory lines for $500\ nm$ particle diameter near the cylinder for $Re = 0.1$

Figure 3.6 Particle trajectory lines for 500 nm particle diameter near the cylinder for $Re = 1$
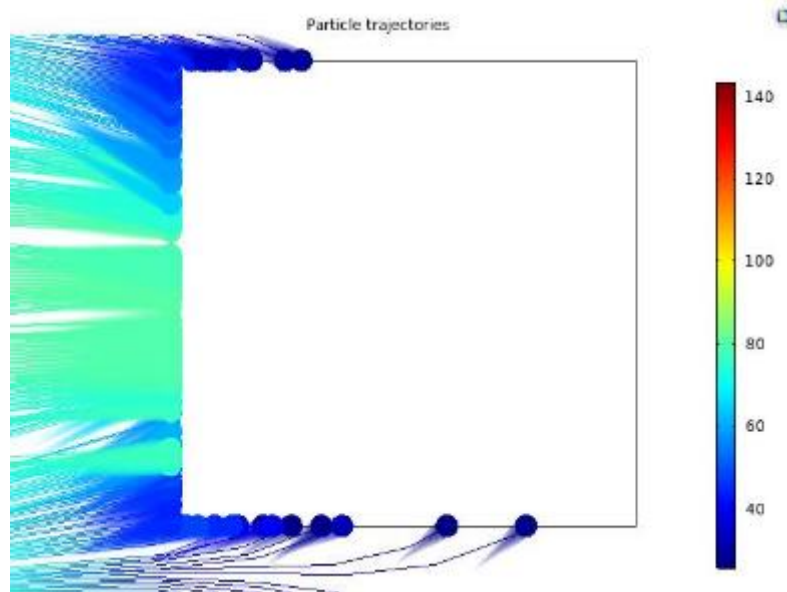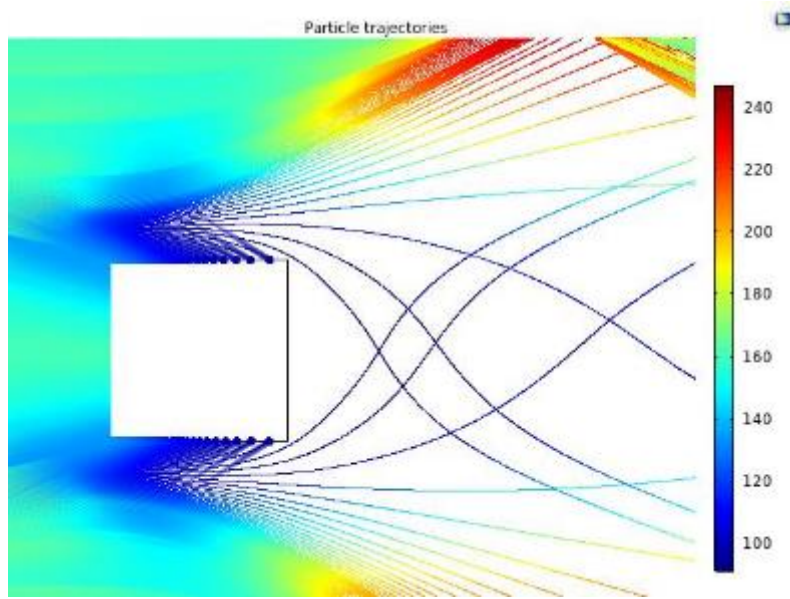

Figure 3.7 Particle trajectory lines for 500 nm particle diameter near the cylinder for $Re = 5$

Figure 3.8 Particle trajectory lines for $500\ nm$ particle diameter near the cylinder for $Re = 10$

3.1.2 Wet Cylinder

Block is wetted by a thin layer of water. The length of the water film is one-half times the length of the block in terms of measuring the particle deposition efficiency of nanoparticles in the flow with four different Reynolds numbers ($Re = 1,\ Re = 5,\ and\ Re = 10$).

Time-step is considered 10^{-3} which is reduced for very low particle diameters to maintain simulation stability. Total simulation time depends on the bulk flow velocity. The simulation injects 1000 particles at the time the flow regime shapes completely.

Water film is located around the block with the thickness of 0.025 micrometer.

Table 3-2 Variation of particle deposition efficiency with Reynolds number for the wetted cylinder.

Particle diameter ⟍ Reynolds No.	10 nm	100 nm	500 nm	1000 nm
$Re = 1$	0.006	0.007	0.291	0.396
$Re = 5$	0.02	0.157	0.327	0.408
$Re = 10$	0.021	0.2	0.349	0.422

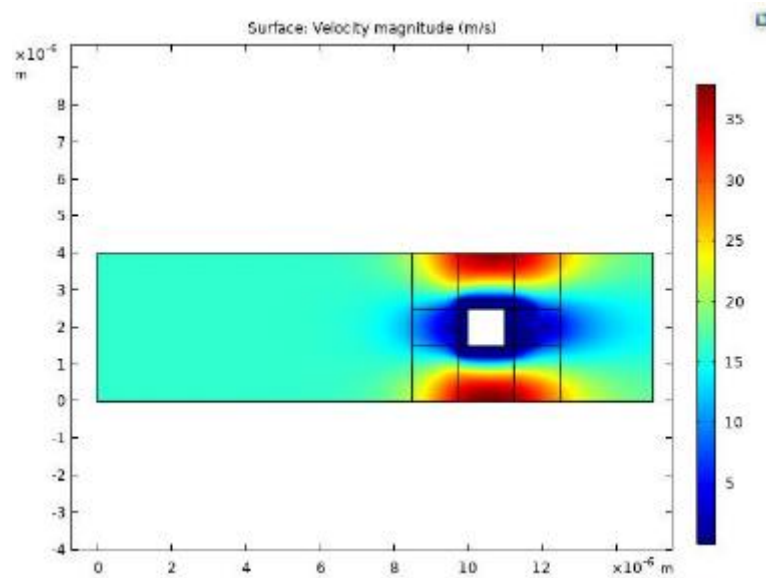Contours of velocity magnitude and volume fraction are illustrated in Figure 3.9 to Figure 3.8 below:
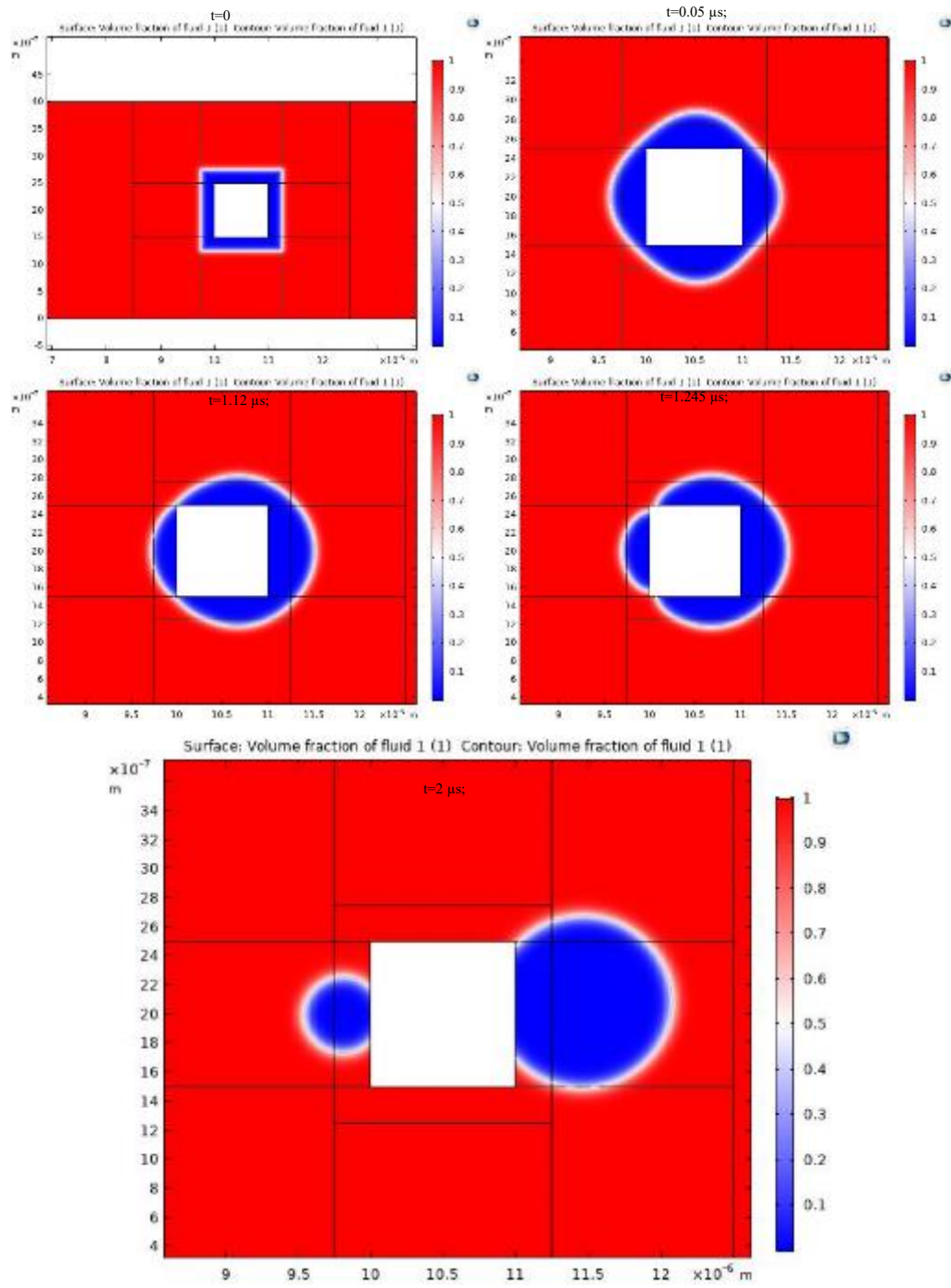

Figure 3.9 Velocity magnitude contour for Re=1.

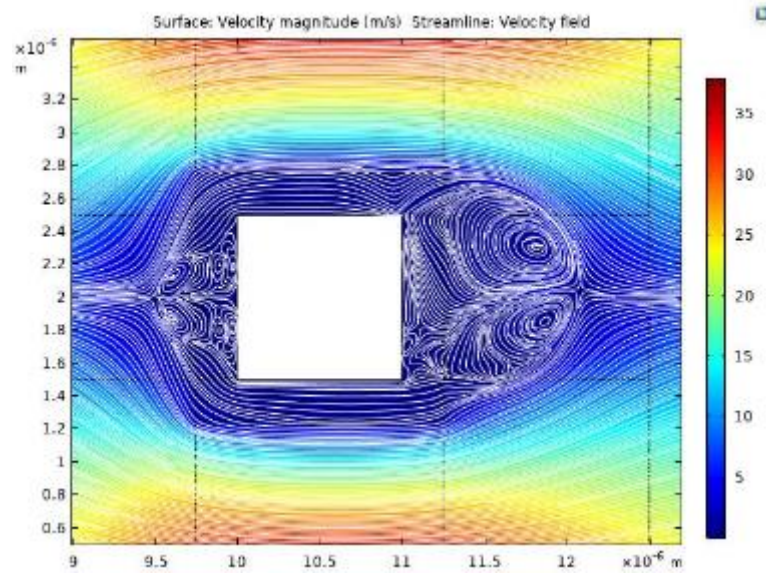Figure 3.10 Volume fraction of water and air respect to the variation of time for Re = 1.

Figure 3.11 Velocity streamline for Re=1 after two phases shaped completely for Re=1.

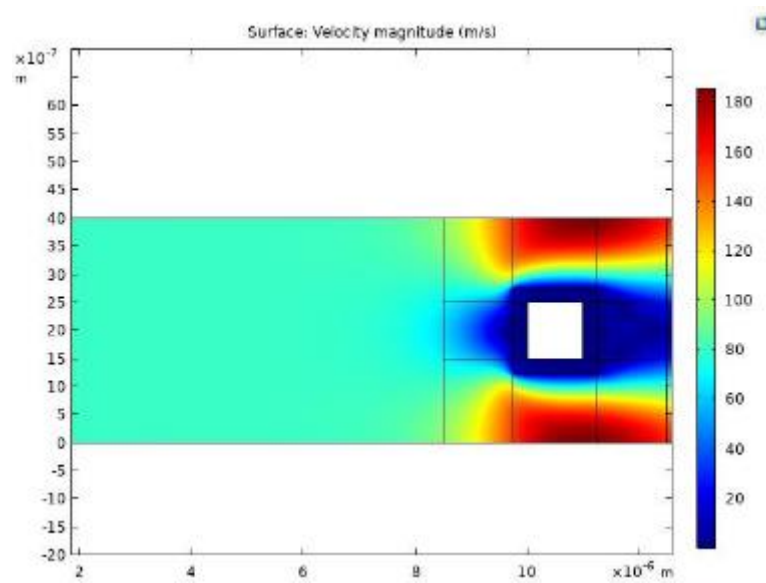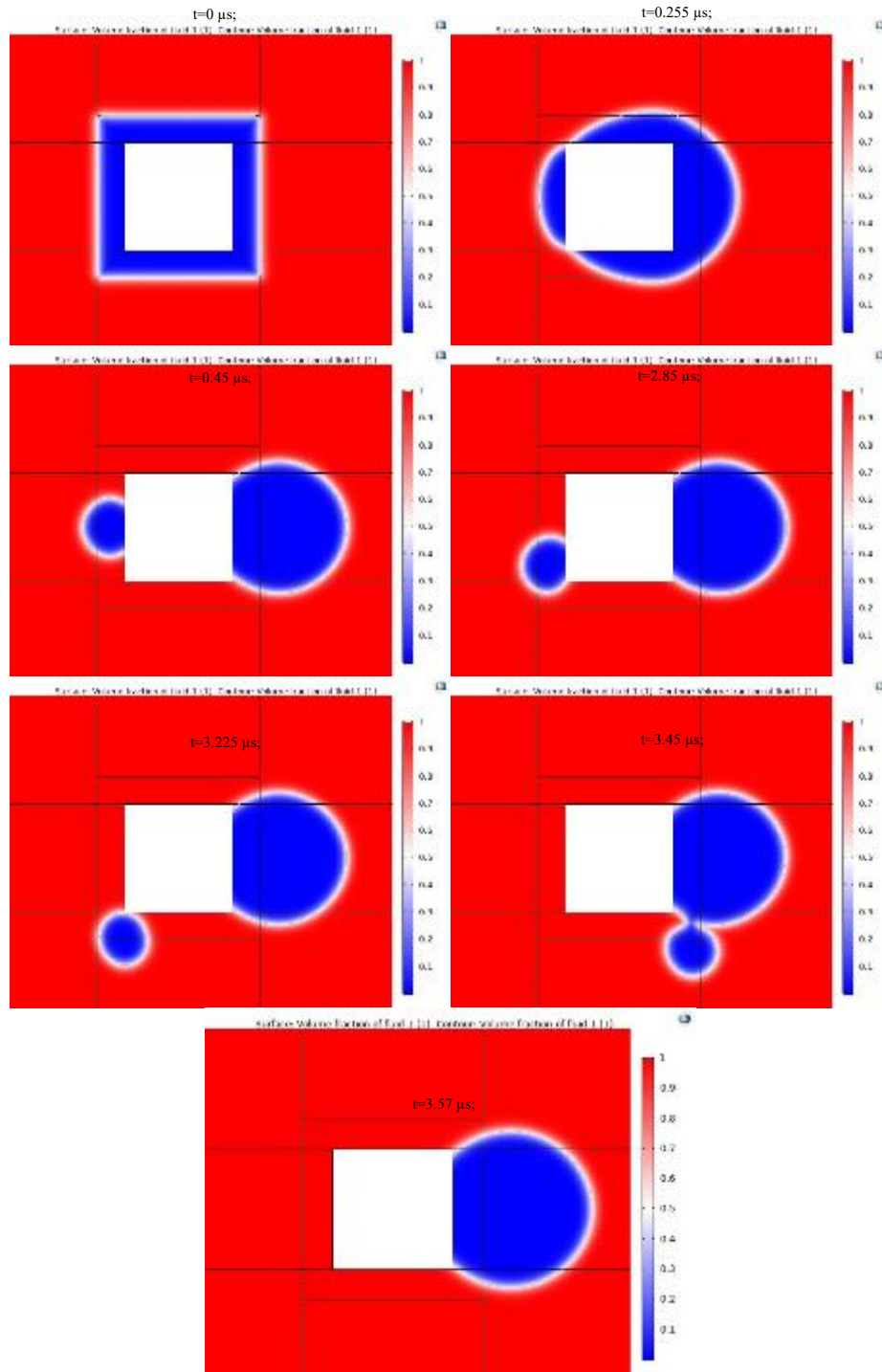Figure 3.12 Velocity contour for Re=10

94

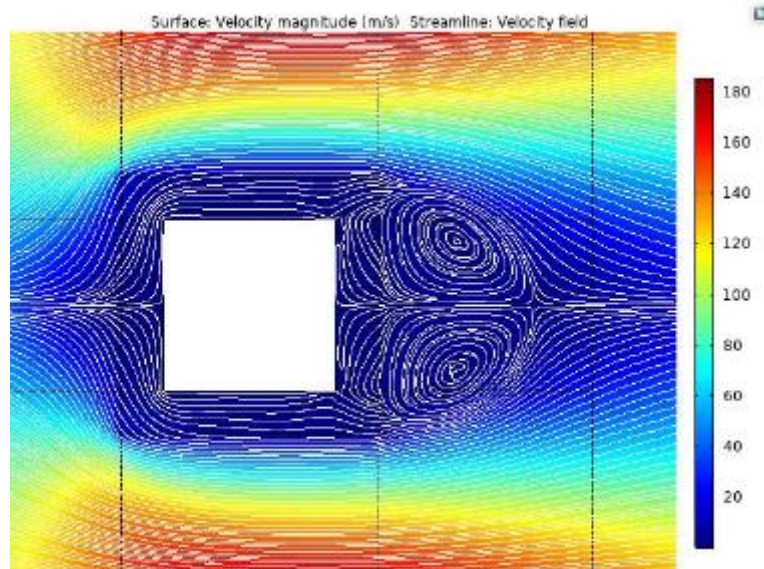Figure 3.13 Volume fraction of water and air respect to the variation of time for Re = 5

95

Figure 3.14 Velocity streamlines after two phase shaped completely for Re=5.
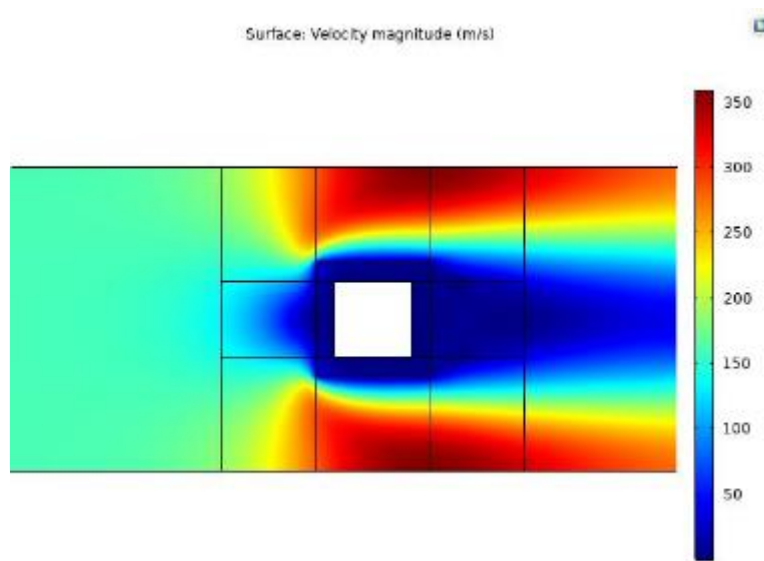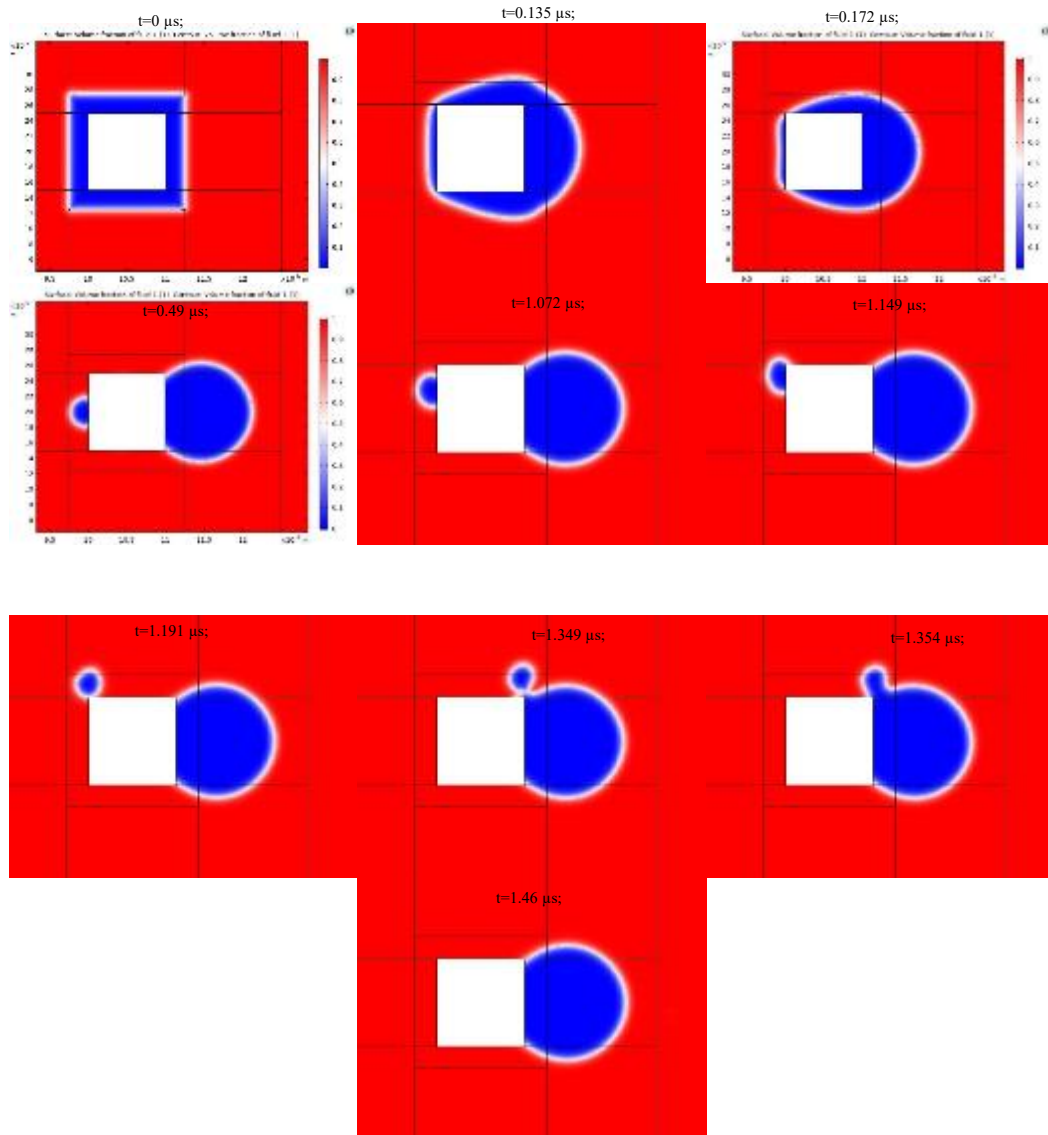

Figure 3.15 Velocity contour for Re=10

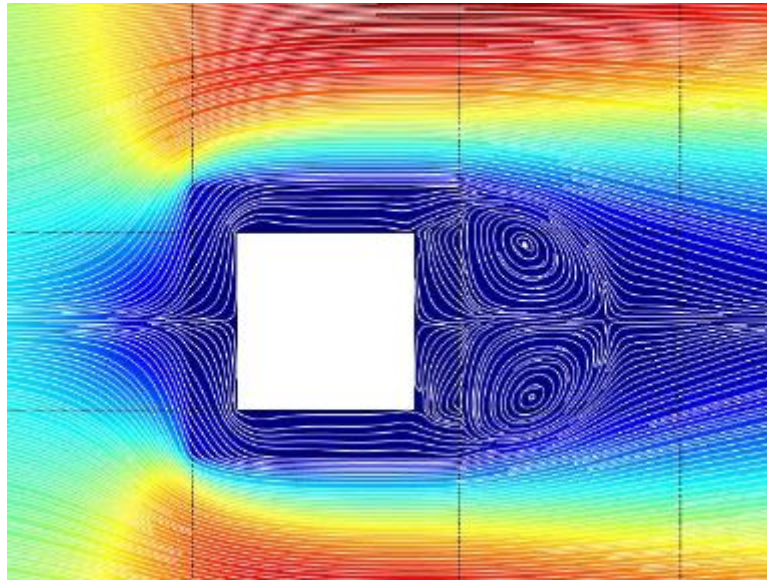Figure 3.16 Volume fraction of water and air respect to the variation of time for Re = 10

Figure 3.17 Velocity streamlines after two phase shaped completely for Re=5.

3.2 On the Importance of Electrostatic on Particle Deposition

In this section electrostatic is added to the domain. The particle deposition efficiency is shown in Table 3-3. Two potential boundaries are added to the domain which is located at the top and the bottom of the duct over the block. The length of the potential line is 4 times of block width. The top plate and bottom plates contain positive and negative potential, respectively. The contour of the electrostatic field is shown in figure 3.18:
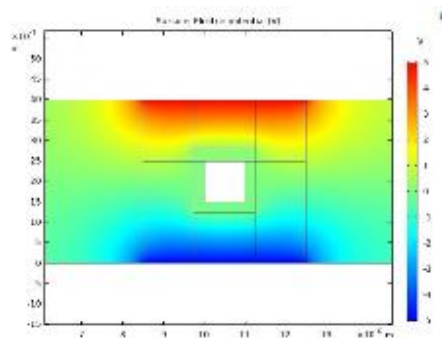

Figure 3.18 Electric potential (V) contour in the domain

98

Dielectrophoretic force is added to particle extra forces which means in this section drag, Brownian, Saffman`s lift, gravity and electrophoretic forces are acting on the particles. Particle and fluid properties are the same as section 3.1. The deposition efficiency, as well as parameters of our simulation study, is shown in Table 3-3:

Table 3-3 Variation of particle deposition efficiency with dielectrophoretic force.

Particle diameter / Reynolds No.	10 nm	100 nm	500 nm	1000 nm
$Re = 1$	0.004	0.007	0.289	0.370
$Re = 5$	0.021	0.153	0.330	0.401
$Re = 10$	0.031	0.190	0.339	0.422

3.3   On the Importance of Electromagnetic Field on Particle Deposition

The magnetic field is added to the simulation by two homogenized coils. The input current of the coils is 500 μA and it has 300 turns. The relative permeability of air and water is equal to 1. The contour and streamlines of the magnetic flux density norm are illustrated in figure 3.19:
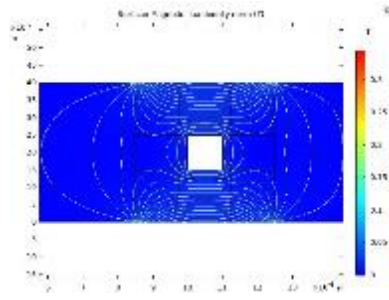
Figure 3.19 Magnitude of Magnetic flux density norm (T).

Magnetophoretic force is added as an effective force to the particle. Relative permeability of particle is considered 5000. As section 3.2 other mechanisms are active. The results are shown in Table 3-4:

Table 3-4 Variation of particle deposition efficiency with electromagnetic fields.

Particle diameter / Reynolds No.	$10\ nm$	$100\ nm$	$500\ nm$	$1000\ nm$
$Re = 1$	0.004	0.008	0.295	0.371
$Re = 5$	0.025	0.155	0.335	0.405
$Re = 10$	0.027	0.191	0.343	0.422

3.4 On the Importance of Electromagnetic and Electrostatic Fields on Particle Deposition

In this step, the flow field condition and parameters of the simulation are the same as section 3.1.2, but both electrophoretic and magnetophoretic forces are added to particles` forces. 5 particles of 501 particles are selected for showing a clear plot of particle trajectory in two

different Reynolds numbers. Particle trajectories of different size of particles in $Re = 5$ and $Re = 10$ are shown in figure 3.20 and 3.21:

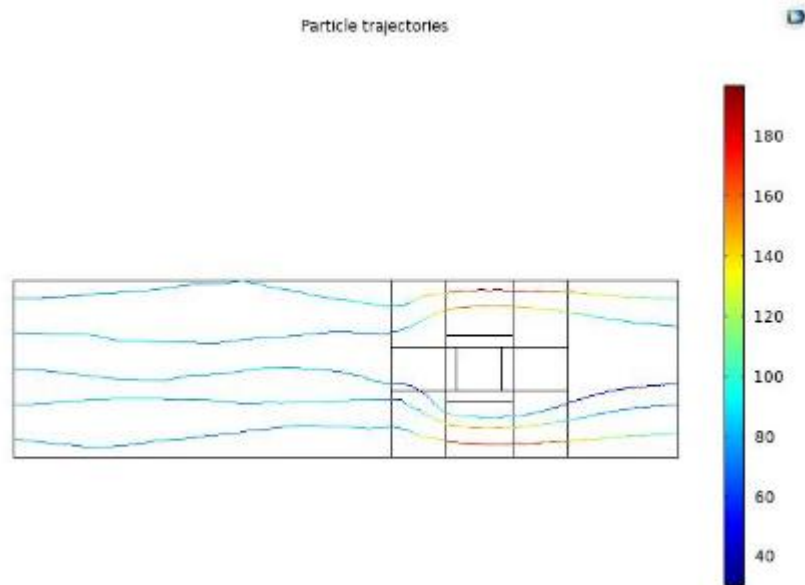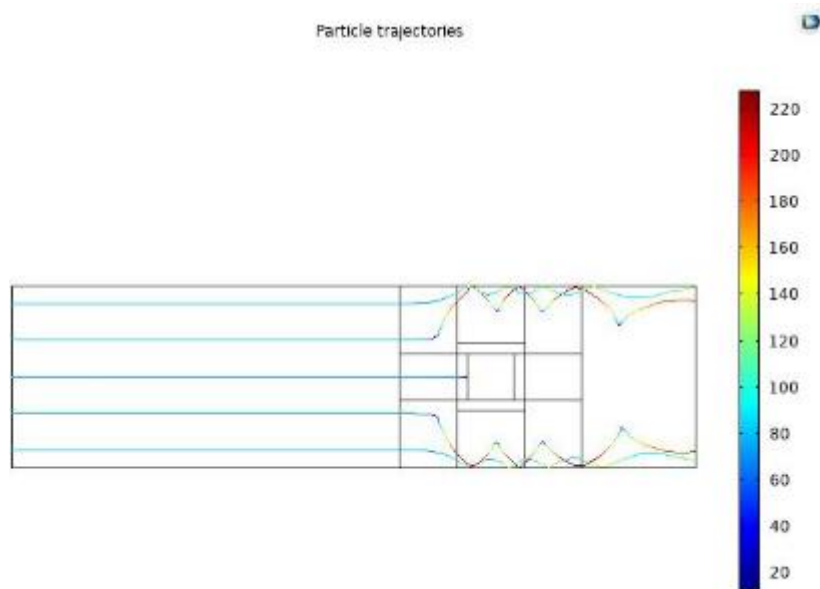Figure 3.20 Particle trajectories for five 10nm particles in Re=5

Figure 3.21 Particle trajectories for five 500nm particles in Re=5
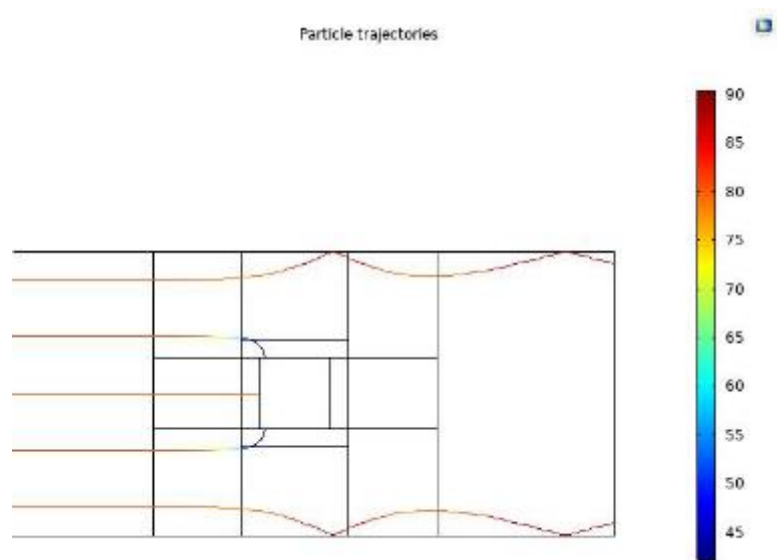
Figure 3.22 Particle trajectories for five 1000nm particles in Re=5
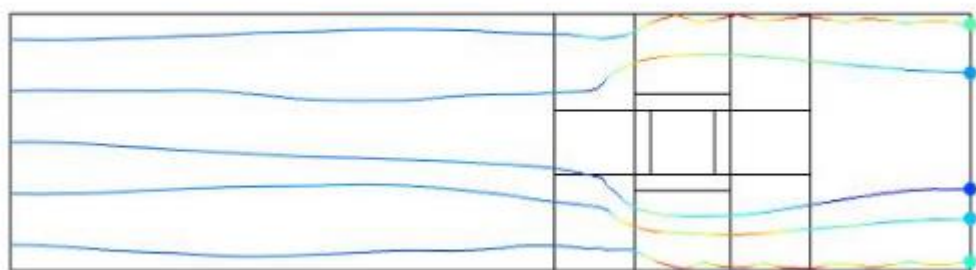
Figure 3.23 Particle trajectories for five 10nm particles in Re=10
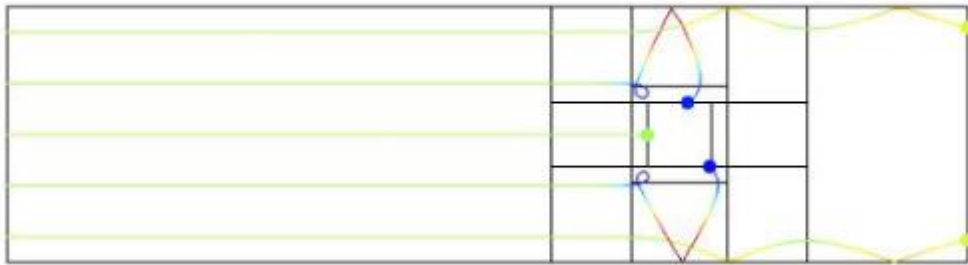
Figure 3.24 Particle trajectories for five 500nm particles in Re=10
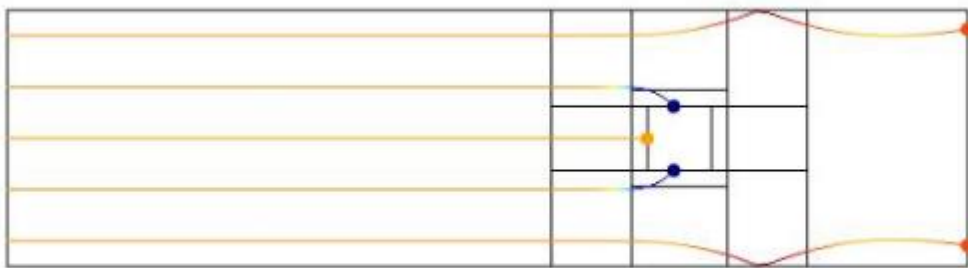
Figure 3.25 Particle trajectories for five 1000nm particles in Re=10

The deposition efficiency, as well as parameters of our simulation study, has been shown in

Table 3-5:

Table 3-5 Variation of particle deposition efficiency with electromagnetic and electrostatic fields.

Particle diameter / Reynolds No.	$10\ nm$	$100\ nm$	$500\ nm$	$1000\ nm$
$Re = 1$	0.006	0.008	0.296	0.369
$Re = 5$	0.023	0.155	0.336	0.404
$Re = 10$	0.025	0.193	0.341	0.422

Chapter 4

Conclusion

This thesis studied the effect of three different Reynolds numbers on the deposition efficiency of a single square cylinder in a filter in the first step. Typically, 1000 particles for a given particle size were injected uniformly in the projected area of the block at a distance of 10B upstream of the block, and their capture efficiency was evaluated. In this case, the flow regimes are laminar vortex shedding and subcritical. Particles are injected when the wakes formed behind the obstacle for $Re = 10$. To begin with, 1000 particles are chosen which have the 100 nm size and injected them into the duct after the average time of 4 seconds and in a moment that streamlines completely formed in our 2-D simulation box. Then, we increased the number of the particles of the same size up to eight times and we reached to the conclusion that its deposition efficiency change with respect to four previous results is below 0.20%. The variations of deposition efficiency with Reynolds number is illustrated in figure 4.4:
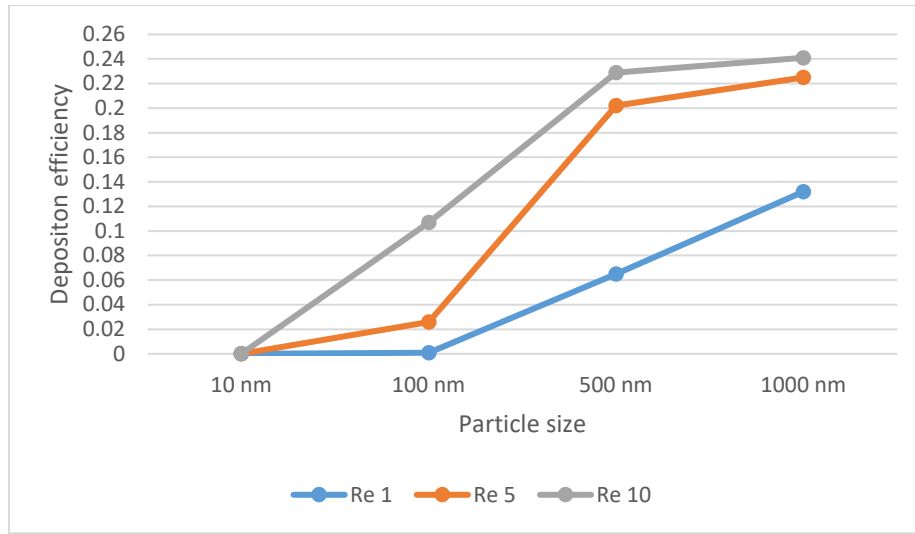
Figure 4.1 Variations of Deposition Efficiency with Reynolds number in the dry cylinder

According to figure 4.1, the deposition efficiency has changed considerably when we have changed the flow regime from creeping flow to laminar vortex shedding. So, for laminar flows, the higher the Reynolds number, the better the deposition efficiency of particles and filtration. In the next steps, we measured the effect of wetting the fiber on the deposition efficiency of 1000 particles that is the optimum number for our simulation. Variations of capture efficiency for a wet square block which have been considered in this study are depicted in figure 4.2:
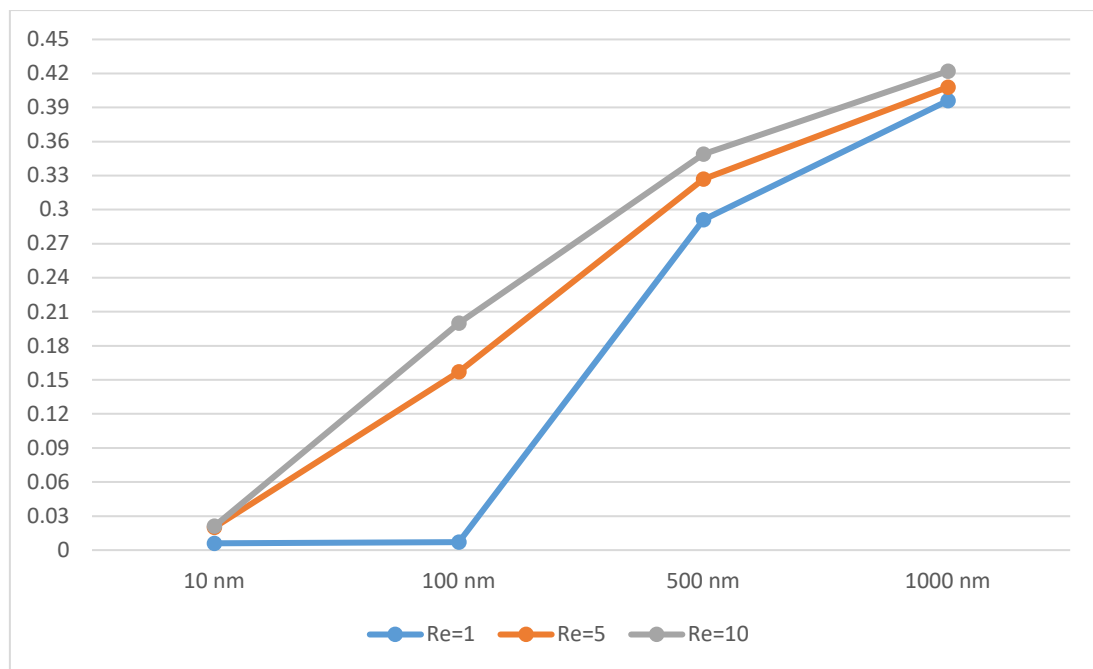
Figure 4.2 Variations of Deposition Efficiency with Reynolds number in the wetted cylinder

By comparing the deposition efficiency results, wetting has an effect on particle deposition and as it is shown in Figure 4.3, the role of wetting in the deposition of nanoparticles with lower Reynolds number is more obvious.
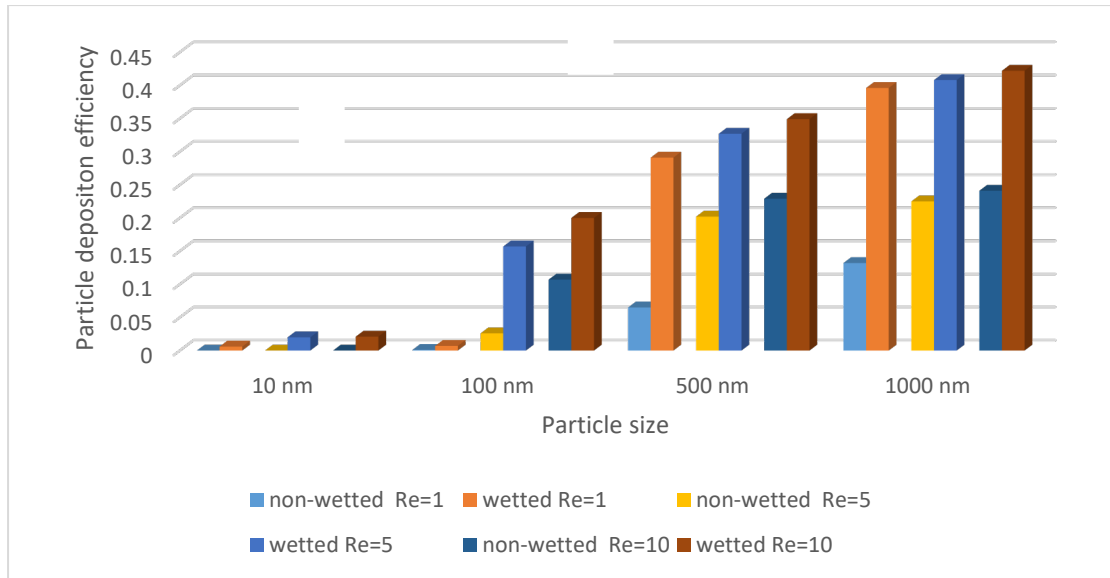
Figure 4.3 Comparison of particle deposition in the wet and dry cylinder

And finally, particle deposition efficiency is computed when electrostatic and electromagnetic forces are added to the domain. As it is shown in **Error! Reference source not found.** with these assumptions which have been chosen for this study and by considering symmetry boundaries, no huge change in capturing particles has occurred. If boundaries are taken as no-slip boundaries, the deposition efficiency will increase by adding electrostatic and electromagnetic forces because the location of electrostatic and electromagnetic fields causes particles to turn to the walls of the duct but not to deposit there due to the wall selected symmetry. By comparing the results, it is obvious that the dominant force is the electromagnetic force.

References

[1] C. Tien and B. V. B. V. Ramarao, *Granular filtration of aerosols and hydrosols*. Elsevier, 2011.

[2] C. Tien and B. V. Ramarao, "Trajectory Analysis of Particle Deposition," *Granul. Filtr. Aerosols Hydrosols*, pp. 169–211, 2007.

[3] D. B. Purchas, *Industrial filtration of liquids*. Hill, 1967.

[4] F. M. Tiller, "Bench-scale design of SLS systems," *Chem. Eng.*, vol. 81, no. 9, pp. 117–119, 1974.

[5] C. Tien and B. V. Ramarao, "Granular Filtration of Aerosols and Hydrosols," pp. 1–20, 2007.

[6] C. Tien, B. V. Ramarao, C. Tien, and B. V. Ramarao, *Granular Filtration of Aerosols and Hydrosols: Butterworths Series in Chemical Engineering*. Butterworth-Heinemann, 2013.

[7] R. A. Juvinall, R. W. Kessie, and M. J. Steindler, "Sand-bed filtration of aerosols: a review of published information on their use in industrial and atomic energy facilities.," Argonne National Lab., Ill., 1970.

[8] G. H. Sykes and J. A. Harper, "Design and operation of a large sand bed for air filtration," in *Treatment of Airborne Radioactive Wastes. Proceedings of a Symposium on Operating and Developmental Experience in the Treatment of Airborne Radioactive Wastes*, 1968.

[9]   K. Witt, "Reliability study of granular filters," *Filters Geotech. Hydraul. Eng.*, pp. 35–42, 1993.

[10]   B. Kalen, "Granular bed filter apparatus and method." Google Patents, 26-Mar-1974.

[11]   W. C. Hinds, *Aerosol technology: properties, behavior, and measurement of airborne particles*. New York: John Wiley & Sons, 2012.

[12]   NIOSH, "Guidance for filtration and air-cleaning systems to protect building environments from airborne chemical, biological or radiological attacks." NIOSH Publications, Cincinnati, OH, USA, 2003.

[13]   J. Kim, *Investigation on charge deterioration of electrically charged filter media using electric force microscopy*. 2005.

[14]   W. C. Hinds, "Aerosol Technology: Properties," *Behav. Meas. airborne Part. (2nd*, 1999.

[15]   R. C. Brown, *Air filtration: an integrated approach to the theory and applications of fibrous filters*. Pergamon, 1993.

[16]   J. Happel, "Viscous flow relative to arrays of cylinders," *AIChE J.*, vol. 5, no. 2, pp. 174–177, 1959.

[17]   S. Kuwabara, "The forces experienced by randomly distributed parallel circular cylinders or spheres in a viscous flow at small Reynolds numbers," *J. Phys. Soc. Japan*, vol. 14, no. 4, pp. 527–532, 1959.

[18]   C. A. Rodman and R. C. Lessmann, "Automotive nonwomen filter media: their

constructions and filter mechanisms," *Tappi J.*, vol. 71, no. 4, pp. 161–168, 1988.

[19]   M. S. El-Shobokshy, S. A. Al-Sanea, and A. M. Adnan, "Computer simulation of monodisperse aerosol collection in fibrous filters," *Aerosol Sci. Technol.*, vol. 20, no. 2, pp. 149–160, 1994.

[20]   B. V. Ramarao, C. Tien, and S. Mohan, "Calculation of single fiber efficiencies for interception and impaction with superposed brownian motion," *J. Aerosol Sci.*, vol. 25, no. 2, pp. 295–313, 1994.

[21]   Y. Li and C.-W. Park, "Deposition of Brownian particles on cylindrical collectors in a periodic array," *J. Colloid Interface Sci.*, vol. 185, no. 1, pp. 49–56, 1997.

[22]   Y. Termonia, "Permeability of sheets of nonwoven fibrous media," *Chem. Eng. Sci.*, vol. 53, no. 6, pp. 1203–1208, 1998.

[23]   S. Dhaniyala and B. Y. H. Liu, "An asymmetrical, three-dimensional model for fibrous filters," *Aerosol Sci. Technol.*, vol. 30, no. 4, pp. 333–348, 1999.

[24]   C. Zhu, C. H. Lin, and C. S. Cheung, "Inertial impaction-dominated fibrous filtration with rectangular or cylindrical fibers," *Powder Technol.*, vol. 112, no. 1–2, pp. 149–162, 2000.

[25]   D. G. Thomas and C. E. Lapple, "Deposition of aerosol particles in fibrous filters," *AIChE J.*, vol. 7, no. 2, pp. 203–210, 1961.

[26]   A. Lisowski, E. Jankowska, A. Thorpe, and R. C. Brown, "Performance of textile fibre filter material measured with monodisperse and standard aerosols," *Powder Technol.*,

vol. 118, no. 1–2, pp. 149–159, 2001.

[27] V. A. Kirsch, "Stokes flow in model fibrous filters," *Sep. Purif. Technol.*, vol. 58, no. 2, pp. 288–294, 2007.

[28] I. B. Stechkina and N. A. Fuchs, "Studies on fibrous aerosol filters—I. Calculation of diffusional deposition of aerosols in fibrous filters," *Ann. Occup. Hyg.*, vol. 9, no. 2, pp. 59–64, 1966.

[29] V. A. Kirsh, "Deposition of aerosol nanoparticles in fibrous filters," *Colloid J.*, vol. 65, no. 6, pp. 726–732, 2003.

[30] N. De Greef *et al.*, "Direct growth of carbon nanotubes on carbon fibers: Effect of the CVD parameters on the degradation of mechanical properties of carbon fibers," *Diam. Relat. Mater.*, vol. 51, pp. 39–48, 2015.

[31] K. W. Lee and B. Y. H. Liu, "Theoretical study of aerosol filtration by fibrous filters," *Aerosol Sci. Technol.*, vol. 1, no. 2, pp. 147–161, 1982.

[32] R. C. Brown, "A many-fibre model of airflow through a fibrous filter," *J. Aerosol Sci.*, vol. 15, no. 5, pp. 583–593, 1984.

[33] G. A. Davies and M. S. Abdel-Ghani, "Simulation of non-woven fibre mats and the application to coalescers," *Chem. Eng. Sci.*, vol. 40, no. 1, pp. 117–129, 1985.

[34] T. J. Overcamp, "Filtration by randomly distributed fibers," vol. 16, no. 5, pp. 473–475, 1985.

[35] D. F. J. Graham W. Jackson, "The permeability of Fibrous media," *Can. J. Chem.*

Eng., vol. 64, pp. 364–374, 1986.

[36]   K. R. Spurny, "On the filtration of fibrous aerosols," *Sci. Total Environ.*, vol. 52, no. 3, pp. 189–199, 1986.

[37]   N. Rao and M. Faghri, "Computer modeling of aerosol filtration by fibrous filters," *Aerosol Sci. Technol.*, vol. 8, no. 2, pp. 133–156, 1988.

[38]   J. Pich, "AEROSOLS-PHYSICAL CHEMISTRY AND APPLICATIONS." PELLEOVA 24, PRAGUE 6 160 00, CZECH REPUBLIC, 1965.

[39]   J. Pich, "Pressure characteristics of fibrous aerosol filters," *J. Colloid Interface Sci.*, vol. 37, no. 4, pp. 912–917, 1971.

[40]   F. Löffler, "Air filtration. Von CN Davies. Academic Press Inc., London 1973. Aulf., X 171 Ss., zahlr. Abb.,£ 4.00," *Chemie Ing. Tech.*, vol. 46, no. 8, p. 364, 1974.

[41]   S. Dhaniyala and B. Liu, "Investigations of particle penetration in fibrous filters: Part II. Theoretical," *J. IEST*, vol. 42, no. 2, pp. 40–46, 1999.

[42]   M. M. Zdravkovich, "Flow around circular cylinders volume 1: fundamentals," *Oxford Univ. Press. Oxford*, vol. 19, p. 185, 1997.

[43]   M. Coutanceau and J.-R. Defaye, "Circular Cylinder Wake Configurations: A Flow Visualization Survey," *Appl. Mech. Rev.*, vol. 44, no. 6, pp. 255–305, Jun. 1991.

[44]   C. H. K. Williamson, "Vortex Dynamics in the Cylinder Wake," *Annu. Rev. Fluid Mech.*, vol. 28, no. 1, pp. 477–539, 1996.

[45] E. Achenbach, "Distribution of local pressure and skin friction around a circular cylinder in cross-flow up to Re= 5× 10 6," *J. Fluid Mech.*, vol. 34, no. 4, pp. 625–639, 1968.

[46] F. Jorgen and S. B. Mutlu, *Hydrodynamics Around Cylindrical Structures*, vol. 12. World Scientific, 1997.

[47] P. K. Kundu and I. M. Cohen, "Fluid mechanics, 3rd edn," *San Diego, CA, USA Elsevier Acad. Press*, vol. 1, pp. 271–377, 2004.

[48] W. W. H. Bruce R. Munson, Donald F. Young, Theodore H. Okiishi, *Fundamentals of Fluid Mechanics, 6th Edition SI Version*. John Wiley & Sons, 2009.

[49] G. Yadigaroglu and G. F. Hewitt, Eds., *Introduction to Multiphase Flow*. Cham: Springer International Publishing, 2018.

[50] C. E. Brennen and C. E. Brennen, *Fundamentals of multiphase flow*. Cambridge university press, 2005.

[51] S. Gross and A. Reusken, *Numerical Methods for Two-phase Incompressible Flows*, vol. 40. 2011.

[52] G. Birkhoff and E. H. Zarantonello, "Jets, Wakes, and Cavities (Academic, New York, 1957)," *Google Sch.*, pp. 221–235.

[53] M. P. Tulin, "Supercavitating propellers history, operating characteristics, mechanism of operation," HYDRONAUTICS INC LAUREL MD, 1964.

[54] A. D. B. Woods, B. N. Brockhouse, M. Sakamoto, and R. N. Sinclair, "Inelastic

scattering of neutrons in solids and liquids," *IAEA, Vienna*, vol. 487, 1961.

[55] E. Olsson and G. Kreiss, "A conservative level set method for two phase flow," *J. Comput. Phys.*, vol. 210, no. 1, pp. 225–246, 2005.

[56] S. O. Unverdi and G. Tryggvason, "A front-tracking method for viscous, incompressible, multi-fluid flows," *J. Comput. Phys.*, vol. 100, no. 1, pp. 25–37, 1992.

[57] S. Osher and R. Fedkiw, *Level set methods and dynamic implicit surfaces*, vol. 153. Springer Science & Business Media, 2006.

[58] J. A. Sethian, *Level set methods and fast marching methods: evolving interfaces in computational geometry, fluid mechanics, computer vision, and materials science*, vol. 3. Cambridge university press, 1999.

[59] M. Sussman, E. Fatemi, P. Smereka, and S. Osher, "An improved level set method for incompressible two-phase flows," *Comput. Fluids*, vol. 27, no. 5–6, pp. 663–680, 1998.

[60] M. Sussman, P. Smereka, and S. Osher, "A level set approach for computing solutions to incompressible two-phase flow," *J. Comput. Phys.*, vol. 114, no. 1, pp. 146–159, 1994.

[61] D. Halliday and R. Resnick, *Fundamentals of physics*. John Wiley & Sons, 1981.

[62] W. H. Hayt, J. A. John Buck, and J. A. Buck, *Engineering electromagnetics*, vol. 6. McGraw-Hill New York, 2001.

[63] D. K. Cheng, *Field and wave electromagnetics*. Pearson Education India, 1989.

[64]   N. V Churaev, B. V Derjaguin, and V. M. Muller, *Surface forces*. Springer Science & Business Media, 2013.

[65]   L. Boinovich and A. Emelyanenko, "Wetting and surface forces," *Adv. Colloid Interface Sci.*, vol. 165, no. 2, pp. 60–69, 2011.

[66]   N. V Churaev, "NV Churaev, VM Starov, and BV Derjaguin, J. Colloid Interface Sci. 89, 16 (1982).," *J. Colloid Interface Sci.*, vol. 89, p. 16, 1982.

[67]   Y. Solomentsev, "Y. Solomentsev and LR White, J. Colloid Interface Sci. 218, 122 (1999).," *J. Colloid Interface Sci.*, vol. 218, p. 122, 1999.

[68]   L. Livadaru and A. Kovalenko, "Fundamental mechanism of translocation across liquidlike membranes: toward control over nanoparticle behavior," *Nano Lett.*, vol. 6, no. 1, pp. 78–83, 2006.

[69]   J. Ralston, M. Popescu, and R. Sedev, "Dynamics of wetting from an experimental point of view," *Annu. Rev. Mater. Res.*, vol. 38, pp. 23–43, 2008.

[70]   J. Drelich, "The effect of drop (bubble) size on contact angle at solid surfaces," *J. Adhes.*, vol. 63, no. 1–3, pp. 31–51, 1997.

[71]   A. Mendez-Vilas, A. B. Jodar-Reyes, and M. L. Gonzalez-Martin, "Ultrasmall liquid droplets on solid surfaces: production, imaging, and relevance for current wetting research.," *Small*, vol. 5, no. 12, pp. 1366–1390, Jun. 2009.

[72]   R. Pericet-Camara, G. K. Auernhammer, K. Koynov, S. Lorenzoni, R. Raiteri, and E. Bonaccurso, "Solid-supported thin elastomer films deformed by microdrops," *Soft*

Matter, vol. 5, no. 19, pp. 3611–3617, 2009.

[73]   J. W. Gibbs, *The scientific papers. Vol. 1, Vol. 1,*. New York: Dover Publications, 1961.

[74]   A. Amirfazli and A. W. Neumann, "Status of the three-phase line tension: a review," *Adv. Colloid Interface Sci.*, vol. 110, no. 3, pp. 121–141, Aug. 2004.

[75]   F. Dutka and M. Napiórkowski, "The influence of line tension on the formation of liquid bridges in atomic force microscope-like geometry," *J. Phys. Condens. Matter*, vol. 19, no. 46, p. 466104, 2007.

[76]   L. Schimmele, M. Napiórkowski, and S. Dietrich, "Conceptual aspects of line tensions," *J. Chem. Phys.*, vol. 127, no. 16, p. 164715, 2007.

[77]   J. O. Indekeu, "JO Indekeu, Int. J. Mod. Phys. B 8, 309 (1994).," *Int. J. Mod. Phys. B*, vol. 8, p. 309, 1994.

[78]   A. Marmur, "A guide to the equilibrium contact angles maze," *Contact Angle Wettability Adhes.*, vol. 6, no. 3, 2009.

[79]   A. Marmur, "Contact angle equilibrium: the intrinsic contact angle," *J. Adhes. Sci. Technol.*, vol. 6, no. 6, pp. 689–701, 1992.

[80]   A. Amirfazli, S. Hänig, A. Müller, and A. W. Neumann, "Measurements of Line Tension for Solid−Liquid−Vapor Systems Using Drop Size Dependence of Contact Angles and Its Correlation with Solid−Liquid Interfacial Tension," *Langmuir*, vol. 16, no. 4, pp. 2024–2031, Feb. 2000.

[81] L. Golshahi, J. Abedi, and Z. Tan, "Granular filtration for airborne particles: Correlation between experiments and models," *Can. J. Chem. Eng.*, vol. 87, no. 5, pp. 726–731, 2009.

[82] B. M. Wenzel *et al.*, "Filtration of dust in an intermittent moving granular bed filter: Performance and modeling," *Sep. Purif. Technol.*, vol. 133, pp. 108–119, 2014.

[83] Y. S. Chen, S. S. Hsiau, S. C. Lai, Y. P. Chyou, H. Y. Li, and C. J. Hsu, "Filtration of dust particulates with a moving granular bed filter," *J. Hazard. Mater.*, vol. 171, no. 1–3, pp. 987–994, 2009.

[84] J. R. Coury, K. V. Thambimuthu, and R. Clift, "Capture and rebound of dust in granular bed gas filters," *Powder Technol.*, vol. 50, no. 3, pp. 253–265, 1987.

[85] I. A. El-Hedok, L. Whitmer, and R. C. Brown, "The influence of granular flow rate on the performance of a moving bed granular filter," *Powder Technol.*, vol. 214, no. 1, pp. 69–76, 2011.

[86] I. A. El-Hedok, L. Whitmer, and R. C. Brown, "The influence of granular flow rate on the performance of a moving bed granular filter," *Powder Technol.*, vol. 214, no. 1, pp. 69–76, Nov. 2011.

[87] W. Peukert and C. Wadenpohl, "Industrial separation of fine particles with difficult dust properties," *Powder Technol.*, vol. 118, no. 1–2, pp. 136–148, Aug. 2001.

[88] S. C. Saxena, R. F. Henry, and W. F. Podolski, "Particulate removal from high-temperature, high-pressure combustion gases," *Prog. Energy Combust. Sci.*, vol. 11, no. 3, pp. 193–251, Jan. 1985.

[89]   J. Seville, T. G. Chuah, V. Sibanda, and P. Knight, "Gas cleaning at high temperatures using rigid ceramic filters," *Adv. Powder Technol.*, vol. 14, no. 6, pp. 657–672, Jan. 2003.

[90]   W. Peukert and F. Löffler, "Influence of temperature on particle separation in granular bed filters," *Powder Technol.*, vol. 68, no. 3, pp. 263–270, 1991.

[91]   G. Xiao *et al.*, "Granular bed filter: A promising technology for hot gas clean-up," *Powder Technol.*, vol. 244, pp. 93–99, 2013.

[92]   H.-C. Yeh and B. Y. H. Liu, "Aerosol filtration by fibrous filters—I. theoretical," *J. Aerosol Sci.*, vol. 5, no. 2, pp. 191–204, Mar. 1974.

[93]   R. Givehchi, Q. Li, and Z. Tan, "The effect of electrostatic forces on filtration efficiency of granular filters," *Powder Technol.*, vol. 277, pp. 135–140, 2015.

[94]   H. Zhao and C. G. Zheng, "Modeling of gravitational wet scrubbers with electrostatic enhancement," *Chem. Eng. Technol. Ind. Chem. Equipment-Process Eng.*, vol. 31, no. 12, pp. 1824–1837, 2008.

[95]   P. Centner, H. Büttner, and F. Ebert, "Investigation of a wet dust scrubber with a pneumatic nozzle: Dust collection based on turbulent diffusion," *Chem. Eng. Technol.*, vol. 12, no. 1, pp. 439–444, 1989.

[96]   H. T. Kim, C. H. Jung, S. N. Oh, and K. W. Lee, "Particle removal efficiency of gravitational wet scrubber considering diffusion, interception, and impaction," *Environ. Eng. Sci.*, vol. 18, no. 2, pp. 125–136, 2001.

[97] L. Guan *et al.*, "Numerical simulation of ash particle deposition characteristics on the granular surface of a randomly packed granular filter," *Powder Technol.*, vol. 314, pp. 78–88, 2017.

[98] H. Zhao and C. Zheng, "Modeling of gravitational wet scrubbers with electrostatic enhancement," *Chem. Eng. Technol.*, vol. 31, no. 12, pp. 1824–1837, 2008.

[99] A. Li, G. Ahmadi, R. G. Bayer, and M. A. Gaynes, "Aerosol particle deposition in an obstructed turbulent duct flow," *J. Aerosol Sci.*, vol. 25, no. 1, pp. 91–112, 1994.

[100] O. Schenk and K. Gärtner, "Solving unsymmetric sparse systems of linear equations with PARDISO," *Futur. Gener. Comput. Syst.*, vol. 20, no. 3, pp. 475–487, 2004.

[101] O. Schenk and K. Gärtner, "On fast factorization pivoting methods for sparse symmetric indefinite systems," *Electron. Trans. Numer. Anal.*, vol. 23, no. 1, pp. 158–179, 2006.

[102] L. Boinovich and A. Emelyanenko, "Wetting and surface forces," *Adv. Colloid Interface Sci.*, vol. 165, no. 2, pp. 60–69, 2011.

[103] S. M. Banihashemi Tehrani, A. Moosavi, and H. Sadrhosseini, "Filtration of aerosol particles by cylindrical fibers within a parallel and staggered array," *Microsyst. Technol.*, vol. 22, no. 5, pp. 965–977, 2016.

[104] R. Franke, W. Rodi, and B. Schönung, "Numerical calculation of laminar vortex-shedding flow past cylinders," *J. Wind Eng. Ind. Aerodyn.*, vol. 35, pp. 237–257, 1990.

[105] A. Roshko, "Experiments on the flow past a circular cylinder at very high Reynolds

number," *J. Fluid Mech.*, vol. 10, no. 3, pp. 345–356, 1961.